공학박사 학위논문

Innovative wet-spinning for manufacturing defect free PAN fibers: Electric current assisted process

2018년 8월

서울대학교 대학원

재료공학부

양 호 성

Innovative wet-spinning for manufacturing defect free PAN fibers: Electric current assisted process

낮은 결점 PAN 섬유 제조를 위한 혁신 습식방사 공정:
전류인가 공정

지도교수 유 웅 열

이 논문을 공학박사 학위논문으로 제출함

2018년 8월

서울대학교 대학원

재료공학부

양 호 성

양호성의 공학박사 학위논문을 인준함

2018년 8월

위 원 장 _____ 윤 재 륜 _____ (인)

부위원장 _____ 유 웅 열 _____ (인)

위 원 _____ 안 철 희 _____ (인)

위 원 _____ 육 지 호 _____ (인)

위 원 _____ 정 용 식 _____ (인)

Innovative wet-spinning for manufacturing defect free PAN fibers: Electric current assisted process

Advisor: Woong-Ryeol Yu

by

Ho-Sung Yang

2018

Department of Materials Science and Engineering
Graduated School
Seoul National University

Abstract

Wet spinning is a conventional spinning process for making fibers. Wet-spun Polyacrylonitrile (PAN) fibers have become more important since the discovery of PAN fibers in the 1960s that they can be transformed into carbon fibers through heat treatment. However, significant progress has not been made in wet spinning since the wet spun PAN fibers were commercialized in 1949. A new process parameter, such as the electric current, has not been introduced and its effect on the final properties of the PAN fiber has also not been investigated.

In this thesis, a new process, current-assisted wet-spinning, was developed, which is the first attempt in the world. The main idea of current-assisted wet-spinning was inspired by the electrospinning. In the electrospinning process, polymer solutions are continuously spun into nanometer-sized fibers without significant damage even at extremely high electric potential (tens of kV). Like electrospinning, the current-assisted process was carried out simply by applying electric potential to PAN solution in the existing wet-spinning process. Unlike electrospinning, the electric current in current-assisted wet-spinning process was several hundred microampere.

The PAN fibers fabricated *via* the current-assisted wet-spinning process (EPANf) showed 20% higher mechanical properties than the PAN fiber fabricated *via* general wet-spinning process (GPANf). Various characterization methods were conducted for both samples to investigate the mechanism of improved mechanical properties in EPANf. It was revealed that the applied electric potential affected the coagulation

environment in coagulation bath by forming ions in PAN solution, attracting more non-solvent (water). The more absorbed non-solvent in the PAN fibers (EPANf) minimized the enlargement of existing voids and nanocavitation during following drawing process, resulting in the enhanced mechanical properties of PAN fibers. Due to the simple set-up of current-assisted wet-spinning process, it is expected that the newly developed process can be applied to commercial wet-spinning process, offering new opportunities of innovating PAN fibers and their productions.

Keywords: PAN fiber, current-assisted wet-spinning, wet-spinning, improved mechanical properties, defect minimization

Student number: 2014-31056

Contents

List of figures

Figure 6.13. TGA comparison of GPANf-CNT0.5 and EPANf-CNT0.5.

List of tables

1. Introduction

1.1. PAN fiber

PAN and its copolymer fibers were first marketed in 1949 by DuPont (Orlon as brand name). Fibers made from polymer with 85 wt% or more acrylonitrile (AN) are called acrylic fibers and made from polymer less than 85 wt% AN are called modacrylic fibers. Many researches about wet-spinning of PAN conducted in 1950-1970 led to the establishment of large-scale plant for PAN fibers production. Since the 1970s, urbanization and the rapid growth in artificial fiber have led to a gradual decline in wool production. Since PAN fibers are very compatible with wool (the low density (1.17-1.18 g/cm^3) and thermal conductivity (1.113±0.117 W/(m·K)), they have begun to replace wool. Comonomer (mainly vinyl acetate and methacrylate) is added in acrylic fiber to improve dyeability and textile processibility (acrylate provides adsorbing sites to dyes). With comonomer, acrylic fiber has excellent color-fastness in brilliant color. Moreover, acrylic fiber has good dimensional stability and is particularly resistant to shrinkage and wrinkles. Resistance to damage by moth, oils, and chemicals is also a feature of acrylic fiber. The most distinctive feature of acrylic fiber is the strong resistance to deterioration from sunlight exposure. Therefore, it is used in outdoor end uses: car top, upholstery, area rug, awning, and sail cover clothe. Outstanding wettability and quick drying ability of acrylic fibers make it be used to remove moisture from body surfaces in pile fabric, wipe fabric, and sportswear. Many products like fake pashmina and cashmere use acrylic fibers to create illusion of their feeling with its relatively low cost. However, the disadvantage of acrylic fibers is that pilling (or fuzz) easily occurs. Modacrylic fiber is similar with acrylic

fiber from their properties to end uses. However, modacrylic fiber has unique characteristic, flame resistance, unlike acrylic fiber. Generally, modacrylic fiber contains vinyl chloride as comonomer and chloride radicals, which act as radical scavengers, prevent flames.

In the 1960s, the researches about converting PAN fibers to carbon fibers (CFs) were tried in Japan and U.S. In 1961, PAN was firstly recognized as a suitable precursor materials for making CFs by Shindo. These research gradually changed the trend of carbon fiber market. In early stage of manufacturing CF field, rayon and pitch were mainly used for manufacturing CFs. However, currently most carbon fibers are currently being manufactured with PAN due to high carbon yield after heat treatment and high failure strength (6.6 GPa). As demand for carbon fiber reinforced polymer (CFRP) composites have been increased mostly in aerospace, wind power, and automotive fields, consumption of carbon fiber has been also increased since 1980s. Accordingly, wet-spinning of PAN has become important because PAN precursors greatly affect the final properties of carbon fibers.

1.2. PAN synthesis

The molecular weight (MW) and polydispersity index (PDI) of PAN have strong influence on properties of PAN fibers as well as solution preparation and spinning process. In wet-spinning process, normally used viscosity ($10 \leq \eta \leq 200$ Pa·s) of PAN is strongly dependent on such polymer properties [1]. Especially, MW determines the failure strength and application of the PAN fibers. For example, MW in 70,000 to 200,000 is usually used in textile field [2] and the PAN higher than those MW is usually used in carbon fiber field [3]. However, PAN with high MW causes bad

spinnability due to high viscosity and PAN with low MW causes broken filaments and bad drawability during the process. Conversion yield from monomer to polymer is also the important factor and more than 70% conversion is required to decrease the cost of PAN fibers. These factors (MW, PDI, and Conversion) are determined during polymerization. Radical polymerization, which is a representative method for PAN synthesis, is a chain reaction consisted of initiation, propagation, and termination. Radicals (formed from initiators) initiate polymerization by forming bond to monomers and the formed chains are lengthened itself by adding monomers continuously. Lastly, chains are terminated when the propagating chains react by combination or disproportionation (dead polymer chains). PAN can be synthesized *via* various free radical, ionic, or atom-transfer radical polymerization methods like bulk, solution , aqueous suspension [4], emulsion [3] and solvent-water suspension [5]. Recently, solution polymerization and aqueous suspension polymerization are most preferred processes for synthesizing PAN-based copolymers. PAN synthesized *via* aqueous suspension polymerization has high PDI [4] because molecular weight of chains gradually reduces due to monomer depletion and initiator termination as polymerization proceeds [6]. Moreover, acrylonitrile monomers have high reactivity in polymerization due to its highly polar nitrile groups so that makes synthesis of PAN having targeted MW and PDI very difficult. To resolve these problems, living radical polymerization like reversible addition fragmentation transform (RAFT) polymerization is preferred [6-8]. Unlike aqueous suspenstion polymerization, RAFT polymerization produces PAN having low PDI (<1.4) and high conversion (>70%) yield [9]. Almost all of RAFT is conducted in solution polymerization because RAFT agent is not soluble in water. In solution polymerization, monomer and synthesized polymer were simultaneously dissolved in organic solvents (aprotic

polar solvent with high dipole moment) such as N,N-dimethylformamide (DMF) and dimethyl sulfoxide (DMSO). Thus after finishing solution polymerization, excess non-solvent (methanol or distilled water) is necessary to remove solvent and simultaneously to acquire PAN as solid powder. However, in wet-spinning, reaction-finished polymer and solvent can be directly used as dope to be spun into fibers, which feature makes it more satisfactory over aqueous suspension polymerization in wet-spinning. Other living polymerizations such as atom transfer radical polymerization (ATRP) [10] and nitroxide-mediated polymerization (NMP) are also used for synthesizing PAN but they are not favor methods because it is difficult to remove metal agent from the polymer, which would be defects in PAN fibers during spinning process.

Usually, PAN homopolymer are not used in wet spinning solely because like previously said, PAN has strong secondary bonds (hydrogen bonding) due to high polar nitrile groups. So other comonomers polymerized with AN to satisfy various purposes. Addition of comonomers leads to easy polymerization (better control over MW and PDI) with reducing high reactivity of AN. Furthermore, copolymer enhances spinnability, drawability, and hydrophilicity during wet spinning process and solubility (dissolution) during solution preparation. Most of comonomers (e.g. methyl acrylate, itaconic acid, methacrylic acid, vinyl carboxylates, butyl esters, and propyl esters) [7, 11-13] impart increased drawability to polymer solution by lowering the T_g. These are functioned like plasticizers helping mobility and orientation of fibers improve. In fabrication of carbon fibers, commonomers play an important role during heat treatment. Comonomers having acid group (itaconic acid and methacrylic acid) lower the start temperature of stabilization (cyclization); oxidation is more easily occurred. Comonomers having carboxylate group boost

stabilization by promoting oxygen permeation to fibers. However, the content of these comonomers is limited less than 8 wt% because of low carbon yield problem after heat treatment. So Toray uses at least 92 wt% AN [14].

1.3. Solution preparation

Highly polar solvents are required for solvating PAN chains having strong dipole-dipole interactions (the secondary bonds): DMF, DMSO, dimethylacetamide (DMAc), aqueous sodium thiocyanate (NaSCN), aqueous zinc chloride ($ZnCl_2$), and ionic liquids. The most commonly used solvents in industry and research are DMF, DMSO, and DMAc. DMF provides fast and perfect dissolution of PAN while DMSO based solution is more homogeneous and more stable to the temperature change [15]. After choice of an appropriate solvent for PAN dissolution, proper polymer contents (solution concentration) should be chosen. When using middle-MW PAN (200,000 – 300,000), the concentration around 20 wt% is mostly selected. The higher the solution concentration, the lower the solvent diffusion gradient. So coagulation rate is low, which leads to circular fiber cross section and less voids. However, PAN with ultra-high molecular weight (> 1,000,000) is not spinnable with around 20 wt% concentration, so low concentrated solution (~ 6 wt%) is prepared and gel-spinning (extremely low coagulation bath included and other processes are same with wet-spinning) is used for spinning the solution [16]. For easy dissolution of PAN, normally temperature (70 to 100 °C) and stirring are simultaneously applied to PAN solution. The higher the temperature, the shorter the solvent (DMF or DMSO both) bridge between nitrile groups. In other words, solvation effect become lower and bonds between nitrile groups are reformed at high temperature (> 90 °C). As the

temperature increases, the color of PAN solution becomes darker yellow, which is attributed to the reformed nitrile-nitrile π bonds. Furthermore, the yield stress of PAN solution increases at higher temperature; the higher yield stress of PAN solution causes bad spinnability and drawability in wet-spinning. Youngho Eom et al. [15] explains this phenomena by presenting UV-visible absorption spectra, TGA, and rheological data. On the contrary, long stirring time provides exactly reverse effect to PAN solution [17]. As stirring time increases, the homogeneity of solution increases and the yield stress of solution decreases respectively. Bubbles or dissolved gases formed during the solution preparation should be removed because they can be voids or defects in the PAN fiber. Therefore, deaeration (degasing) is performed *via* vacuum oven and self-rotating centrifuge before wet-spinning [3, 18].

1.4. Wet-spinning process

Wet-spinning process is one of the oldest technologies for making micro-fibers from polymer solution. Polymer solution is extruded from multi-orifice nozzle, which is submerged inside coagulation bath, and it is coagulated. Phase separation occurs as a double diffusion in the coagulation bath: Inflow of non-solvent from coagulation bath to polymer jet and outflow of solvent from polymer jet to coagulation bath. During coagulation, polymer solute solidifies to form 1-D fibers. Subsequently, the fibers are stretched and consequently the orientation and crystallinity of the fibers are improved. Wet-spinning is a preferred method of making high-strength fibers because other spinning processes such as melt, dry, and electrospinning produce the fibers with voids and defects. Polymers used in wet-spinning mainly have strong secondary bonds (e.g. hydrogen bonding) between polymer chains and are therefore degraded prior to melting. In some cases, large amount of additives or plasticizers

are used to reduce the secondary bonds to enable the melt spinning process of the polymer. However, it is not recommended in spinning process because additives or plasticizers remain as defects in the fibers. Representative polymers for wet-spinning are poly(acrylonitrile), poly(*p*-phenylene benzobisoxazole), polyamide, polyimide, chitosan, cellulose etc.

Wet-spinning device largely consists of solution reservoir (or pump), coagulation bath, washing bath (or heat stretching bath), drying device, and winder. Among these, coagulation bath related process and parameters take the largest portion in determining final properties of PAN fibers. Coagulation bath is a mixture of solvent (DMF, DMSO, and DMAc) and non-solvent (mainly distilled water); the solvent concentration is generally higher than the non-solvent concentration (> 60 wt% for solvent). The parameters related to coagulation bath are coagulation bath composition (weight fraction ratio of solvent and non-solvent), coagulation bath temperature, jet stretch, and etc. These parameters eventually related to coagulation rates. Reasonably, as coagulation time increases, the solvent contents inside PAN fibers decreases [19-22]. As temperature increases, coagulation rate increases and saturation point of residual solvent inside the fibers are reached more quickly. At low temperature (< 0 °C) of coagulation bath, diffusion rate is restricted [23] and the inward rate of non-solvent is low when compared to outward rate of solvent [24]. The rate difference and extremely low diffusion cause different rate or different driving force of outward solvent in radial direction so bending occurs at some points with low rate or driving force of outward solvent (bean-shaped fibers are formed) On the other hand, soft skin formed *via* slow diffusion helps exchange of solvent and non-solvent smoothly and resultantly, bean-shaped fibers have high density and less voids [25]. In a certain temperature (generally 50 – 60 °C) of coagulation bath, the

density and failure strength have highest value. At high enough temperature (60 – 70 °C), diffusion rate increases more quickly at the fiber surface, so rigid skin-core structure is rapidly formed. Rigid skin causes loose structure due to a large amount of residual solvent in the core (outward solvent diffusion from the fiber to coagulation bath is prohibited by the rigid skin). The large amount of residual solvent is left as voids in the fibers and the fibers have poor mechanical properties. Furthermore, the fibers fabricated at high temperature of coagulation bath shows circular cross-sectional shape.

As mentioned early, the coagulation composition also has similar effect on coagulation rate like temperature [22, 26-29]. At high solvent concentration in coagulation bath, the diffusion process is slow due to low diffusion gradient. This produces a dense and compact structure like when applying the low temperature in coagulation bath but the cross-sectional shape of the fibers is circular unlike applying the low temperature in coagulation bath. However, at too high solvent composition in coagulation bath, PAN fibers re-dissolve from the surface so some depressions are formed on the surface (irregular and rough surface) [27]. While the solvent concentration is low (non-solvent concentration is high), the diffusion gradient is high, which leads to fast coagulation rate. The fast coagulation rate results in rigid skin-core structure like applying the high temperature in coagulation bath. In case of low solvent concentration, high non-solvent contents starts instaneous phase separation at the very outermost surface of the fibers; more rigid skin-core structure is formed rather than applying high temperature in coagulation bath. Therefore, the core remains as fluid-like materials. The highly rigid skin and fluid-like core cause the fiber to shrink, which finally induces bean-shaped cross section. Generally, PAN fibers, fabricated in high solvent concentration (> 70%) in coagulation bath, show

the highest mechanical properties and best microstructure information [22, 26].

Jet stretch is the ratio of the velocity of dope (extrusion velocity) from the nozzle over the first take up velocity while the PAN fibers go through coagulation bath. Jet swells in the coagulation bath due to inward diffusion of non-solvent and relaxation of PAN chains. Stretch in coagulation bath suppresses relaxation of PAN chains and disorientation of PAN molecules. So the fibers fabricated without jet stretch have voids due to disorientation and random coiled chains resulted from jet swell and radial expansion of the fibers. When jet stretch is low (< 0.5), the diameter of fibers is larger than fibers with high jet stretch (> 0.5) and jet stretch and diameter have invers linear relationship [25, 30]. Under below 1 of jet stretch, the fibers have higher crystal size, crystallinity, and density as jet-stretch increases [31]. Furthermore, the cross-sectional shape is more close to circular as jet stretch is more close to 1 [26]. However, in the range of jet stretch over 1, diffusion rate increases [19] and it causes rigid skin-core structure [30], which stops further diffusion between fibers and coagulation bath. Therefore, the cross-sectional shape is distorted to kidney (just like low concentration in coagulation bath case) and large voids remain from residual solvent in the fibers [25]. Most of all papers about wet-spinning of PAN select the jet stretch just below 1. However, other parameters (coagulation bath composition and temperature) overwhelm jet stretch [32]; other parameters have more influence on cross-sectional shape and coagulation process over jet stretch.

The shape and size of orifice in nozzle plays an important role in determining the cross-sectional shape of PAN fibers. The diameter of orifice is ranged from 0.05 to 0.5 mm and the size is selected based on targeting diameter of PAN fibers. Y-shaped orifice with a certain coagulation rate can produce triangular shaped PAN fibers and the fibers are used for lustre purpose or enlarging surface area (interfacial area) for

FRP purpose [33]. As coagulation rate decreases, the cross-sectional shape can be changed from triangular to circular with Y-shaped orifice nozzle. However, circular fibers are more preferred for fabricating carbon fibers because the stress is homogeneously distributed in all directions in the fibers during stabilization and carbonization. In other words, generally noncircular fibers cannot stand a tensile load in carbonization and even in spinning process rather than circular fibers [21].

After coagulation bath, the fibers go through various baths for washing and thermal drawing. Generally, each bath has gradually lower coagulation bath composition and higher temperature as fibers go through each bath. Stretch ratio also gradually increases according to each bath. Finally, the highest stretch ratio is applied to the fibers at the bath with the temperature usually around or higher than T_g (glass transition temperature: 95 °C) of PAN. At the T_g PAN chains become soft and flexible so it can be easily stretched. The stretching process with T_g is conducted mainly inside hot water or steam [34]. *Via* such multistep drawing, the commercial fibers are produced with stretch ratio of over 15. Thermal drawing increase the fiber axial orientation of the PAN fibrils and crystallinity. Thus, mechanical properties (failure strength and modulus) of the fibers also increase [25, 31, 35]. *Via* drawing process, fibers get smaller in radial direction due to stretching of PAN chains and collapsing of pores. The overstretched fibers have defibrillation and this causes early fiber breakage. Thus the maximum stretch ratio should be carefully determined. After that, the fibers are dried to remove residual solvent or non-solvent and the fibers are winded by winder.

For more stretching the fibers, postspinnig process is applied to the fibers under different chemical conditions. Specifically, removing surface defects, attenuating fiber diameter, and reducing molecular dipole interactions of nitrile groups are the

purposes of the process [36]. Removing surface defects and reducing molecular dipole interactions help the PAN fibers increase orientation and tensile strength [37]. In the field of manufacturing carbon fiber, the attenuating PAN fiber diameter, which is mainly targeted to 7 – 9 μm, and the reducing molecular dipole interactions help PAN fibers withstand tensile load and enhance more uniform thermal treatment (inducing more cyclization reaction by reducing exothermic heat) during heat treatment. Postspinning modifications have been conducted by coating or impregnating of chemicals in fibers and by stretching fibers in the chemicals or plasticizers. Various plasticizers and chemicals are such as DMF [36], DMSO, copper chloride, zinc chloride, hot steam, acetic acid [38], boric acid [39], succinic anhydride [40] , pottassium permanganate ($KMnO_4$) [41], cobalt sulfate ($CoSO_4$) [42], cobalt chloride ($CoCl_2$) [43]. All these materials are functioned as lubricants by reducing the dipole interaction between the nitrile groups in PAN, which leads to more stretching. Among these, the transition metal compounds ($KMnO_4$, $CoSO_4$, $CoCl_2$) form the conjugation bond between d shells in metal and electron from N of C≡N, which makes them catalyst for cyclization reaction during stabilization process as well as lubricants during the postspinning process. The postspinning process has been only conducted at lab scale but it has not been tried in commercialized-PAN manufacturing process because industrial process has been well established and the targeting mechanical properties of PAN fibers necessary in real application are already achieved. However, in order to obtain fibers with extremely high strength such as next generation carbon fibers, the gap between the achieved average tensile strength and the theoretical strength needs to be bridged. This can be done by using postspinning treatments at commercial scale.

1.5. Current-assisted wet-spinning

As mentioned in section 1.4, various researches about wet-spinning of PAN had been conducted. However, it has been successfully commercialized and its history has been almost 70 years. Therefore, studies on PAN wet-spinning, especially its parameters and optimization, have been well established and saturated. So it is just being used as intermediate step to produce carbon fibers and little research has been done on PAN wet-spinning itself. In the early 2000s when CNTs began to attract high attention, CNT-PAN composite fibers produced *via* wet-spinning was once in spotlight [44-49]. So far, electric current and potential have not been considered as a parameter in wet spinning at all.

The new concept introduced here, current-assisted wet-spinning, is world firstly tried at least in our knowledge. The main idea of applying electric potential in PAN solution come from electrospinning process. However, two processes (electrospinning and current-assisted wet-spinning) are totally different in some points: 1. Dimension of produced fibers (micrometer-sized fibers in current-assisted wet-spinning and nanometer-sized fibers in case of electrospinning), 2. The amount of applied potential (several tens of voltage in current-assisted wet-spinning and several ten thousands of voltage in electrospinning) 3. The amount of flowed electric current (microampere in current-assisted wet-spinning and nanoampere in electrospinnng), 4. Fiber forming mechanism (coagulation of polymer solution in current-assisted wet-spinning and electrostatic repulsion force on polymer solution in electrospinning). The current-assisted wet-spinning is conducted *via* simply applying electric potential. The electric current flows in polymer solution just before the polymer jet enters coagulation bath. So except the part of applying electric parameters, other parts of process are exactly same with ordinary wet-spinning

process like coagulating, washing, drying, and winding. Negative sockets and positive sockets were connected to the syringe plunger and nozzle, respectively, to apply potential to the polymer solution. The syringe barrel and the surroundings were intentionally designed to be electrically insulated so that potential or current only affect the polymer solution. Thus syringe plunger, nozzle, and syringe barrel are made of metal materials and polypropylene respectively. During the process, the applied potential is constant and the following current is also almost constant as a several hundred micro ampere (μA) during the entire spinning process. The purpose of the thesis is to investigate the effect of applied electric current on the mechanical properties of PAN fibers. General wet-spun and current-assisted wet-spun PAN fibers, fabricated under the same wet-spinning conditions, were compared in terms of materials' properties. Their differences are closely characterized through tensile test, thermogravimetric analysis (TGA), differential scanning calorimeter (DSC), gel permeation chromatography (GPC), X-ray photoelectron spectroscopy (XPS), nuclear magnetic resonance (NMR), scanning electron microscopy (SEM), wide-angle X-ray scattering (WAXS), small-angle X-ray scattering (SAXS), cyclic voltammetry (CV), and etc. Details would be explained in section 3 - 6.

2. Current-assisted process: Electrospinning

The current-assisted wet-spinning process could be born because the electrospinning experiments were preceded. Electrospinning process is the simple method to produce nanosized fibers. By applying high electric potential, the extra charges start to stack up on the surface of polymer solution and the repulsion force caused by stacked charges makes polymer solution be drawn into nanosized fibers. Due to small size of fibers, its specific area is extremely high. So the process has been used for various purposes like pharmaceutical, catalyst, filter, and energy materials. The interior structure of nanofibers could be controlled by phase separation induced by heat treatment or coaxial electrospinning. Herein, we introduced some coaxial electrospinning experiments. With proper nozzle design, multi layered and multi channeled nanofibers were fabricated and characterized.

2.1. Multi-layer coaxial electrospinning

2.1.1 Introduction

One dimensional (1D) nanostructures, such as nanowires, nanorods, nanobelts, and nanofibers, have been thoroughly investigated because of their unique material properties resulting from their unique dimensions and geometries [50]. Due to their long length, uniform diameter, and controllable compositions [51], electrospun nanofibers have been researched extensively using polymeric, ceramic, and metallic materials. For example, polymer nanofibers containing multiwalled carbon nanotubes, nanoclays, and graphenes have been reported as mechanically reinforced composites

[52-54]. Ceramic nanofibers made of SnO2, TiO2, and WO3 have been researched for chemoresistive gas sensors [55-57], and ZnO and poly(vinylidene fluoride) nanofibers were used to fabricate piezoelectric nanogenerators [58-60]. On the other hand, carbon/silicon, carbon/sulfur, and carbon/tin composite nanofibers have been suggested as potential candidates for lithium-ion battery electrodes [61-63]. To enhance the performance of the aforementioned nanofiber-based applications and demonstrate new multi-functionalities, there is a strong need for an efficient fabrication method for multi-layered nanofibers [64-67] .

The coaxial electrospinning process is one of the most facile manufacturing methods for multi-layered nanofibers, though many processing parameters (including surface tension, viscosity, electrical conductivity, interfacial tension, mutual miscibility, and mutual compatibility [68]) are involved in the optimization process. In our previous work, bi-layered carbon nanofibers (CNFs) were successfully manufactured using a combined material system (polyacrylonitrile and styrene-co-acrylonitrile), a specific nozzle system, and coaxial electrospinning followed by subsequent thermal treatment [69-72] . Due to their unique and tunable electrical and mechanical properties, CNFs have been used for photocatalysts [73], chemical sensors [74], and electrochemical devices (e.g., Li-ion batteries, Li–air batteries, supercapacitors, solar cells, and fuel cells) [75-79]. To date, bi- and tri-layered CNFs manufactured by coaxial electrospinning have been reported [80, 81]. However, we believe that additional multi-layered structures, beyond bi- and tri-layered structures, can further enhance the performance of nanofibers, motivating the current research on manufacturing tetralayered CNFs.

In this work, tetra-layered nanofibers were manufactured using the quadruple coaxial electrospinning process with a core-cut nozzle system. Double-tubular (or tube-in-

tube) CNFs with concentric cylindrical vacant channels were obtained by subsequent heat treatment. The microstructures of double-tubular CNFs were systematically investigated, focusing on their structural evolution resulting from layerwise fluidic behavior during coaxial electrospinning. Finally, nanoparticles were successfully incorporated between tubes in double-tubular CNFs, suggesting that tetra-layered nanofibers can provide a basis for developing new multi-functional 1D materials.

2.1.2 Experimental

Polyacrylonitrile (PAN, MW = 200 000 g mol–1, Misui chemical) and styrene-co-acrylonitrile (SAN, AN = 28.5 mol%, MW= 120 000 g mol–1, Cheil Industries) were used to manufacture double-tubular CNFs. Note that the former is one of the representative carbonizing precursors, while the latter is a thermally degradable polymer. *N,N*-Dimethylformamide (DMF, 99.5%, Daejung Chemical) was used as a common solvent for both PAN and SAN materials. Their concentrations were 20 and 30 wt%, respectively. To dissolve and homogenize the two materials (i.e., PAN and SAN) in DMF, the solutions were ultrasonicated for 5 h and further stirred at 80 °C for 5 h.

A quadruple coaxial electrospinning process was developed to produce tetra-layered nanofibers (see Figure 2.1(a)). To fabricate double-tubular CNFs later *via* a heat-treatment process, SAN/DMF and PAN/DMF solutions were alternatingly supplied to the coaxial nozzle, as shown in Figure 2.1(b); SAN/DMF was supplied to the innermost (center) and third nozzles, while PAN/DMF was supplied to the second and outermost (shell) nozzles. The needle gage of the innermost nozzle was 22 and that of the other nozzles was 17. The coaxial electrospinning parameters were set as fol-

lows: applied voltage, 18 kV; tip-to-collector distance, 15 cm; flow rates of the innermost, second, third, and outermost solutions, 0.25, 0.25, 0.50, and 1.00 mL h^{-1}, respectively.

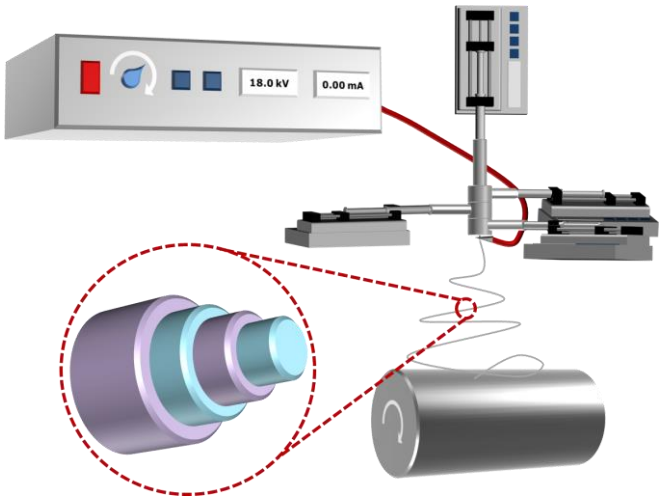

(a)

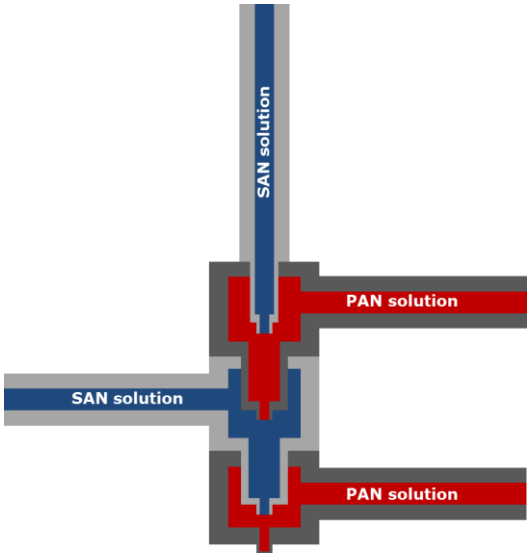

(b)

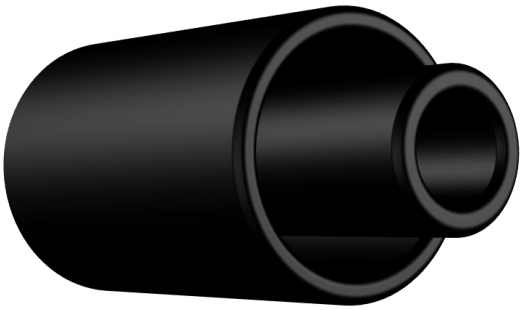

(c)

Figure 2.1. Schematic illustration of the quadruple coaxial electrospinning system. (a) Overall configuration of the coaxial electrospinning setup, (b) sequence of fluid supplied for manufacturing tetra-layered nanofibers and the configuration of the nozzles (so-called core-cut nozzle, where the inner nozzles are retracted inside the adjacent outer nozzle), and (c) a double-tubular CNF fabricated by subsequent thermal treatments.

The coaxial tetra-layered (SAN/PAN/SAN/PAN) nano-fibers were then thermally treated to remove the SAN com-ponents and carbonize the PAN components, producing double-tubular CNFs (see figure 2.1(c)). The oxidative stabili-zation of PAN was carried out at 270–300 °C for 1 h under an air atmosphere, and the carbonization process was conducted at 1000 °C for 1 h under a N_2 atmosphere. The ramping rates before the stabilization and carbonization were set to 10 °C min^{-1}.

The morphologies of the electrospun nanofibers were investigated using a field-emission scanning electron micro-scope (FE-SEM) (JSM-6700F, Jeol). The carbonized microstructures were investigated using Raman spectroscopy (Ar laser, wavelength: 514 nm, T64000, HORIBA), wide angle x-ray diffraction (WAXD) (wavelength:

0.154 nm, GADDS, Bruker), and high-resolution transmission electron microscopy (HR-TEM, JEM-3000F). The porous structure of double-tubular CNFs was evaluated using the Brunauer–Emmett–Teller (BET, Micromeritics ASAP2420) test.

2.1.3 Results and discussion

There are many parameters to be considered for the successful design of a multi-layered coaxial electrospinning system, such as material compositions of two or more solutions, sufficient applied voltage, optimal flow rates of each solution, and coaxial nozzle shape. PAN/DMF and SAN/DMF were chosen as the material compositions due to their mutual compatibility and immiscibility; additionally, these solutions have been used successfully to manufacture bi- and tri-layered nanofibers *via* coaxial electrospinning [69, 82]. The applied voltage was empirically determined as the lowest value that can form uniform, multi-layered nanofibers. The flow rates were determined by considering the coaxial electrospinning mechanism; i.e., the outer solution requires a higher flow rate than the inner solution because the inner fluid is produced within the nanofiber by the viscous dragging of the outer solution [82]. The quadruple coaxial nozzle system was empirically designed using a core-cut nozzle concept (see Figure 2.1 for detailed description of the nozzle). The end of the inner nozzle was retracted inside the adjacent outer nozzle, which was proven effective for reducing the jet instability and forming the core/shell structure due to sufficient transfer of the shear dragging force to the inner solution [83].

The SEM and TEM images of as-spun tetra-layered nanofibers are presented in Figures 2.2 (a) and (b). Figure 2.2 (a) shows that the nanofibers were uniformly prepared and their average diameter was measured as 1461.7 nm (±184.6 nm).

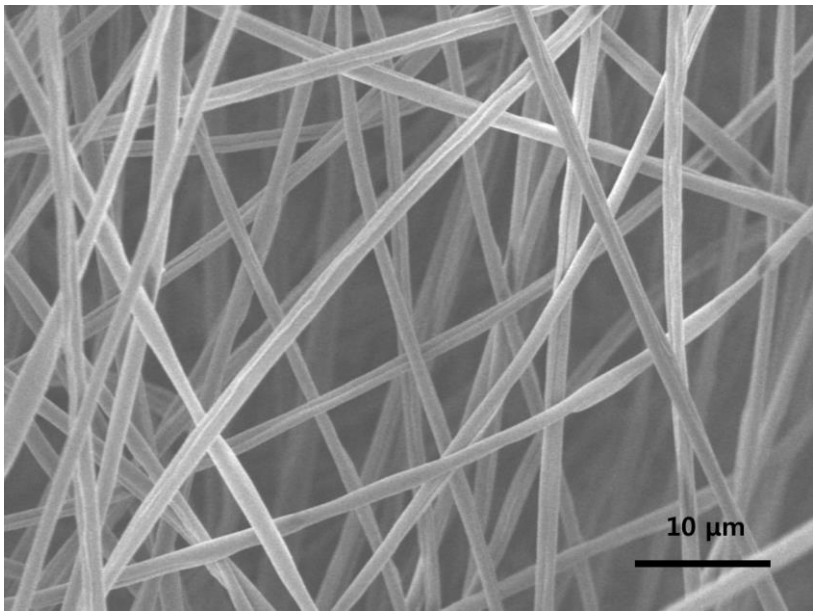

(a)

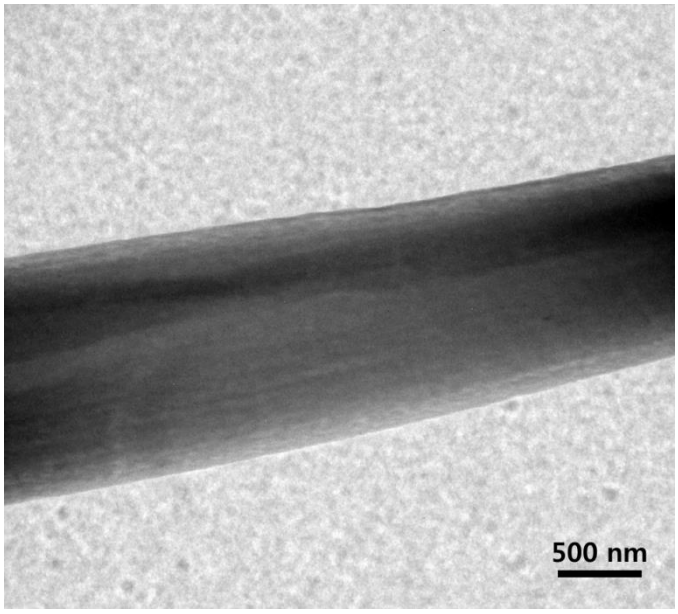

(b)

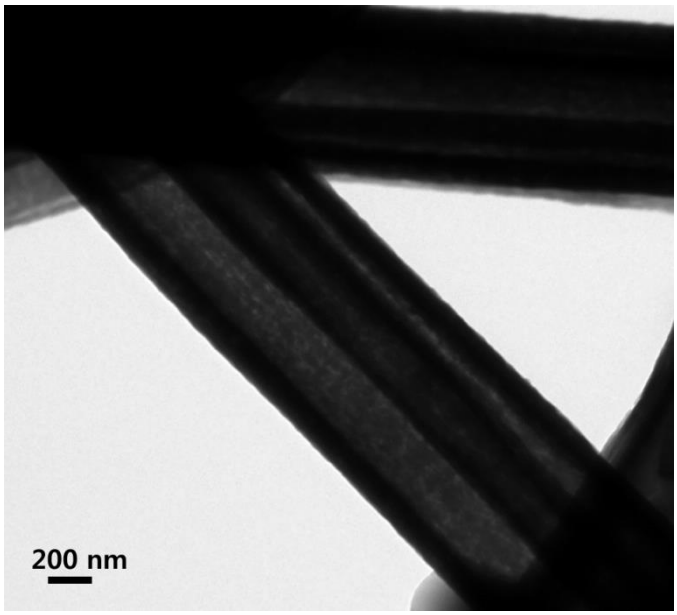

(c)

Figure 2.2. Electron microscopy images of the tetra-layered nanofibers: (a) SEM of as-spun tetra-layered nanofiber mat, and TEM of (b) as-spun and (c) selectively dissolved tetra-layered nanofibers.

At a glance, the multi-layered structure shown in Figure 2.2(b) is not clear due to indistinct boundaries between PAN and SAN. To observe the unclear boundaries between the layers, SAN components in the nanofibers were selectively removed using acetone. Note that the acetone selectively dissolved the SAN in the nanofibers. Consequently, the boundaries of PAN became obvious (Figure 2.2(c)), confirming that the multilayered nanofibers, with a perfect interface between layers, were manufactured successfully by the quadruple coaxial electrospinning process. The inner PAN nanofiber did not appear to be concentrically centered, because the SAN components had been removed in the third layers; i.e., the inner PAN layer had not been supported

and thus leaned towards the outer PAN layer.

Double-tubular CNFs were uniformly manufactured by heat treatment of concentrical tetra-layered SAN/PAN/SAN/PAN nanofibers (see Figure 2.3(a)). Their morphology and microstructure were systematically investigated. Figures 3(b)–(d) shows typical cross-sections of double-tubular CNFs.

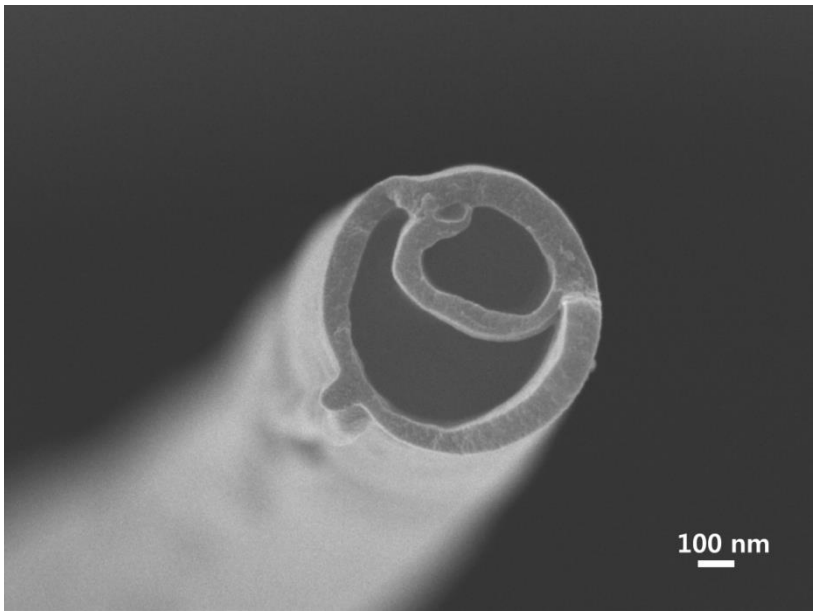

(a)

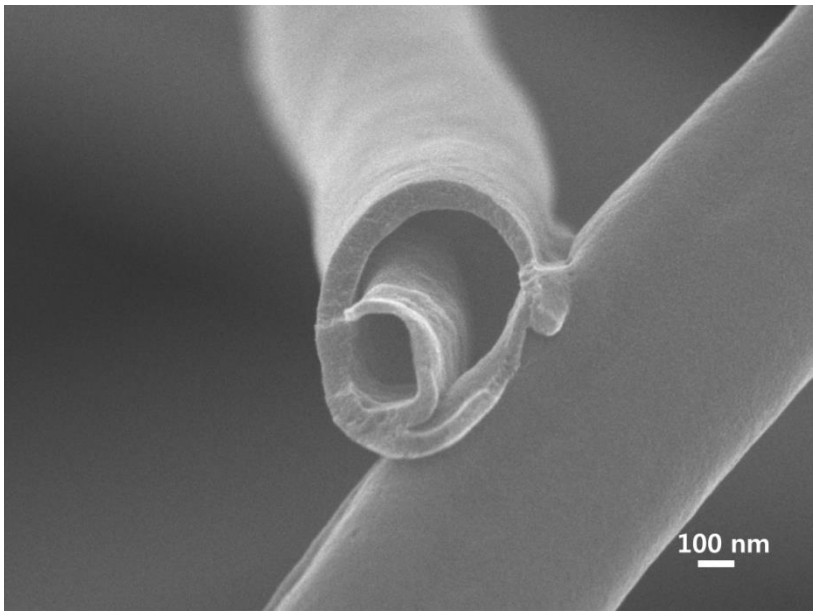

(b)

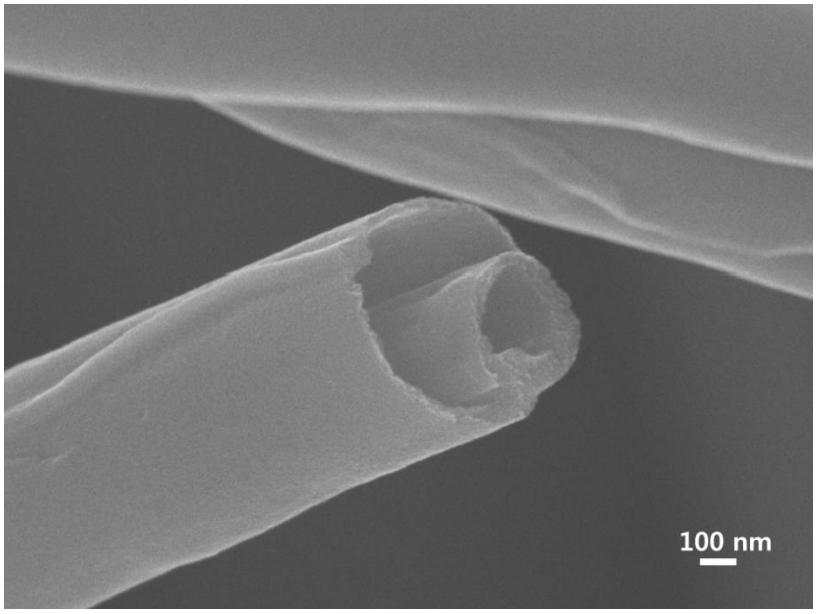

(c)

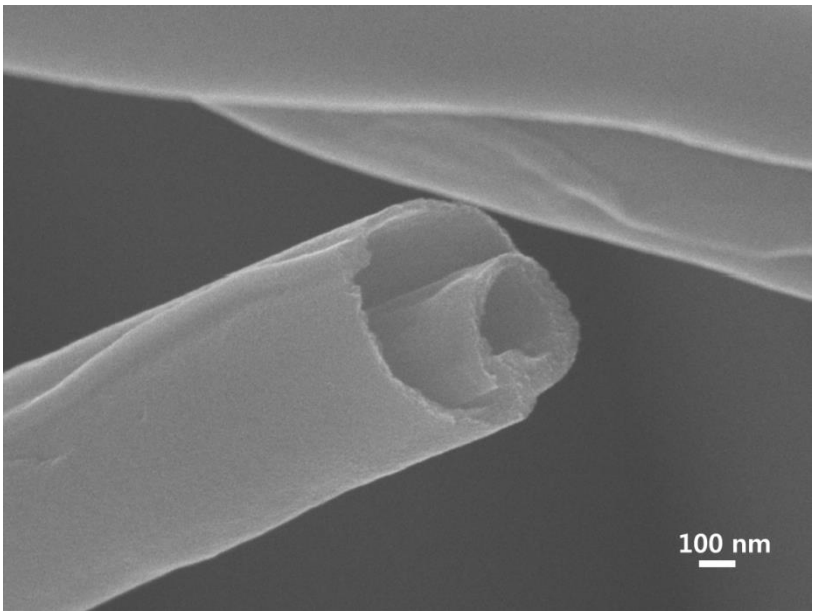

(d)

Figure 2.3. Typical FE-SEM images of the carbonized tetra-layered nanofibers: (a) low-magnification double-tubular CNF mat, and (b–d) high-magnification images of double-tubular CNFs.

The average outer diameters of the inner and outer tubes were 419.1 nm (±87.6 nm) and 767.3 nm (±98.3 nm), respectively. The ratio of the measured diameter of the inner and outer tubes was 1:1.83, which differed slightly from the target ratio (1 : 2). This was probably due to excess stretching of the outermost PAN layer during coaxial electrospinning . The measured wall thickness ratio of the two tubes was 1:1.46, which was also different from the target ratio (1:2.14). The wall thicknesses of the inner and outer tubes were 53.8 nm (±14.3 nm) and 78.3 nm (±29.6 nm), respectively. The average eccentricities of the inner and outer tubes (eccentricity: $(1 - b^2/a^2)^{1/2}$, where a and b are the lengths of major and minor axes on the ellipse) are 0.689

(±0.065) and 0.251 (±0.093). The cross-section of the outer tube was more circular than that of the inner tube; a smaller eccentricity indicates a more circular shape . Based on the morphologies discussed so far, the shapes of the tubes in the double-tubular CNFs were a result of the coaxial electrospinning mechanism, i.e., the more circular shape of the outer tube was attributed to the uniform charge distribution, while the oval shape of the inner tube resulted from unbalanced shear dragging by the outer fluid.

The microstructures of double-tubular CNFs were investigated by WAXD and Raman spectroscopy. The WAXD curve shows representative peaks of the turbostratic carbon crystals: primary ((002) at $2\theta = 24.12°$), secondary ((10) at 43.47°), and tertiary ((110) at 81.11°) peaks (see Figure 2.4(a)).

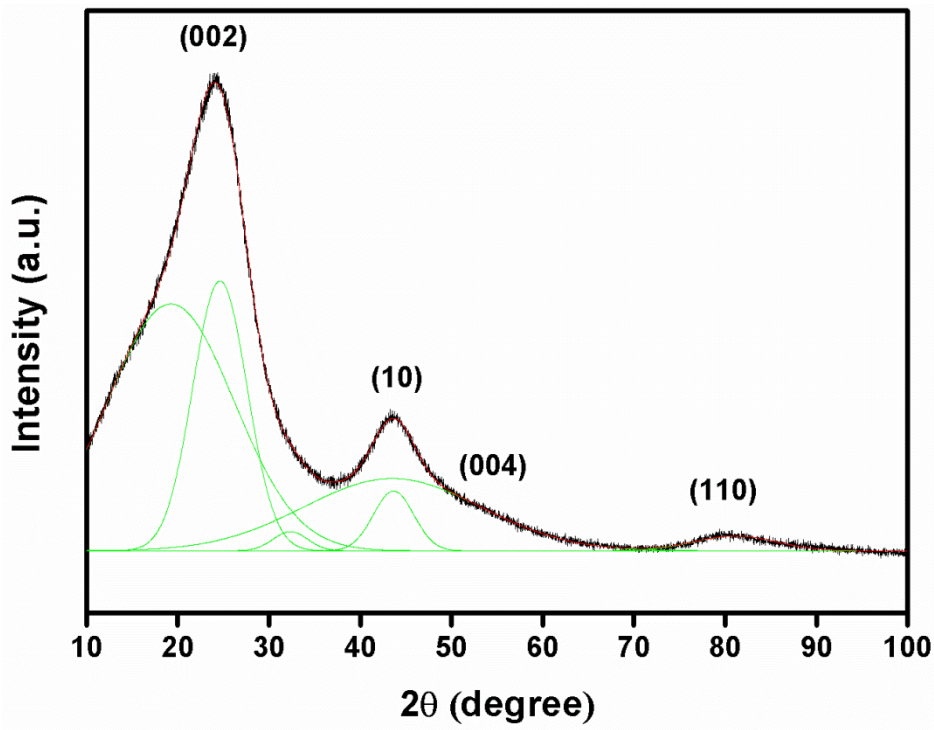

(a)

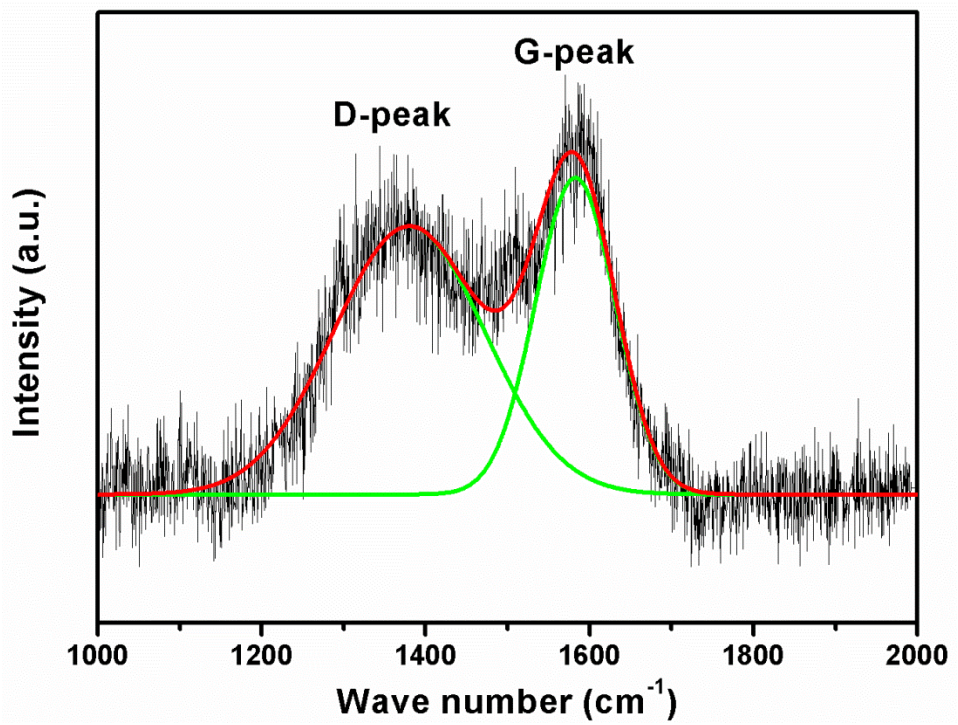

(b)

Figure 2.4. (a) WAXD curve and (b) Raman spectrum of the double-tubular CNFs.

A slight peak of (004) was also observed near 52.95°. For a more detailed analysis, the WAXD curve was deconvoluted using Gaussian peak functions. The (002) peak related to the turbostratic carbon was centered at 24.61° (note that the slightly up-shifted (002) peak center of the deconvoluted peak resulted from subtraction of the rare-carbonized fraction), and d002 was calculated as 0.361 nm using Bragg's equation. It is noteworthy that the peaks around 19.23° and 32.32° are mainly related to the incomplete carbonization of the PAN molecules [84]. The Raman spectrum in Figure 2.4(b) also indicates the successful formation of the turbostratic carbon structure. The primary peak near 1380 cm^{-1} (D-peak) is related to structural disorders in

the graphitic layers (i.e., diamond-like carbon), while the secondary peak near 1583 cm^{-1} (G-peak) represents the in-plane tangential stretch vibrational mode (E_{2g}) of the graphitic layer [69]. The Raman spectrum was also deconvoluted using Gaussian peak functions to calculate the integrated area ratio (I_D/I_G ratio). The ratio was 1.61, which is higher than that of the hollow CNFs thermally treated under the same conditions [70], implying a higher fraction of the disordered carbon structure. The less-ordered turbostratic carbon is attributed to the coaxial electrospinning process; i.e., the PAN molecules in the outermost layer were not fully stretched and recrystallized due to the resistance of the inner layer upon shear dragging, whereas the PAN molecules in the second layer from the center did not reorganize to the same degree because of shear dragging. The microstructure of carbonaceous materials strongly depends on the heat treatment temperature; thus, the microstructure of double-tubular CNFs will improve with a higher carbonization temperature or longer thermal treatment time.

The microstructure of the double-tubular CNFs was further investigated by HR-TEM. As shown in Figure 2.5 (a) and (b), the carbonaceous crystallites of the outer tube were much more developed than those of the inner tube. The carbonaceous crystallite size (La) of the outer tube (6.5 nm (±1.0 nm)) was significantly larger than that of the inner tube (4.4 nm (±1.7 nm)). The crystallite thickness (Lc, the number of carbon layers) of the outer tube (5.0 (±1.1)) was much greater than that of the inner tube (3.8 (±0.8)). To determine the degree of carbonization of the outer and inner tubes, the interlayer spacing values between the (002) planes (i.e., d002) were carefully measured. The outer tube shows better crystallographic quality: the interlayer spacing of the outer tube was in the range of 0.35–0.43 nm, more compact than the inner tube (0.35–0.50 nm) (see Figure 2.5 (c)). Overall, the carbonaceous crystallites of

the outer tube were significantly well developed compared to those of the inner tube due to the different stretching mechanism [82].

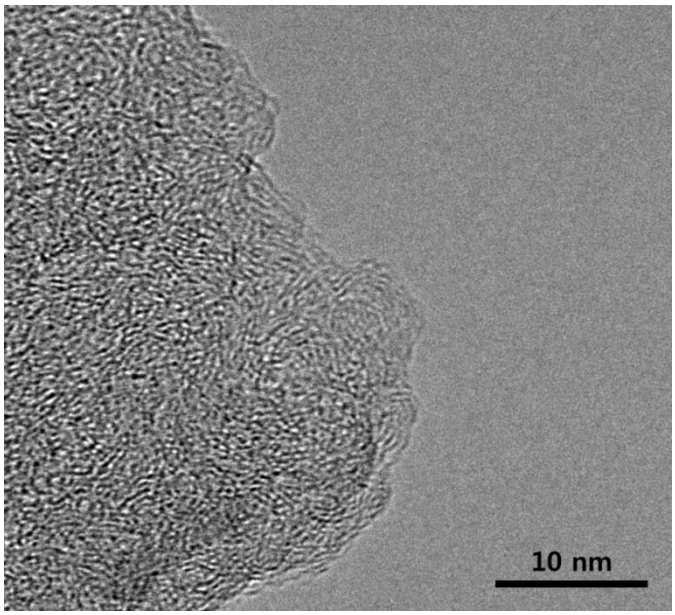

(a)

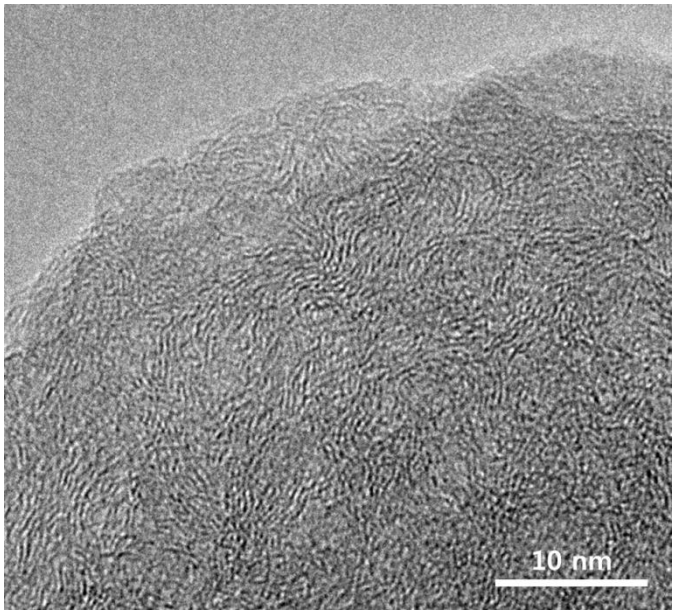

(b)

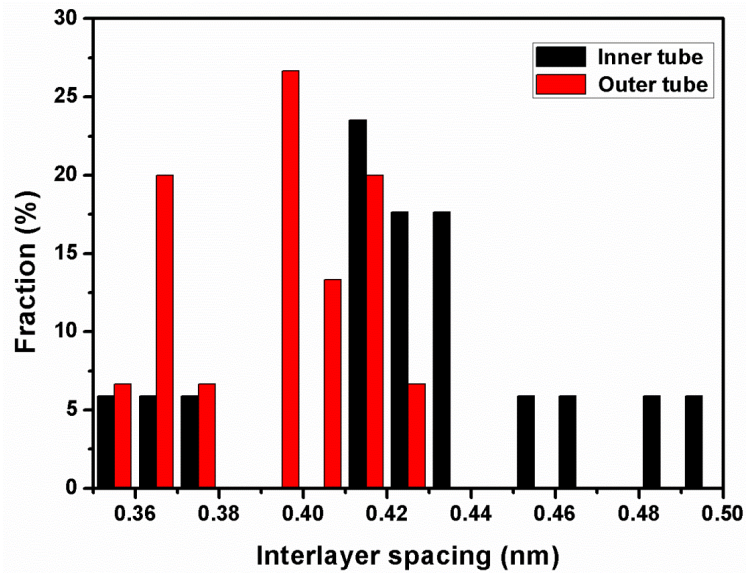

(c)

Figure 2.5. HR-TEM images of the double-tubular CNFs. (a) Inner and (b) outer tubes and (c) interlayer spacing distribution of the carbonaceous crystallites of the outer and inner tube in double-tubular CNFs.

The CNFs derived from PAN nanofibers through the carbonization process possess turbostratic carbon crystallites, non-crystalline carbons, and micro- or meso-pores [85]. In addition to crystal structure, the pore size and distribution of CNFs are among the most important parameters that affect microstructure and potential applications. The surface area and pore distributions of the double-tubular CNFs were characterized by BET and compared with those of hollow carbon nanofibers (HCNFs) and porous hollow carbon nanofibers (pHCNFs), which were prepared under the same heat treatment conditions reported in our previous work [71]. The BET surface area of the double-tubular CNFs was 50.04 m2·g–1, much larger than that of the HCNFs (13.18 m2·g–1) and pHCNFs (13.32 m2·g–1). The increased BET surface

area of the double-tubular CNFs compared to those of HCNFs and pHCNFs was attributed to the introduction of the inner tube and the decreased overall diameter and wall thicknesses. The total pore volume of double-tubular CNFs was 0.04095 cm3·g–1, larger than those of the HCNFs (0.02746 cm3·g–1) and pHCNFs (0.03915 cm3·g–1). In contrast, their average pore size was 3.27 nm, much smaller than those of the HCNFs (8.33 nm) and pHCNFs (11.76 nm). The nitrogen adsorption isotherm of the double-tubular CNFs in Figure 2.6 (a) shows the typical Type III (non-porous carbon) isotherm according to IUPAC classification [86]. The pore volume of micro-pores (0.105 $cm^3 \cdot g^{-1}$) in the double-tubular CNFs was much higher than those of the HCNFs (0.038 $cm^3 \cdot g^{-1}$) and pHCNFs (0.021 $cm^3 \cdot g^{-1}$) (see Figure 2.6 (b)).

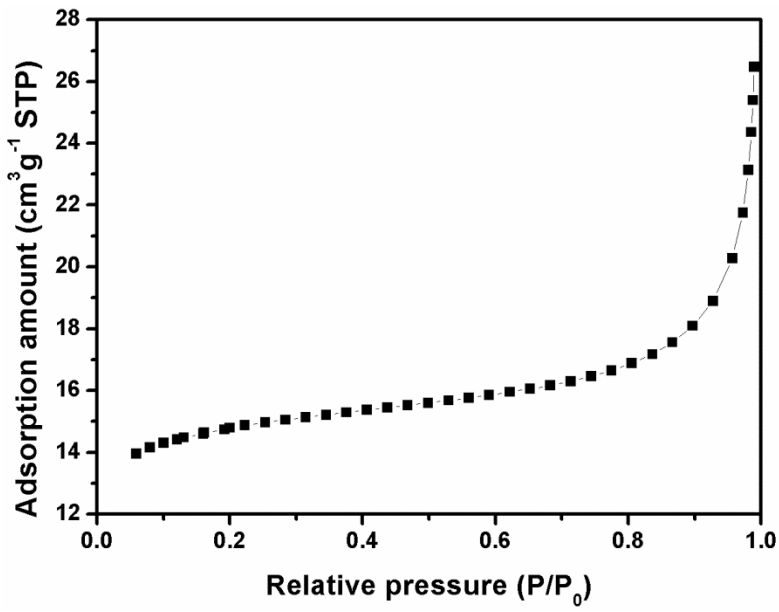

(a)

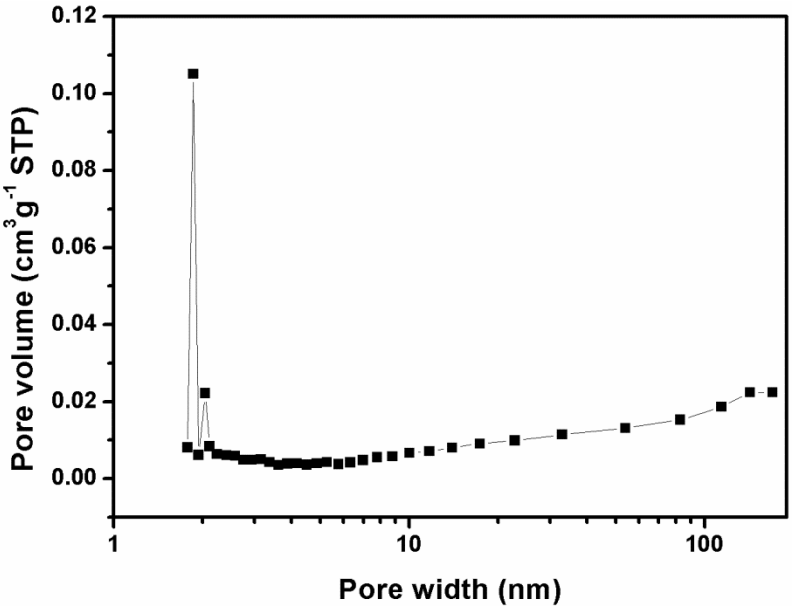

(b)

Figure 2.6. (a) Nitrogen adsorption isotherm of the double-tubular CNFs and (b) their pore size distribution (BJH desorption pore volume).

Basically, micro-pores in the double-tubular CNFs originated from the microstructural evolution of PAN. It is well-known that the oxidative stabilization and carbonization of the PAN nanofibers usually accompany the release of NH_3, HCN, N_2 gases, etc., resulting in the formation of the micro-pores within the carbon fiber structure [87]. The increased micro-pores of double tubular CNFs can be attributed to the better crystallized microstructure [87]. Note that the outer tubes of the double-tubular CNFs showed the more developed crystalline structures compared to the HCNFs: the crystallite thickness (L_c, the number of carbon layers) of the outer tube (5.0 (±1.1)) was higher than that of the HCNFs (4.6 (±0.8)), while the carbonaceous crystallite size (L_a) of the outer tube (6.5 nm (±1.0 nm)) was significantly larger than that of the

inner tube (4.5 nm (±0.9 nm)) [70]. Therefore, the more developed microstructure of the outer tubes brought about the increased micro-pore volume. On the other hand, the micro-pore volume was also affected by the release of the thermally decomposed SAN molecules. The micro-pore volume of the double-tubular CNFs was increased due to increased relative SAN/PAN ratio (0.225/0.250) compared to that of HCNFs (0.150/0.200) and the penetration of thermally decomposed SAN molecules in the innermost layer into both inner and outer tubes. In brief, the increased micro-pore volume resulted from the microstructural change of PAN and the increased effect of the thermally decomposed SAN molecules. Note that the low micro-pore volume of the pHCNFs (0.021 $cm^3 \cdot g^{-1}$) resulted from the pore coalition mechanism [71]. The large surface area and pore volume of the double-tubular CNFs make them interesting potential materials for electrodes of supercapacitors or cathodes of Li-Air batteries.

Lastly, double-tubular CNFs were prepared with nanoparticles located between their tubes to demonstrate the potential variants of double-tubular CNFs. Aluminum acetate (Al-ac, Sigma Aldrich) was incorporated between tubes of double-tubular CNFs. The PAN and SAN solutions had the same configuration explained in the Experimental section, except Al-ac (60 wt% SAN) was dissolved in the third SAN layer. The same electrospinning and heat-treatment conditions used for the previous double-tubular CNFs were employed. Figure 2.7 (a-b) clearly shows double-tubular nanofibers, the inner tubes of which were perfectly separated from the adjacent outer tubes. The double-tubular structure is shown in Figure 3; however, the inner tubes appear to be conjoined with the outer tube. This unified structure was likely formed during heat treatment because SAN layers were released, rendering the inner tube unsupported unless it leaned on the outer tube. The inner and outer tubes were then

bonded for the subsequent carbonization process. Al-ac dissolved in the SAN layer between the two tubes prevented the inner tube from touching the outer tube, floating it within the outer tube as shown in Figure 2.7. This method can be extended to manufacture multi-functional double-tubular CNFs having two concentrically arranged cylindrical channels; the same or different functional materials can be incorporated into these channels.

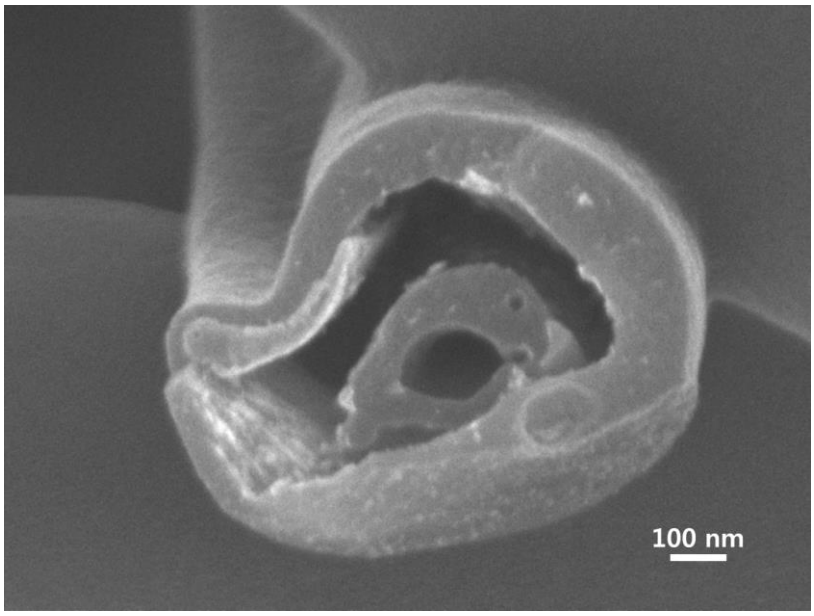

(a)

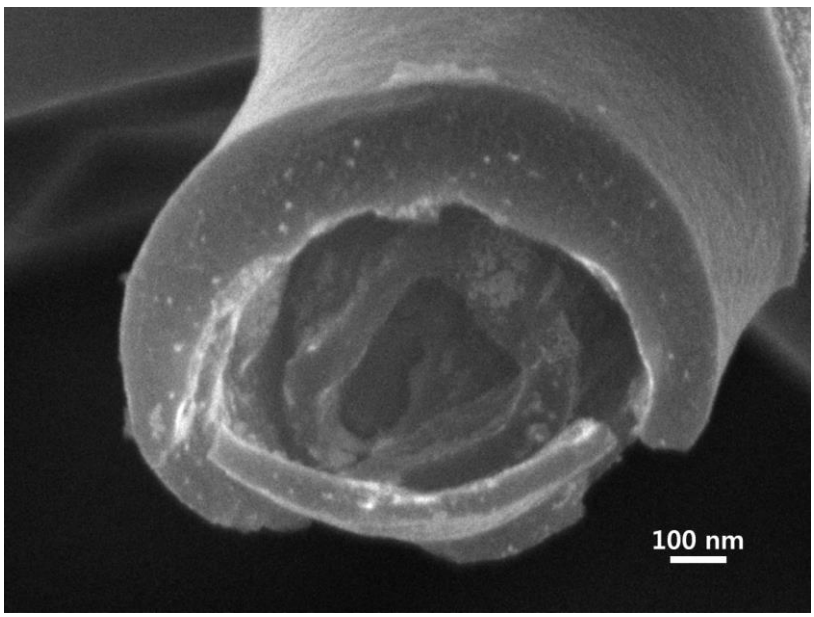

(b)

Figure 2.7. FE-SEM images of alumina nanoparticles incorporated double-tubular CNFs. (a) and (b) are arbitrarily selected images of the nanofibers manufactured using the same electrospinning conditions.

2.1.4 Summary

Concentrical tetra-layered SAN/PAN/SAN/PAN nanofibers were successfully manufactured using a quadruple coaxial electrospinning process. Through subsequent heat treatment, the tetra-layered nanofibers were converted to double-tubular (or tube-in-tube) CNFs. The mechanism behind the multi-layered nanofiber formation during coaxial electrospinning was determined. The outer tube of the double-tubular CNFs was stretched to a greater degree by electrical forces, whereas the inner tubes were shear-dragged by the outer fluid, resulting in denser carbon crystals in the outer tube than the inner tube. The BET surface area (50.04 m2·g–1) and total pore volume

(0.04095 cm3·g–1) of double-tubular CNFs, which were likely formed during the thermal treatment process due to the release of thermally decomposed SAN molecules, suggests the presence of a great number of micro-pores in the CNFs. Lastly, double-tubular CNFs with foreign materials incorporated between their tubes were prepared, demonstrating that the inner tube of double-tubular CNFs can be floated within the outer tube and multi-functional materials can be readily incorporated into those concentrical cylindrical channels.

2.2. Multi-channel coaxial electrospinning

2.2.1 Introduction

Recently, the rapid increase of the electric vehicular and the smart grid industries has been accomplished based on the optimization of the battery cell structure under the limited electrochemical reaction between the graphite anode and lithium layered cathode [88]. It is inevitable to employ the high capacity electrode materials to achieve further improvement satisfying the prevailing needs on the high-performance energy storage devices [89]. High specific capacities of the anode have been successfully delivered by researching on the silicon (Si) based negative electrode materials [90-92]. The volume expansion and rate performance problems also need to be addressed for the practical application of the Si based anode materials [93, 94], and those are the reasons why the low Si contents (<10 wt%) are mostly considered to design the commercializable anodes.

There have been tremendous number of reports on resolving the volume expansion [95-98] because the volume expansion issue is the inherent problem of the Si which

is intimately related to the high specific capacity [99, 100]. Meanwhile, the rate performance of the Si anode has not been much considered as the high specific capacity, the longer cycle life and the volume expansion problem. Therefore, we focused on the rate performance improvement of the Si anode in this work. In the previous works, the rate performances of the Si anodes have been improved on the basis of the kinetic effect by compositing with electrochemically inert materials: for example, titanium carbide due to its high electronic conductivity [101] and barium titanate due to its piezoelectricity [102]. Meanwhile, the augmented rate performances of the Si composites with electrochemically active materials such as tin (Sn) [103-107] or carbon (C) [72, 108-110] were recognized as the kinetic effect based on their excellent electronic conductivities. Since the supercapacitor electrode [111-113] and the hard carbon anode [114-116] demonstrated excellent rate performances in both the faradaic and non-faradaic reactions based on broad potential range electrochemical reaction, it could be conceived that the improved rate performances of the Si/Sn or Si/C composite materials can be not only resulted from the kinetic effect, but also from the thermodynamic effect attributed to the expanded potential range of the electrochemical reaction resulted from the multiple working potentials. By extension, the composite anode material consisting of multiple (≥3) active materials is expected to have the more improved rate performance.

In this work, Si/Sn/C ternary composite anode material was newly designed to improve the electrochemical performances and to elucidate the thermodynamic effect (expanded potential range due to Sn) in the rate performance improvement. The carbon not only contributes to the capacity, but also provide the conducting pathway and the structural mechanical support [72, 82, 108]. In contrast, the Sn and Si particles can only contribute to the capacity if they are embedded in a compartmentalized

space, so that the kinetic effect (electric conductivity improvement due to Sn) can be excluded from the point of Si. Thus, the double-holed carbon nanofibers separately filled with Si and Sn were designed to achieve the purposes explained above. Meanwhile, a separate-filling electrospinning process was developed in order to synthesize the designed anode material. It is well known that the electrospinning process is simple, efficient, and cost-effective technology to fabricate the highly controllable nanofibers [117]. The well-defined interior structures such as multi-layered [82, 118] or multi-channeled [119] cross-sections [70, 83, 118, 119] are enabled by employing the core-cut nozzle technology . Based on the material and processing designs, the well-compartmentalized Si/Sn/C ternary composite (*e.g.*, separately compartmentalized Si and Sn nanoparticles in double-holed carbon nanofibers (Si-Sn-DHCNF)) anode was successfully prepared. The electrochemical characterization of the prepared sample were thoroughly addressed from the point of thermodynamic effect (working potential) with the comparison to the reference samples (Si nanoparticles in double-holed carbon nanofibers (Si-DHCNF) and Sn nanoparticles in double-holed carbon nanofibers (Sn-DHCNF)).

2.2.2 Experimental

Solution preparations: In order to prepare the shell solution, poly(acrylonitrile-*co*-methacrylic acid) (PAN, 6% MA, MW: 80,000 g mol^{-1}, Polyscience) was dissolved in *N,N*-dimethlyformamide (DMF, purity: 99.5%, Daejung Chemical) with the concentration of 17.25 wt% and stirred for 3 h at 70 °C. The core solutions with Si and SnO_2 nanoparticles were separately prepared: 2 g of Si nanoparticles (Nanoshel) and 2 g of SnO_2 nanoparticles (Nanoshel) were dispersed in DMF using ultrasonication

for 3 h and poly(styrene-*co*-acrylonitrile) (SAN, 25% AN, MW: 165,000 g mol^{-1}, Sigma-Aldrich) was subsequently dissolved into the nanoparticle dispersed DMF solutions with the SAN concentration of 30 wt% and stirred for 3 h at 70 ^{o}C.

Synthesis and characterization: Silicon-tin-carbon ternary composite nanofibers were prepared by using a specially designed electrospinning system as shown in Figure 2.8. Si-SAN/DMF solution was provided to one core nozzle, while SnO_2-SAN/DMF solution was supplied to the other core nozzle. PAN/DMF solution was employed as the shell solution to drag the core solutions. The flow rates of core solutions were 0.25 ml/h, and the shell flow rate was 1.25 ml/h. Note that the SAN and PAN solution composition forms the stable cross-sectional geometry due to the immiscible and compatible interface, and the preceded core nozzle is beneficial to separate the core/shell fluid geometry formation and electrified jet protrusion at Taylor cone. The applied potential was 18 kV, and the tip-to-collector distance (TCD) was 15 cm. The binary composite reference samples consisting of silicon-carbon or tin-carbon were prepared using the same electrospinning condition including the flow rates, applied voltage, and TCD. The prepared samples were then thermally heat treated. The details on thermal treatments were described elsewhere. Briefly, the as-spun fibers were stabilized from 270 to 300 °C for 1 h under air atmosphere, and carbonized at 1000 °C for 1 h under Ar. The cross-sectional morphologies of prepared composite carbon nanofibers were examined by using scanning electron microscopy (SEM) (JSM-7600F, JEOL), and their internal structures were evaluated by transmission electron microscopy (TEM) (JEM-2100F, JEOL), energy dispersive X-ray (EDX) added on the TEM and wide-angle X-ray diffraction (XRD) (New D8 Adance, Bruker).

Electrochemical evaluation: The anode electrochemical performances of the prepared nanofibers were assessed by preparing two-electrode 2032-type coin-cells. The composite nanofibers were pulverized and mixed with binder (lithiated polyacrylic acid (Li-PAA)) solution in active material to binder at a weight ratio of 80:20. Then, the mixed slurry was screen-printed on Cu foil. The polyethylene separator (Star 20) and electrolyte consisting of 1.3 M $LiPF_6$ in a mixed solution of ethyl carbonate (EC), diethyl carbonate (DEC), and fluoroethylene carbonate (FEC) at a volume ratio of 2:6:2 were purchased from Asahi Kasei and PANAX ETEC, respectively. Li foil was used as a counter and reference electrode. The coin-cells were discharged and charged at a current density of 100 mA/g for investigating the cyclic performance, while the rate performances were examined by changing the charging current densities from 100 to 10,000 mA/g under consistent discharging current density of 200 mA/g between 0.01 and 1.5 V.

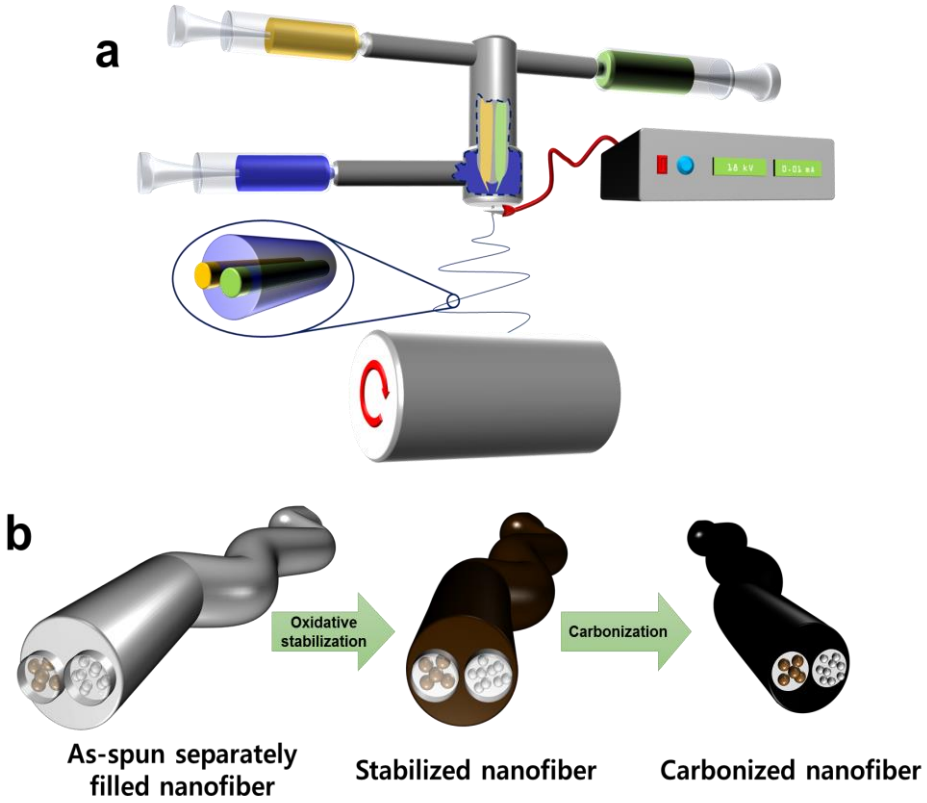

Figure 2.8. Schematic diagrams of (a) separate-filling electrospinning system and (b) expected cross-sectional morphologies of as-spun, stabilized, and carbonized Si-Sn-DHCNF.

2.2.3 Results and discussion

The compartmentalized structure is required to figure out the multiple working potential effect during charging process, so the separate-filling electrospinning setup in Figure 2.8(a) was prepared to make the well-compartmentalized nanofibrous structure. As previously reported, there are few requirements to synthesize the well-compartmentalized structure based on multi-channeled or multi-layered electrospinning

process: the immiscible and compatible core/shell fluid composition to form a clear core/shell structure [69] and the spatial separation of the core/shell interface formation and the Taylor cone development [83]. The separate-filling electrospinning system was designed based on those requirements. The yellow and green core fluids are individually fed through the core nozzles, and wrapped in the blue shell solution to form the patterned fluid. The patterned fluid is then electrospun into the patterned nanofiber by the high applied voltage at the outer nozzle, and the formed nanofiber is collected on the cylindrical collector.

The structural changes during thermal treatment are schematically described in Figure 2.8 (b). As-spun nanofibers fabricated by using the separate-filling electrospinning process are expected to have a compartmentalized polyacrylonitrile (PAN) cross-section which was separately filled with Si nanoparticle/poly(styrene-*co*-acrylonitrile) (SAN) and SnO_2 nanoparticle/SAN composites. The shell is transformed into the stabilized PAN by the oxidative stabilization including dehydrogenation and cyclization under an air atmosphere, and then carbonized under an inert atmosphere by the thermal treatment [118]. Meanwhile, the molten SAN preserve the core volumes during the PAN stabilization, and then the maintained volume is turned into the void space by the thermal decomposition of SAN during the carbonization [70]. The nanoparticles are immobilized in the core holes during thermal treatment [72]. As a result, the double-holed carbon nanofibers separately filled with Si and SnO_x nanoparticles (Si-Sn-DHCNF) is prepared. The Si-Sn-DHCNF is expected to enable the independent electrochemical reactions of Si and SnO_x due to the compartmentalized structure in terms of kinetics by electronic and ionic transports.

The cross-sectional scanning electron microscopy (SEM) images in Figure 2.9 (a-c) reveal that the carbon nanofibers have the robust double-hole structures filled with

the Si and SnO_x nanoparticles.

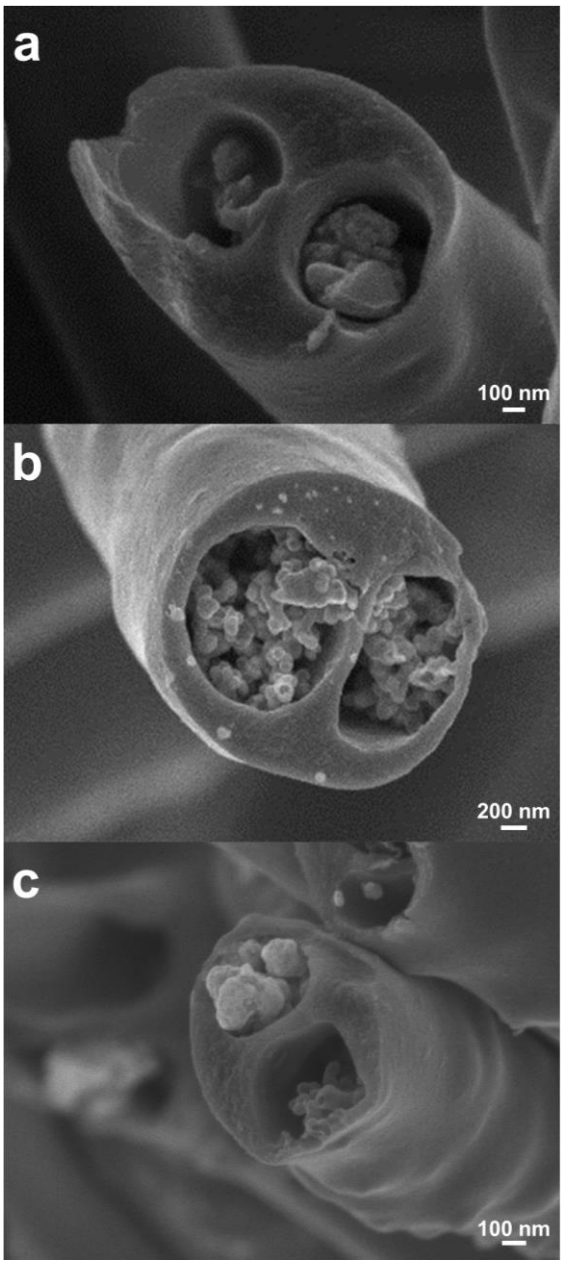

Figure 2.9. Cross-sectional SEM images of (a) Si-DHCNF, (b) Sn-DHCNF, and (c) Si-Sn-DHCNF.

Although the Si-filled double-holed carbon nanofiber (Si-DHCNF) and the SnO_x -filled double-holed carbon nanofiber (Sn-DHCNF) morphologies are highly analogous each other, the actual cross-sectional dimensions of the Sn-DHCNF such as average diameter (2082.59 nm (±251.33 nm)) and wall thickness of the thinnest part (102.38 nm (±31.08 nm)) are much larger than those of the Si-DHCNF (average diameter of 1342.69 nm (±203.09 nm) and thickness of 70.72 nm (±28.76 nm)) due to the high viscosity driven by the smaller nanoparticle diameter of SnO_2. Interestingly, the Si-Sn-DHCNF exhibited the smallest cross-sectional dimensions (average diameter of 1005.72 nm (±196.99 nm) and thickness of 54.61 nm (±22.00 nm)). The mechanism results in the reduced cross-sectional dimensions with two different core solutions should be carefully studied in the following work.

The compartmentalized morphologies were further examined by employing the transmission electron microscopy (TEM). Consistently to the cross-sectional SEM images, TEM and EDX mapping images of the Si-DHCNF revealed the discrete Si nanoparticles are well-encapsulated by the carbon framework (refer to Figure 2.10).

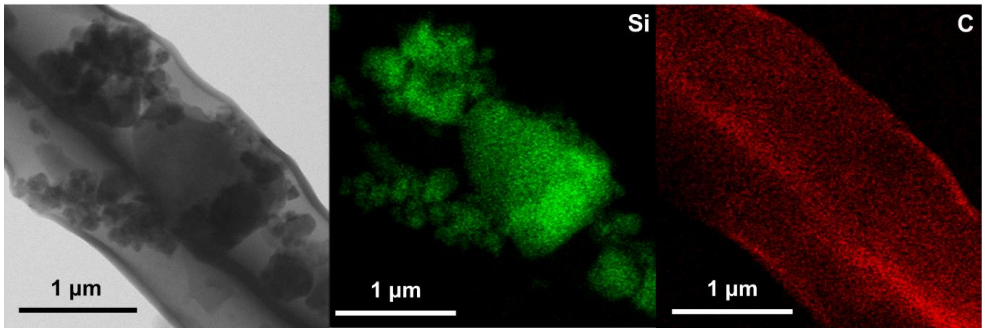

Figure 2.10. Separately filled Si-DHCNF: TEM image and its EDX profiles of Si and C atoms.

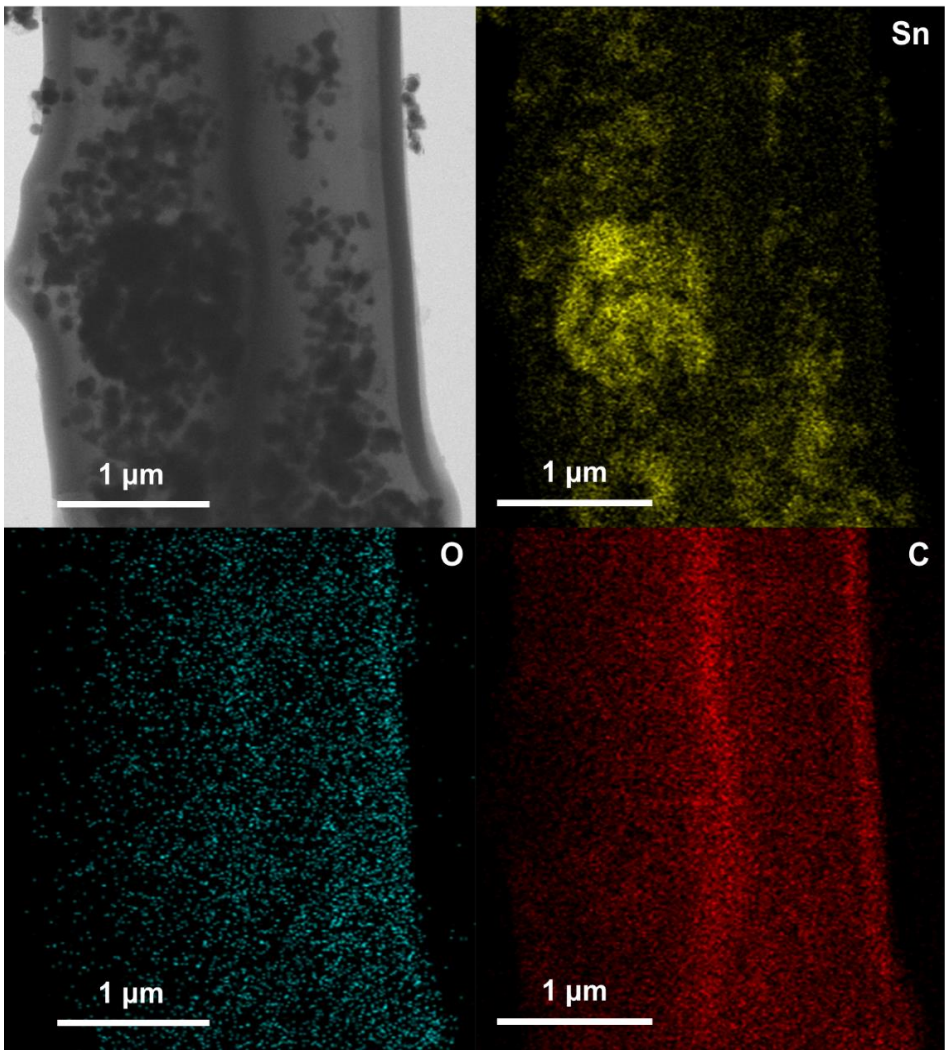

Figure 2.11. Separately filled Sn-DHCNF: TEM image and its EDX profiles of Sn, O, and C atoms.

Likewise, the TEM and its tin and carbon atom EDX mapping images of Sn-DHCNF

in Figure 2.11 clearly showed the well-developed double-hole structure filled with nanoparticles. Meanwhile, there was a significant discrepancy between the EDX mapping images of the tin and oxygen atoms at the Sn-DHCNF TEM image, indicating that the SnO_2 nanoparticles were substantially reduced into Sn by the carbothermal reduction during the thermal treatment since the carbonization temperature is much higher than the criteria (e.g, 600 °C) . The carbothermal reduction was initially onset by the solid-solid chemical reaction between the SnO_2 and carbon, and accelerated by the CO_2 and CO gaseous products. The detailed chemical reactions are represented by following equations [120]:

$$\mathrm{SnO_2}_{\ (s)} + \mathrm{C}_{(s)} \rightarrow \mathrm{Sn}_{(s,l)} + \mathrm{CO_2}_{\ (g)} \tag{1}$$

$$\mathrm{CO_2}_{\ (g)} + \mathrm{C}_{(s)} \rightarrow 2\mathrm{CO}_{\ (g)} \tag{2}$$

$$\mathrm{SnO_2}_{\ (s)} + 2\mathrm{CO}_{(g)} \rightarrow \mathrm{Sn}_{(s,l)} + 2\mathrm{CO_2}_{\ (g)}. \tag{3}$$

TEM image in Figure 2.12(a) reveals the shell structure is filled with different nanoparticles having different contrasts. The shell part is mainly consisting of carbon as it was expected, and the left-hand side core having darker particles was filled with tin, while the right-hand side core was occupied by silicon nanoparticles. Uniform distribution and weak intensity of the oxygen atom EDX mapping elucidates the tin oxide nanoparticles in Si-Sn-DHCNF precursor nanofiber was mostly reduced to tin by the same mechanism discussed above (see Figure 2.12(d-e)).

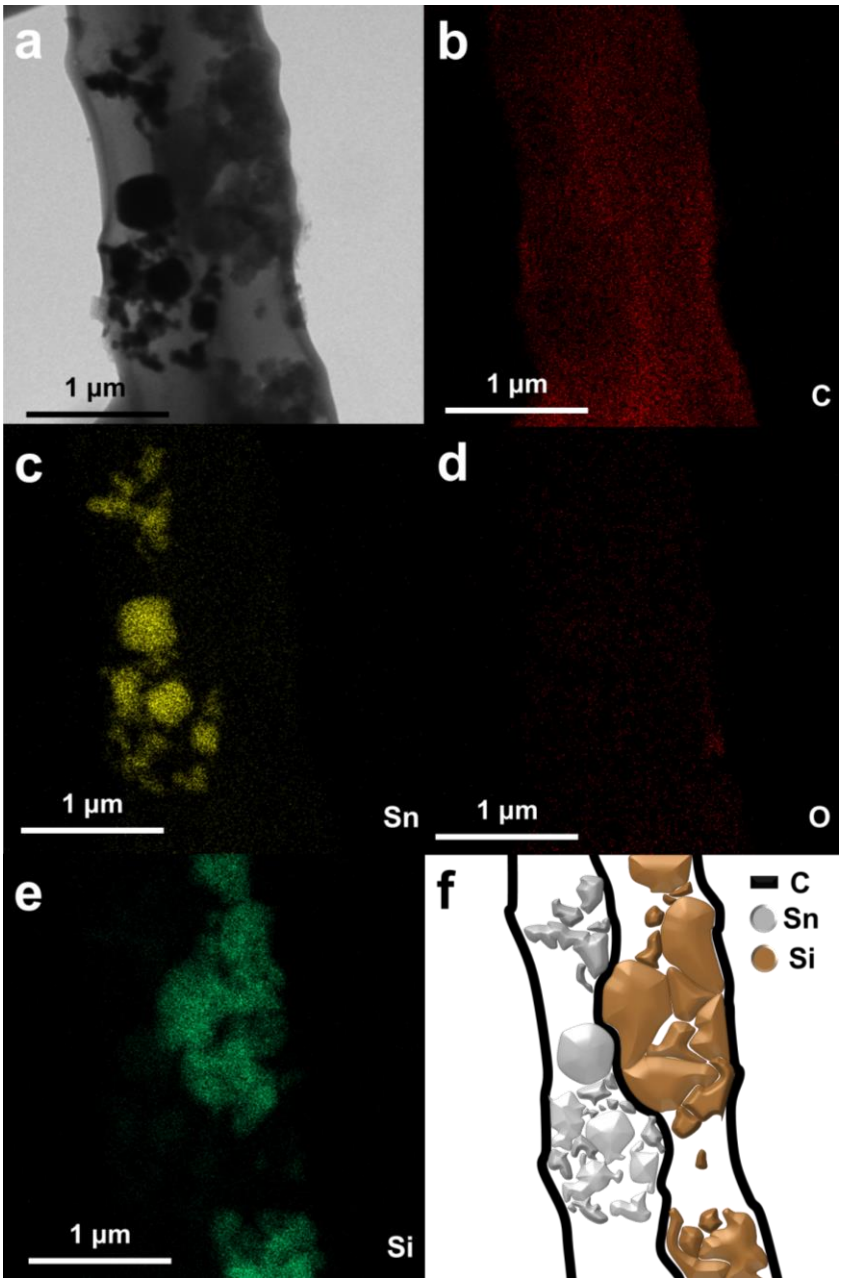

Figure 2.12. Separately filled Si-Sn-DHCNF: TEM image (a), its EDX profiles of (b) carbon, (c) tin, (d) oxygen, and (e) silicon, and (f) reconstructed atomic distribution based on EDX profile.

It is appreciable that the use of the SnO_2 nanoparticles prevents the agglomeration of tin particles during thermal treatment because the metallic tin can be easily agglomerated into large particles due to its low melting temperature 232 °C [121, 122]. Therefore, the atomic distribution can be reconstructed as shown in Figure 2.12 (f) by using the EDX mapping images.

The crystallographic structural characterization was conducted by using XRD in Figure 2.13. It is clear that the Si-DHCNF showed Si crystalline peaks of (111), (220), (311), (400), and (331) at 2θ = 28.4°, 47.5°, 56.2°, 69.2° and 76.3° . On the other hand, the Sn-DHCNF revealed not only significant metallic tin crystalline peaks of (200), (101), (220), (211), (301), (112), (400), (321), (420), (411), and (312) at 2θ = 30.6°, 31.9°, 43.9°, 44.9°, 55.3°, 62.5°, 63.8°, 64.5°, 72.5°, 73.2° and 79.5° [123], but also small SnO_2 rutile of (110), (101), and (211) at 2θ = 26.5°, 33.8° and 51.6° and SnO peaks of (101), (110), (002), (200), (112), and (211) at 2θ = 29.8°, 33.3°, 37.2°, 47.9°, 50.7° and 57.4° [92]. The ternary composite nanofibers (*i.e.*, Si-Sn-DHCNF) XRD curves demonstrated both crystalline Si and Sn peaks, and tiny peaks of unreduced tin oxide crystal peaks. Therefore, we could expect less irreversible capacity resulted from mostly reduced Sn compound. Tiny bumps with little intensities at around 25° corresponds to the carbonized shell structure [69].

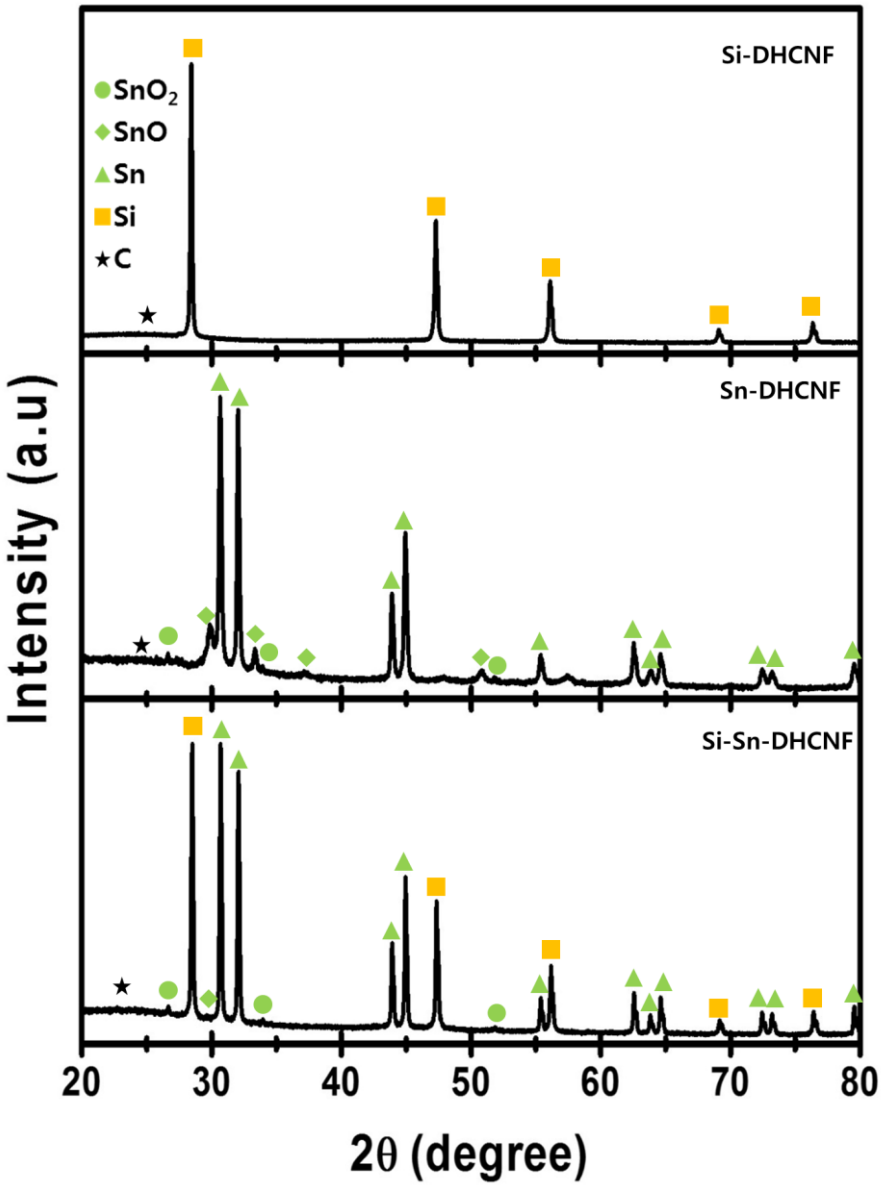

Figure 2.13. XRD profiles of Si-DHCNF, Sn-DHCNF, and Si-Sn-DHCNF.

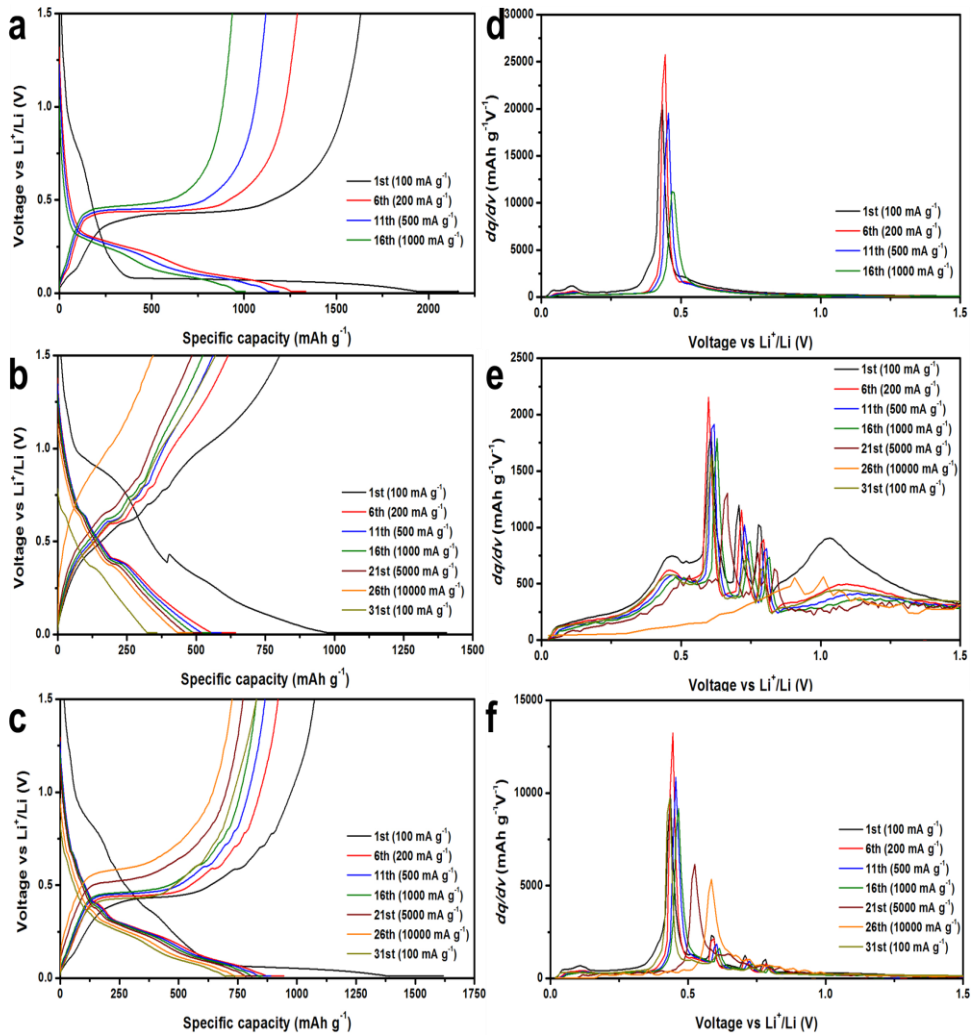

Figure 2.14. Rate performances of Si-DHCNF, Sn-DHCNF, and Si-Sn-DHCNF: voltage profiles of (a) Si-DHCNF, (b) Sn-DHCNF, and (c) Si-Sn-DHCNF, differential charge capacity curves of (d) Si-DHCNF, (e) Sn-DHCNF, and (f) Si-Sn-DHCNF.

The rate performances of the Si-DHCNF and Sn-DHCNF in Figure 2.14 reveals the pros and cons of the binary composite materials. The first discharge voltage profiles of Si-DHCNF in Figure 2.14(a) reveals the typical solid electrolyte interphase (SEI)

formation of CNF and Si nanoparticles from 0.75 to 0.62 V, and a long plateau at around 0.1 V corresponding to silicon amorphization by alloying with lithium and lithiation of the turbostratic carbon shell [72]. After the first cycle the alloying and dealloying plateaus of Li with Si were represented at 0.27 and 0.9 V during discharging and 0.45 V during charging . Huge hysteresis was observed in the Si-DHCNF voltage profiles and in high current density (over 1000 mA g^{-1}), the Si-DHCNF cell was not able to show the stable discharge behavior. This is because the Si nanoparticles were degraded at a glance. On the other hand, the Sn-DHCNF (Figure 2.14(b) and 2.15(a)) showed far lower initial coulombic efficiency of 55.80% than that of the Si-DHCNF (75.47%) because the oxygen atoms in the unreduced SnO_x crystals formed partially reversible Li_2O during first discharge around 0.9 V [124]. In the following cycles in voltage profiles (Figure 2.14(b)) revealed the multiple plateaus (0.65 and 0.4 V in discharging curves and from 0.4 to 0.8 V in the charging curves [105]) corresponding to the Li alloying/dealloying reactions with the metallic Sn [125]. The plateaus in charging curves were up-shifted (reaction voltage increased) as current density increased from 100 mA g^{-1} to 10000 mA g^{-1} due to the degradation while the plateaus in discharging curves stayed at almost same position due to CC (constant current) mode. However, when compared with Si-DHCNF, Sn-DHCNF showed the relatively less significant hysteresis of the Sn-DHCNF voltage profiles and the continuous operation of Sn-DHCNF cell even over 1000 mA g^{-1}. It elucidates better rate performance of the Sn-DHCNF. It could be conceived that the multiple plateau is more beneficial to the rate performance. For example, the broad potential range of electrochemical reaction such as the faradaic reaction in the hard carbon or the non-faradaic reaction in the supercapacitors resulted in the excellent rate performance [114]. In addition, the electronic contact of the Sn-DHCNF was expected to

be more robust than that of Si-DHCNF since the metallic Sn has the excellent electronic conductivity [126]. In Figure 2.14(c), the first discharge and charge capacities of the Si-Sn-DHCNF were 1619.0 and 1074.0 mAh g^{-1}, so the initial coulombic efficiency of the Si-Sn-DHCNF was calculated as 66.34%, which is exactly in the middle between that of Si-DHCNF and that of Sn-DHCNF. The SEI formation on the Si and Sn nanoparticle surfaces were cooperatively exhibited at around 0.8 V in the first discharge voltage profile of the Si-Sn-DHCNF (Figure 2.14 (c)). Meanwhile, the voltage profiles were also associated to the turbostratic carbon lithiation/delithitaion below 0.2 V [72] and the Si and Sn alloying/dealloying plateaus in a wide potential range from 0.2 to 0.9 V in the following cycles.

The differential capacity curves provide more quantitative information on the rate performances. The single Li-Si dealloying peak was shown at around 0.44 V in the differential capacity curves of the Si-DHCNF (Figure 2.14(d)), and the four typical dealloying peaks of Li-Sn (0.46, 0.6, 0.7, and 0.78 V [127]) and partial oxidation peak of Li_2O (1.155 V) [124] were exhibited in the Sn-DHCNF differential capacity curves (Figure 2.14(e)). All-peak potentials of Si-DHCNF and Sn-DHCNF were shown in Figure 2.14(f) (Si-Sn-DHCNF) and as current density increased, all peaks were right-shifted.

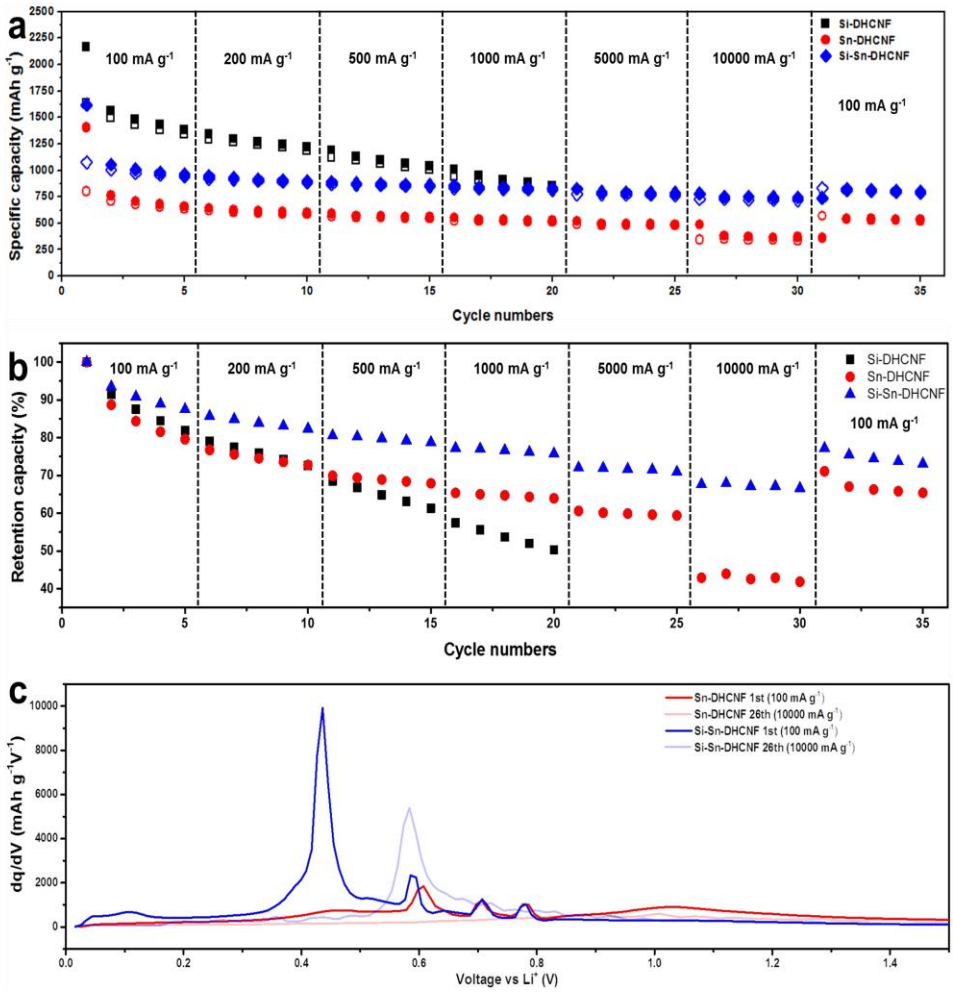

Figure 2.15 (a) Rate performance comparison, (b) their retention capacity comparison, and (c) differential charge capacity comparison at 1st and 16th cycles.

The Si-Sn-DHCNF showed the best rate performance (Figure 2.15(a)) and the best capacity retention (Figure 2.15 (b)) as cycles went through. Note that all three samples showed capacity deterioration at initial cycles (Figure 2.15 (b)); at lower rate (100 – 200 mA g^{-1}), rate retention reduction for the three samples is almost same with cycling retention reduction so rate retention reduction mainly attributed to the

repeated cycling while at high rate (500 – 10000 mA g^{-1}), the reduced capacities were resulted from high rate itself (Figure 2.16). Especially, Si-DHCNF showed severe capacity fading as current density increased because of high initial capacity and Si degradation.

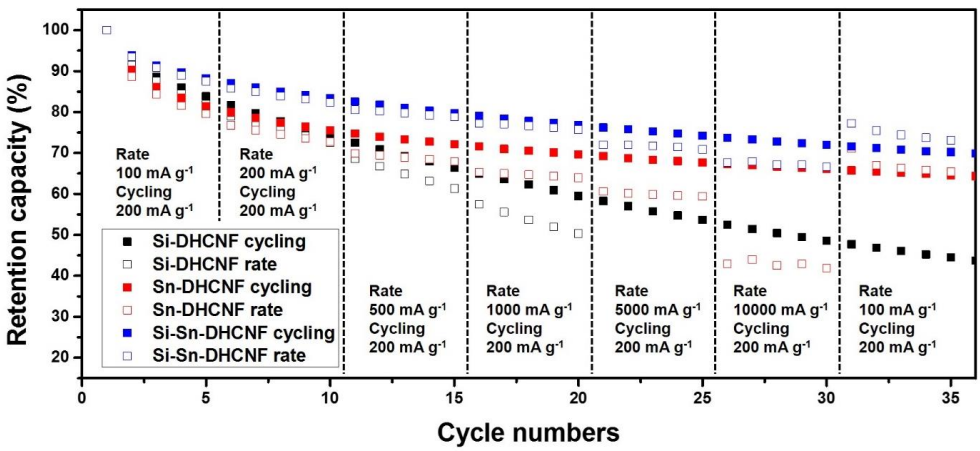

Figure 2.16. Retention capacity of rate and cycling performance comparison.

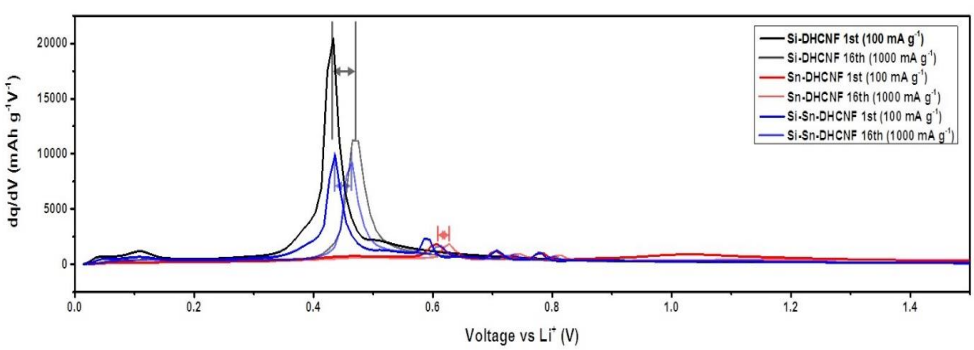

Figure 2.17. Differential charge capacity comparison at 1st and 16th cycles.

In Figure 2.17, the dealloying principal peak potential (around 0.6 V) shift of Li-Sn from the 1st cycle (100 mA g^{-1}) to 16th cycle (1000 mA g^{-1}) is less than that of the Li-Si around 0.44 V; $\Delta V = 0.021$ V for Sn-DHCNF and $\Delta V = 0.043$ V for Si-DHCNF. Meanwhile, in the case of Si-Sn-DHCNF, the reduced Si dealloying peak potential (around 0.44 V) shift ($\Delta V = 0.03$ V) from the 1st cycle (100 mA g^{-1}) to 16th cycle (1000 mA g^{-1}), which means more active Si nanoparticles remained with suppressed degradation of Si (generally degradation increases intrinsic resistance of electrode and thus increases reaction potential; V=IR). In Si-Sn-DHCNF 26th (10000 mA g^{-1}) curve in Figure 2.15 (c), one large peak was centered at around 0.6 V, where only Li-Sn dealloying reaction occurred, but the peak area (specific capacity) is larger than all-peak areas in Sn-DHCNF 1st or 26th. Thus, Li-Si dealloying reaction was also included in the peak in Si-Sn-DHCNF 26th. It could be interpreted that dealloying potential of Li-Sn extracted more dealloying reaction of Li-Si by holding back the potential just like CC (contant current) mode in charging. Note that Si-DHCNF was not reacted at all even at lower current density (5000 mA g^{-1}). Moreover, in Si-Sn-DHCNF 1st (100 mA g^{-1}) curve (Figure 2.15 (c)), Li-Sn dealloying peak was centered at lower potential (0.58 V) when compared with Sn-DHCNF 1st curve (Li-Sn dealloying peak was centered at 0.61 V). So these multiple dealloying potentials of Si and Sn affects each other by extending each other's reaction range. In the meantime, the Sn-DHCNF demonstrated a specific capacity of 344.2 mAh g^{-1} at a current density of 10,000 mA g^{-1}, which is comparable to commercialized graphite anode in current commercial Li-ion battery [102]. In brief, the high specific capacity and initial coulombic efficiency of the Si-DHCNF and the good rate performance of the Sn-DHCNF are the pros, while the poor cycling and rate performance of the Si-DHCNF and the low specific capacity and initial coulombic efficiency of Sn-DHCNF are the

cons, respectively. However, in Si-Sn-DHCNF, multiple reaction potentials of Li made more latent Si and Sn participated in reaction with Li, which might suppress cons of Si-DHCNF and Sn-DHCNF. Therefore, it is expected that well-designed Si-Sn-C ternary component anode exhibits the improved electrochemical performances due to the synergistic effect of Si and Sn.

2.2.4 Summary

The separately compartmentalized Si and Sn nanoparticles in double-holed carbon nanofibers (Si-Sn-DHCNF) was successfully prepared based on newly designed separate-filling electrospinning system to elucidate only the thermodynamic effect (expanded potential range). The cross-sectional and transmitted morphologies clearly revealed the Si and Sn nanoparticles asymmetrically filled in two holes formed in the carbon nanofibers. The use of the SnO_2 nanoparticle as a Sn nanoparticle precursor prevented the Sn agglomeration during heat treatment, and the carbothermal reduction enabled the successful formation of the metallic Sn under the high temperature carbonization. The Si-Sn-DHCNF showed the significantly improved electrochemical performances compared to the structured binary composites, and it is conceived that the electrochemical reactions under high current densities were facilitated by only cooperative electrochemical effect (*i.e.*, multiple plateaus in the voltage profile) because the ready-reported Si-Sn composite benefits such as good electronic conductivity and ductility of the Sn were completely excluded by compartmentalized structure in current material.

3. Wet-spinning process: Basic setup

Before current-assisted wet-spinning, basic wet-spinning experiments were necessary for deciding wet-spinning parameters. Various fiber's mechanical properties were shown in this chapter according to change of various wet-spinning parameters. In this chapter, largely two parts were introduced: wet-spinning for single filament and wet-spinning for multi filaments. All parts in wet-spinning for single filament were roughly self-designed. In wet-spinning for multi filaments, except syringe pump, syringe, and coagulation bath, other parts like 3-staged bath for washing and heat stretching, drying device, and winder were bought from the a manufacturer of wet-spinning machines.

3.1. Wet-spinning for single filament

3.1.1 Experimental

Figure 3.1. self-designed wet-spinning device for single filament.

Figure 3.2. Metal syringe for self-designed wet-spinning for single filament.

Figure 3.1 and Figure 3.2 showed the previous self-designed wet-spinning device and metal syringe for containing PAN solution. In a plant scale of wet-spinning, PAN polymer is synthesized by solution polymerization in reaction vessel and simultaneously, the synthesized PAN solution is used as dope for wet-spinning. Also, the reaction vessel serves also as a storage vessel for flowing PAN solution into coagulation bath *via* nozzle. These procedures are for reducing the cost of PAN fibers. However, in lab scale, small capacity syringe is used and contained PAN solution in the syringe is injected into the coagulation bath by nitrogen pressure or pressure. The syringe used in wet-spinning process was shown in Figure 3.2 and syringe barrel and syringe plunger were made of stainless steel. Syringe nozzle was made of brass to drill an orifice. The one orifice was drilled in the center of the nozzle with diameter of 400 μm (the orifice with a diameter less than 400 μm was technically difficult). Originally, syringe plunger had rubber O-ring at the end of the plunger to prevent leakage of PAN solution. However, the plunger with the O-ring made the air layer between the PAN solution and the plunger, and it was difficult to remove. Furthermore, the O-ring partially dissolved by DMF (solvent of PAN solution). So the rubber O-ring removed and only the groove, where once the O-ring was located, was left. As the syringe pump pushed the syringe plunger, the PAN solution just below the plunger was drawn into the groove and it was functioned as the O-ring. PAN solution was not leaked anymore due to solidified PAN solution in the groove. Coagulation bath consisted of solvent and non-solvent mixture and its weight fraction was 6:4 where many researches selected and recommended this fraction. The first roller for drawing the fibers in coagulation bath was set between heat bath, which was for washing and thermal stretching, and coagulation bath. The roller was covered with sand paper to prevent slip between the PAN fiber and the roller. The

heat bath was set on four hot stages to increase the temperature. The length of heat bath was 150 cm and it contained 40 kg of distilled water. Due to large amount of the distilled water, the heating time until targeting temperature of 90 °C (close to T_g of PAN) was taken about 1.5 h. In order to apply a temperature higher than 90 °C, the silicon oil was once put in the heat bath, but at 100 °C or higher, fiber breakage occurred frequently and it was very difficult to maintain a constant temperature due to absence of the sensor. Besides, the removal of silicon oil from the fiber was very difficult. So the experiments introduced here were conducted with heat bath containing distilled water. After heat bath, the fiber then went through drying section (consisted of hot stage covered by heat insulator, styrofoam) and finally wound up by winder. The single fiber from the single-orifice nozzle made it very difficult to handle the fiber during the process. Especially at high rate, fiber breakage frequently occurred even in careful handling. Therefore, the fiber was first guided to the winder with low rate, and then the rate of 1st roller and winder roller was simultaneously increased for stretching. Thus, the fiber initially wound in the winder roller was not used for characterization and only the fiber wound later in the winder roller was used for characterization.

Since the PAN solution preparation procedure was not completely set up, the PAN solution was prepared poorly. PAN (co-polymer with methyl acrylate 6 wt%, MW: 80,000, Polyscience) was used as received. The concentration of PAN solution was selected about 25 – 32 wt%. Due to high concentration of PAN solution, heating time was too long about 12 h and heating temperature was also high (100 °C). As I would describe later, this severe condition is not suitable for preparing PAN solution (see Figure 3.11 in section 3.2.2). The prepared PAN solution was poured with direct contact to the syringe's inner wall to suppress the formation of voids resulted from

perturbed flow of PAN solution. High viscosity from 25 – 32 wt% of PAN solution made it impossible to be spun at room temperature. Thus, the syringe containing the PAN solution was covered by hot tape to increase temperature. At around 70 °C, the PAN solution could be spun. The rate of 1st and final rollers were varies according to experiments. The air gap was introduced for dry jet wet-spinning and it was 3 cm. The fibers fabricated through dry jet wet-spinning generally showed higher mechanical properties because the stress, which is caused when polymer solution passes through a narrow die, is relaxed in the air gap.

3.1.2 Results and discussion

3.1.2.1 Solution parameters (concentration and flow rate)

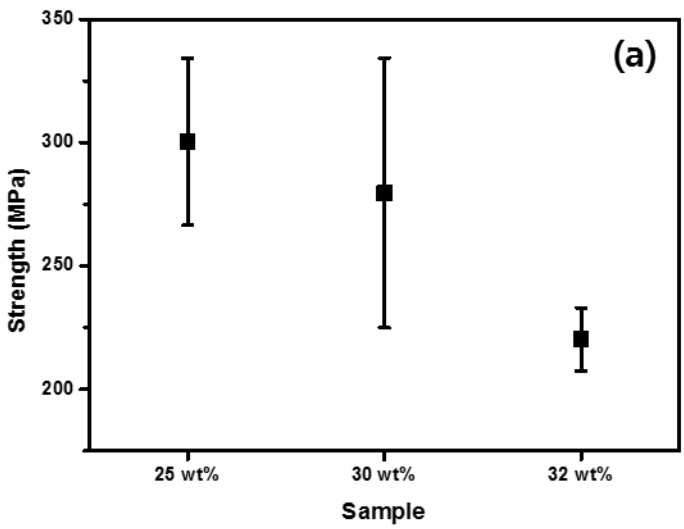

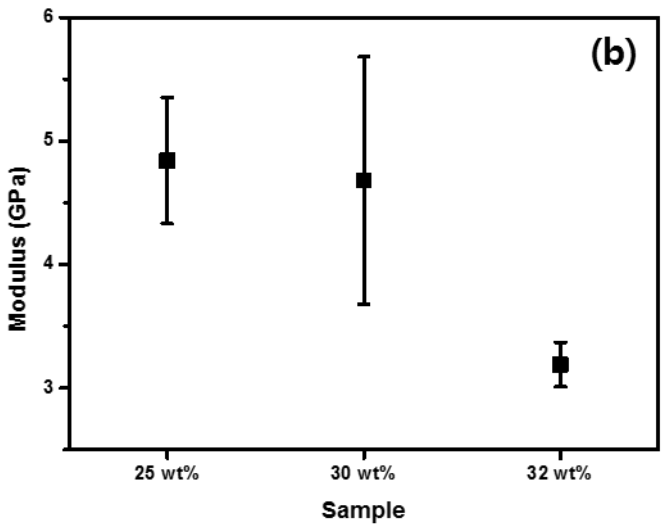

Figure 3.3. Mechanical properties of PAN fibers according to PAN solution concentration: (a) strength and (b) modulus.

Basically, the wet-spinning process was initiated without any stacking data. Therefore, all experiments in this chapter were conducted for stacking basic data (mainly relation between process parameters and mechanical properties) not for finding any close correlation between samples. Furthermore, note that the procedures of wet-spinning and PAN solution preparation in this chapter were not fully set up (optimization continued through various experiments). Firstly, at constant flow rate (7.6 ml/h) and constant drawing ratio of 5, the mechanical properties of samples with different PAN solution concentration were shown in Figure 3.3. For all samples, the constant drawing rate was applied so microstructure might be less developed in high concentration (32 wt%). Therefore the strength and the modulus of fibers decreased as concentration of PAN solution increased. When samples for tensile test were

prepared, instant adhesive was used to attach test sample with hard paper tab. Sometimes the thin adhesive was introduced, resulting in slippage between the sample (fiber) and the adhesive after ultimate stress (strength) was reached. This more frequently happened in thick fibers (> 50 μm). Thus, the strain was higher than the existing value so the strain data was excluded. In preparing PAN solution, the higher the concentration, the more difficult it is to dissolve in solvent, so higher temperature and longer heating times were required. This condition had bad effect on PAN solution by reducing solvation effect. Furthermore, due to high viscosity from high concentration, pouring PAN solution into syringe was difficult and perturbation of PAN flow formed bubbles during pouring. For these reasons, overall mechanical performance seems to be degraded as the concentration increased.

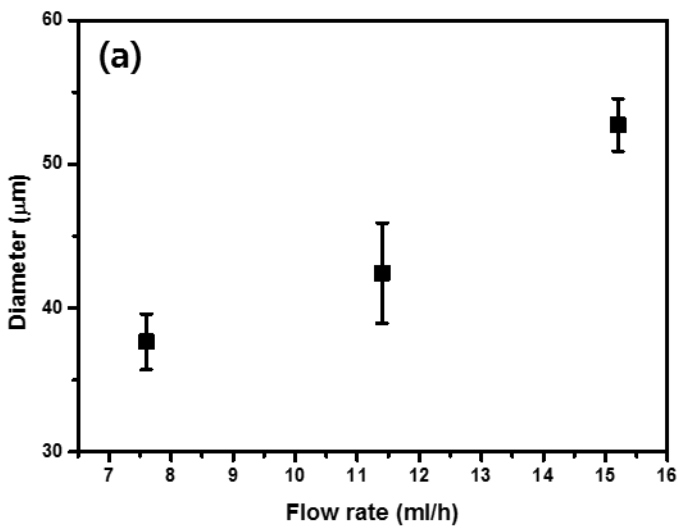

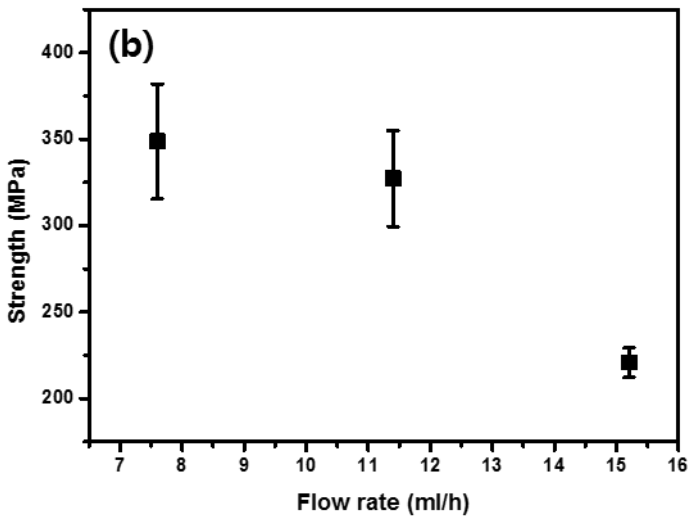
(b)
Strength (MPa)
400
350
300
250
200
7
8
9
10
11
12
13
14
15
16
Flow rate (ml/h)

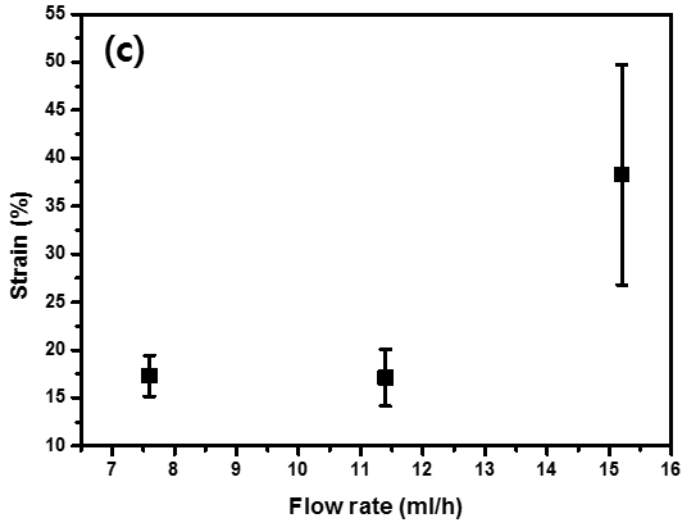
(c)
Strain (%)
55
50
45
40
35
30
25
20
15
10
7
8
9
10
11
12
13
14
15
16
Flow rate (ml/h)

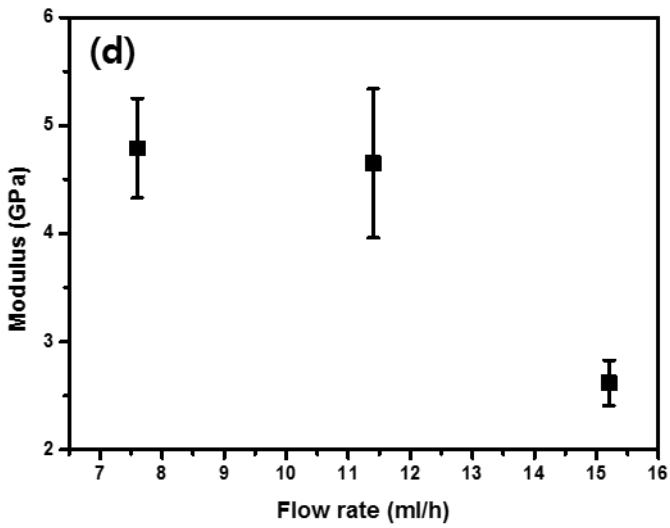

Figure 3.4. Mechanical properties of PAN fibers according to PAN solution flow rate: (a) diameter, (b) strength, (c) strain, and (d) modulus.

Fibers were fabricated by changing flow rate (7.6, 11.4, and 15.2 ml/h) and other parameters kept constant (concentration 30 wt% and draw ratio 5). Their mechanical properties were evaluated by tensile test (Figure 3.4). As flow rate increased, the diameter of fiber naturally increased. Strength increased with decreasing flow rate because polymer chains were more aligned at low flow rate rather than at high flow rate because of higher drawing force per unit area at low flow rate. Furthermore, the smaller diameter generally results in high strength even with the same failure load. Like Figure 3.4 (b) and (c), strength and strain showed revers relation. In case of flow rate, 15.2 ml/h, the failure strain of the fiber was very higher than other samples. When the tensile test sample was prepared, the sample was attached to hard paper tab with instant adhesive. For the same reason in Figure 3.3, the strain of sample

with 15.2 ml/h was much higher than other samples. The modulus of fibers were gradually decreased as flow rate increased. In the highly concentrated PAN solution (30 wt%), it was difficult to completely dissolve PAN solution and it is difficult to pour the solution without high temperature into syringe, which leads to formation of voids inside PAN solution. Because of these difficulties in high-concentrated PAN solution (27 – 32 wt%), the PAN concentration was lowered to 25 wt%. Accordingly, the flow rate increased to 19 ml/h to apply same draw ratio 5 like other samples; below 19 ml/h, the fiber was broken. Due to low concentration and high flow rate, mechanical properties were decreased (diameter 48.56 (2.74) μm, strength (176.49 (24.35) MPa), strain (14.45 (2.06)%), and modulus 3.21 (0.36) Gpa).

3.2. Wet-spinning for multi filaments

3.2.1 Experimental

Figure 3.5. Lab scale wet-spinning device.

In wet-spinning for single filament (section 3.1), the single fiber was frequently broken. Also, during the wet-spinning process, the size of the wind roller increased as the number of fibers wound on the roller increased, thereby increasing the drawing rate and reducing the diameter of the fiber. The fiber diameter more varied due to the eccentricity of the self-designed roller. Furthermore, due to the large orifice diameter (300 μm), large diameter fibers were produced and then, it was difficult to completely remove the solvent from the fibers and these points served as a point of lowering the mechanical properties (there was a high possibility that pores were formed). So new wet-spinning device was necessary.

New lab scale wet-spinning device was set up like Figure 3.5. From left to right side in Figure 3.5, syringe pump, coagulation bath, 3-staged washing bath, drying device, and winder made up the wet-spinning equipment. Syringe pump and syringe were self-designed to fit each other. Flow rate of PAN solution in syringe was controlled by the worm gear (2 mm) rate in syringe pump. Importantly, 100-orificed nozzle was used for experiment and diameter of each orifice and nozzle were 100 μm and 1.5 cm respectively. Because of dense space between each orifice, dry jet wet-spinning was impossible; each jet from the orifice was sticked together and finally, they were bunched as one polymer jet. Coagulation bath contains 15 kg of solvent (DMF) and non-solvent (distilled water) mixture and its composition is usually set as 6:4 in weight ratio (composition varies according to experiments). In 3-staged bath device, 1st bath is composed of solvent and non-solvent mixture at 5:5 weight ratio and the others contain only distilled water. Each bath temperature is 60, 70, and 90 °C respectively from the 1st to the last bath. Drawing ratio gradually increased from the 1st bath to the last bath (drawing ratio could be controlled in each bath respectively). The temperature in drying device was set as 120 °C and the roller rate in drying

device and winder rate were same with the last roller rate in 3-staged bath. Like section 3.1, the experiments here were conducted for stacking the basic data. And according to change in wet-spinning parameters, change of mechanical properties was mainly dealt with in this section.

PAN (co-polymer with methyl acrylate 6 wt%, MW: 80,000, Polyscience) and *N*,*N*-dimethylformamide (DMF, purity: 99.5%, Daejung Chemical) were used as received. PAN powder was dissolved in DMF at 25 wt% concentration at high temperature 100 °C for 12 h.

3.2.2 Results and discussion

3.2.2.1 Solution parameters (flow rate and solvation effect)

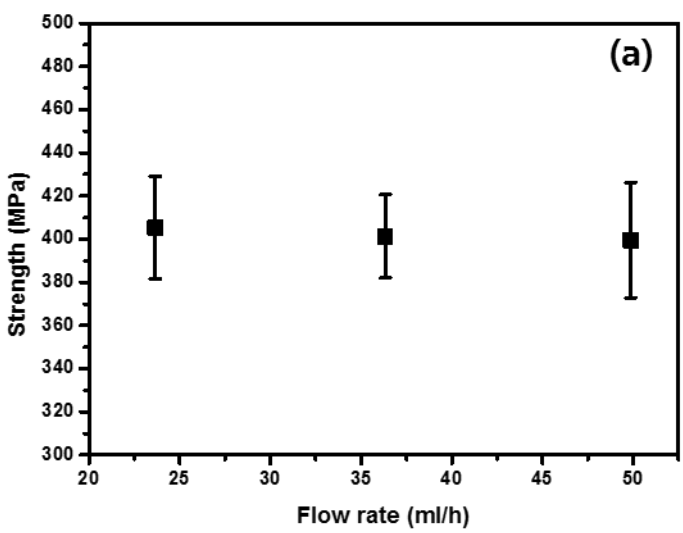

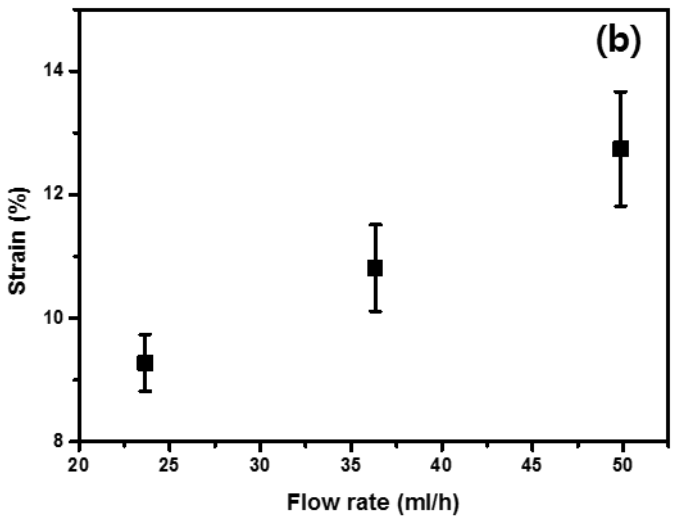
(b)
Strain (%)
14
12
10
8
20
25
30
35
40
45
50
Flow rate (ml/h)

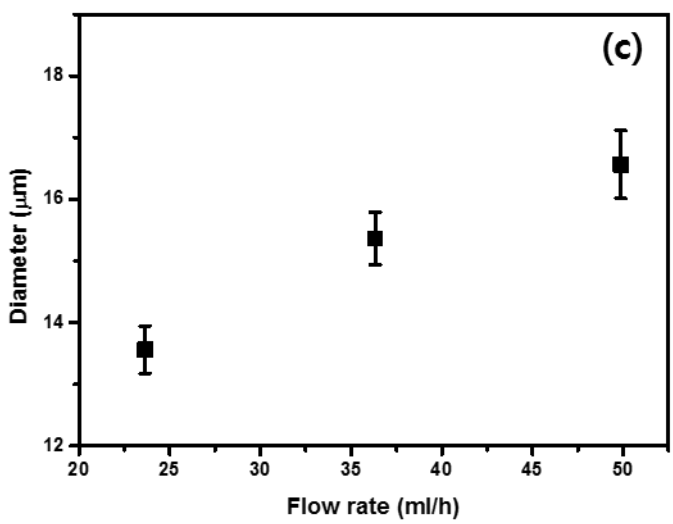
(c)
Diameter (μm)
18
16
14
12
20
25
30
35
40
45
50
Flow rate (ml/h)

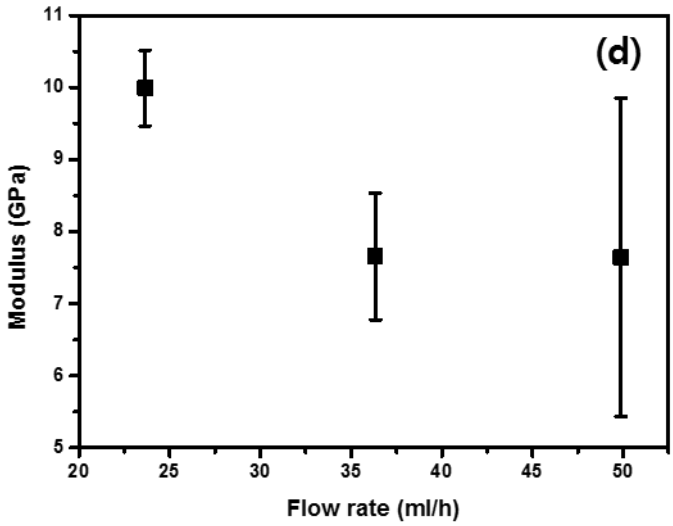

Figure 3.6. Mechanical properties of PAN fibers according to change in flow rate (23.65, 36.33, and 49.87): (a) strength, (b) strain, (c) diameter, and (d) modulus.

Flow rate was changed during wet-spinning process and at the same time drawing rate was also changed to make it possible to make PAN fibers with similar mechanical performance (concentration of PAN solution was 25 wt% for all samples). The fiber diameter fabricated *via* wet-spinning for multi filaments process more decreased than the fiber diameter (see Figure 3.6 (c)) fabricated *via* wet-spinning for single filament process due to low diameter of orifice (100 μm). The rate of all four rollers in 3-staged bath increased as flow rate increased (23.65, 36.33, and 49.87 ml/h). Representatively, the rate of the last rollers in each flow rate was 3.2, 5.2, and 6.8 m/min respectively. The strength of all samples was exactly same in Figure 3.6 (a). However, strain (Figure 3.6 (b)) and diameter (Figure 3.6 (c)) showed linearly increase relationship with flow rate. The high flow rate seems to

inevitably increase the diameter and strain. Only modulus deviated from tendency (Figure 3.6 (d)).

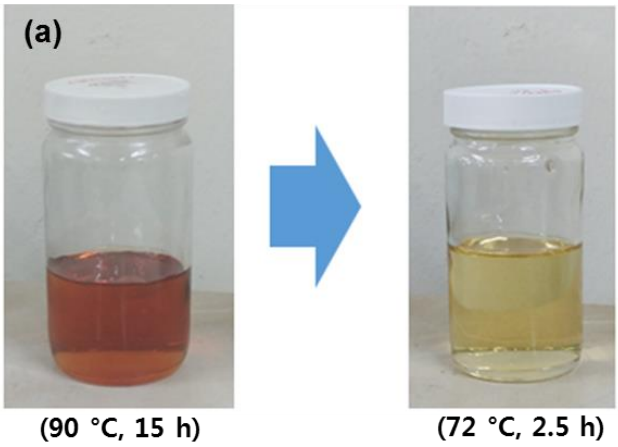

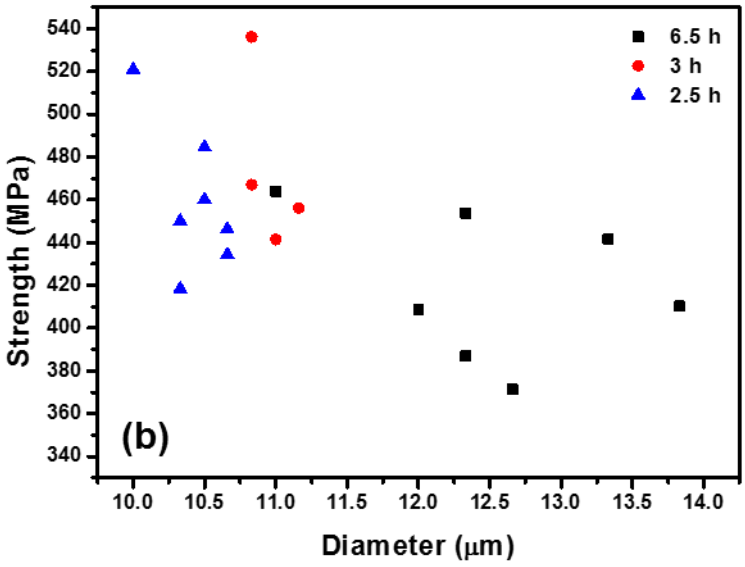

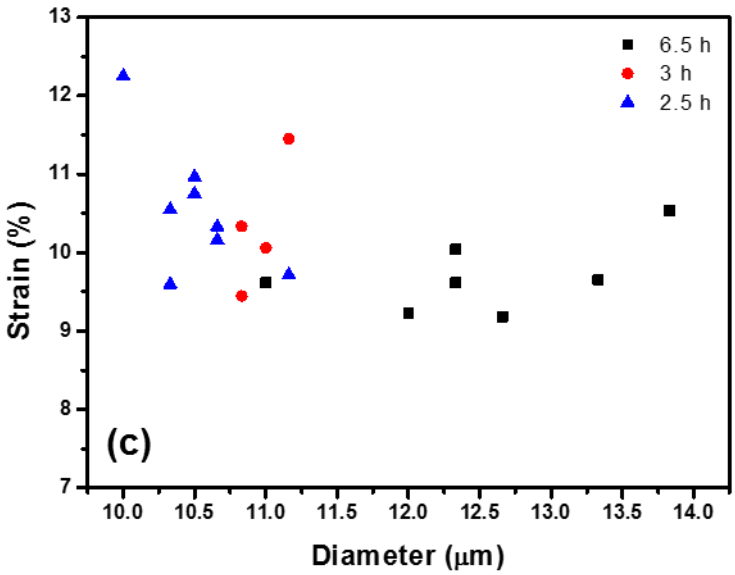

Figure 3.7. (a) color change of PAN solution (20 wt%), (b) strength VS diameter, and (c) diameter VS strain scattering plot according to heating time.

Heating temperature and heating time are important during PAN solution preparation. Figure 3.7 (a) showed the color change of PAN solution (20 wt%) according to heating temperature and time. As the temperature and time increased, the color of PAN solution changed into dark yellow. At the high temperature (90 °C) and the long heating time, the mobility of PAN chains increased and it makes the longer solvent bridge between nitriles groups shorter or direct coupling (strong secondary bonds) formed between nitrile groups [15]. The direct coupling bond enhanced the π-absorption and was functioned as a strong chromophore. So PAN solution, which was prepared at high temperature and had longer heating time, became dark yellow. This direct coupling bonds formation was observed not only in PAN but also in other

polymers such as poly(vinyl alcohol) (PVA) [128, 129]. It could be also observed in wet spinning process. Figure 3.7 (b) and (c) showed failure strength VS diameter and failure strain VS diameter scattering plot respectively according to heating time of PAN solution. Each point meant one test result of each sample. All fibers were fabricated with same wet spinning parameters except the heating time (heating temperature was 70 °C). As the time increased (solvation effect decreased), the diameter of fibers increased due to bad drawability resulted from more number of direct coupling bonds. As the time decreased (solvation effect increased), the failure strength increased because of smaller diameter of fibers and the failure strain kept almost constant.

3.2.2.2 Jet stretch effect

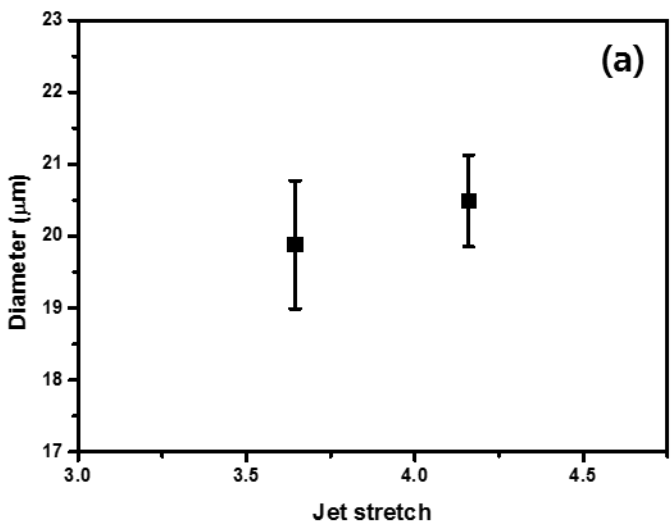

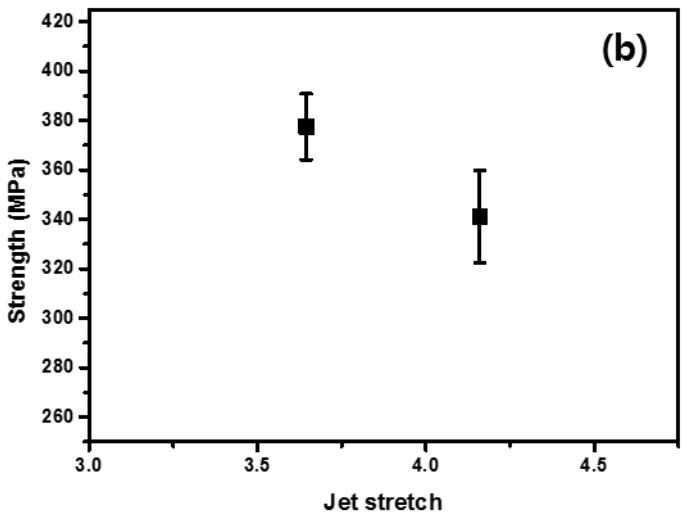
(b)
Strength (MPa)
420
400
380
360
340
320
300
280
260
3.0
3.5
4.0
4.5
Jet stretch

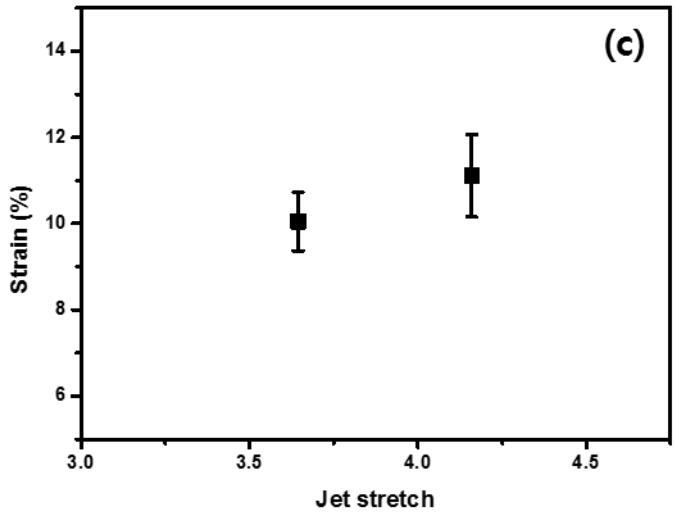
(c)
Strain (%)
14
12
10
8
6
3.0
3.5
4.0
4.5
Jet stretch

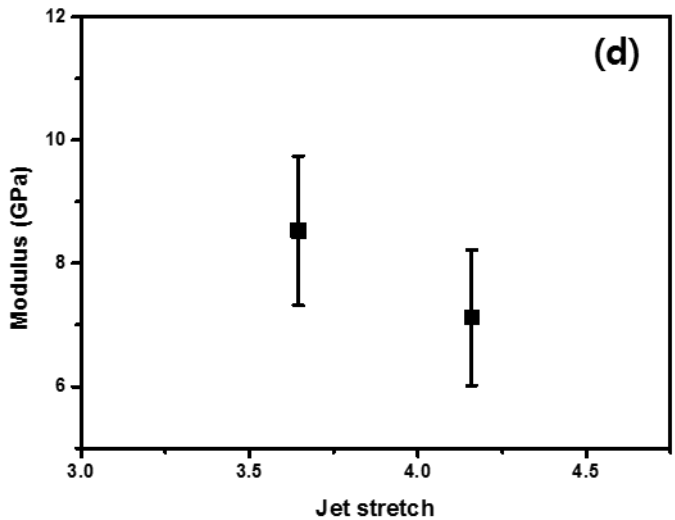

Figure 3.8. Mechanical properties of PAN fibers according to change in jet stretch (3.645 and 4.16): (a) diameter, (b) strength, (c) strain, and (d) modulus.

Jet stretch is the ratio of the velocity of dope (extrusion velocity) from the nozzle over the first take up velocity while the PAN fibers go through coagulation bath. As the jet stretch increased, the coagulation rate was increased. At high coagulation rate, the rigid skin-core structure formed and it interfere further removal of solvent inside the fibers during washing process. The core part remains as coiled PAN chains with a residual solvent. As jet stretch increased, the fiber diameter increased (Figure 3.8 (a)). This meant that at high jet stretch (4.16), the rigid skin-core structure was formed and further removal of solvent was prohibited rather than low stretch (3.645) sample. So the strength decreased and the strain increased as jet stretch increased (Figure 3.8 (b) and (c)). In case of high jet stretch (4.16), due to large diameter and

residual solvent inside the fiber, the strength decreased. Coiled PAN chains and the residual solvent (functioned as a plasticizer) induced increased strain at high jet stretch. Generally, jet stretch close to 1 is preferred in many wet-spinning researches. So PAN fibers were fabricated by using jet stretch around 1 and their mechanical properties were compared (Figure 3.9). Figure 3.8 and 3.9 were not directly compared because their rate of last roller was different (Figure 3.8: 4.65 m/min and Figure 3.9: 4.2 m/min). Unlike Figure 3.8, as jet stretch increased from 0.96 to 1.92, there were no significant change in mechanical properties of PAN fibers (the diameter was decreased at jet stretch 1.92). When considering jet stretch in Figure 3.8 (3.645 and 4.16), their mechanical properties were more dependent on the last roller rate than on jet stretch in the wet-spinning for multi filaments.

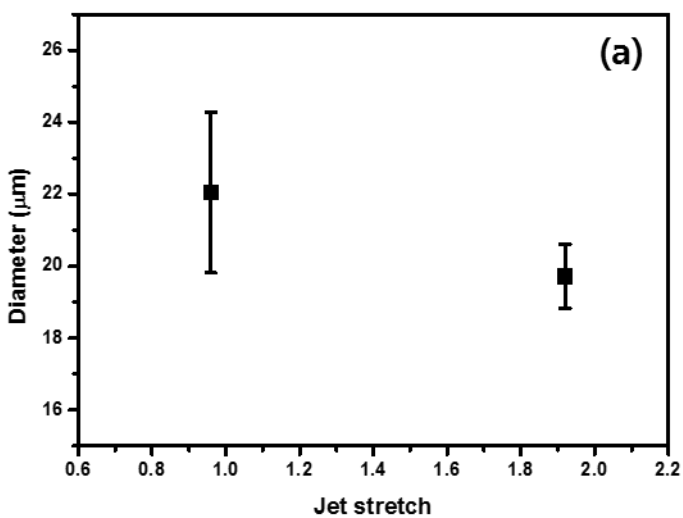

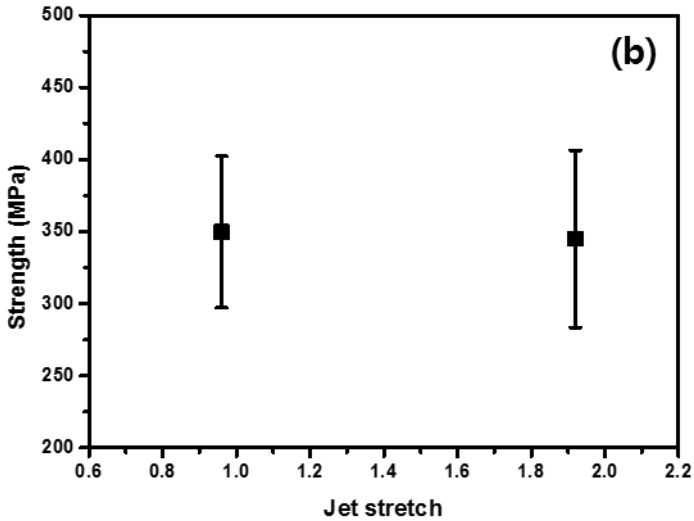
(b)
Strength (MPa)
500
450
400
350
300
250
200
0.6
0.8
1.0
1.2
1.4
1.6
1.8
2.0
2.2
Jet stretch

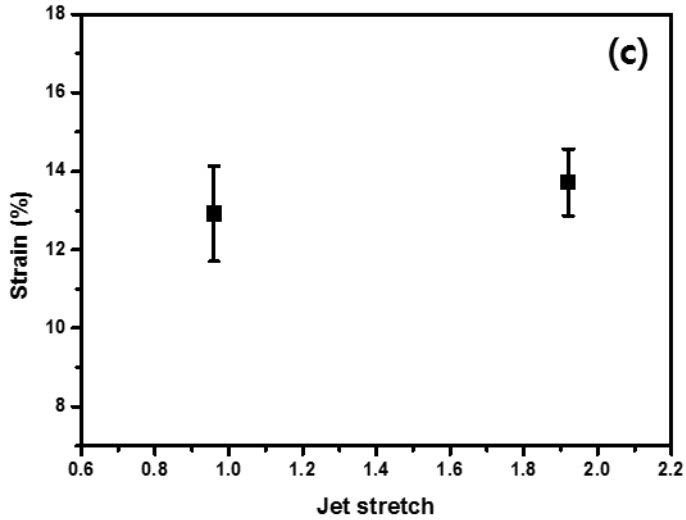
(c)
Strain (%)
18
16
14
12
10
8
0.6
0.8
1.0
1.2
1.4
1.6
1.8
2.0
2.2
Jet stretch

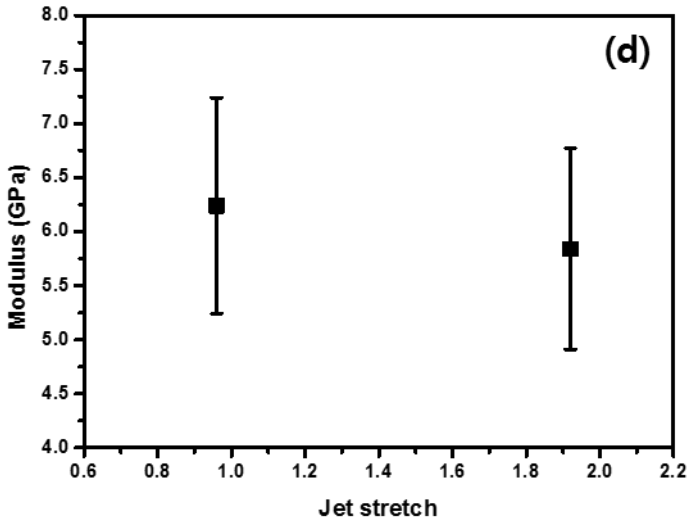

Figure 3.9. Mechanical properties of PAN fibers according to change in jet stretch (0.96 and 1.92): (a) diameter, (b) strength, (c) strain, and (d) modulus.

3.2.2.3 Coagulation composition effect

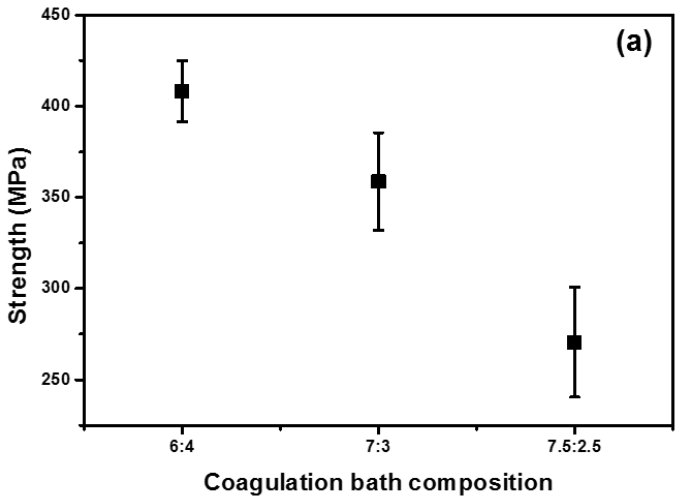

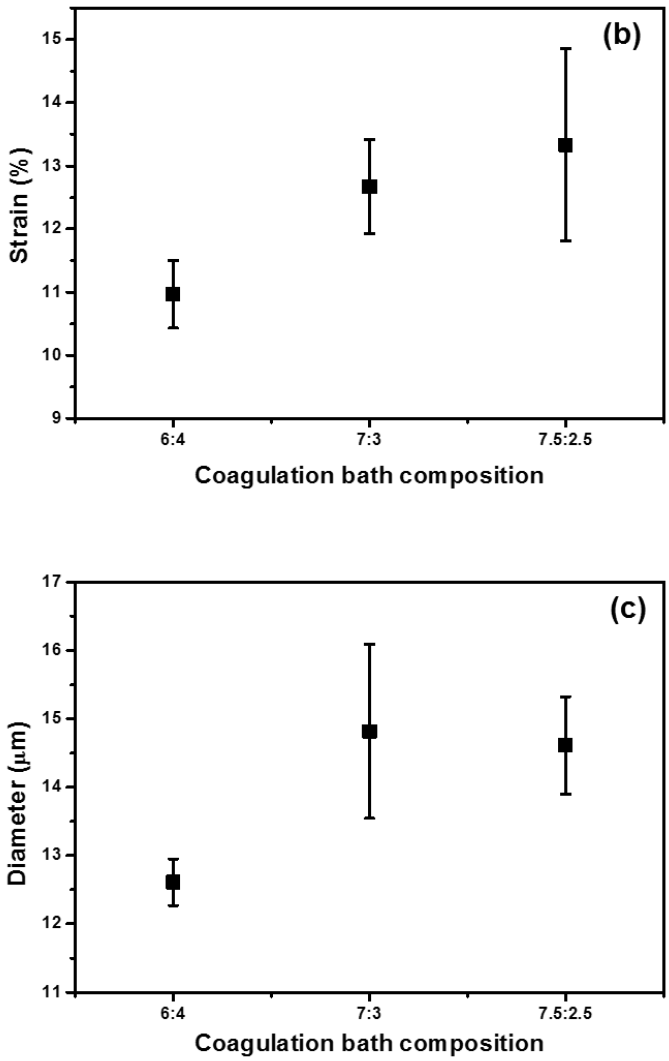

Figure 3.10. (a) Failure strength, (b) failure strain, and (c) diameter VS coagulation bath composition.

With different coagulation bath composition, fibers were fabricated without changing other parameters (solution and wet-spinning parameters) (Figure 3.10). In

high content of solvent, the exchange between solvent and non-solvent, and phase separation of polymer jet are restricted due to low gradient of diffusion. Accordingly, the fiber shrinkage effect in radial direction, resulted from phase separation by non-solvent (water), is decreased as coagulation bath composition increased. Simultaneously, PAN chains remain as coiled form (stretching effect decreases). So the diameter and strain increased (Figure 3.10 (c) and (b)). On the contrary, the failure strength gradually decreased because coiled chains (7.5 : 2.5 in coagulation bath) could not resist the external tensile force compared to the stretched chains (6:4 in coagulation bath).

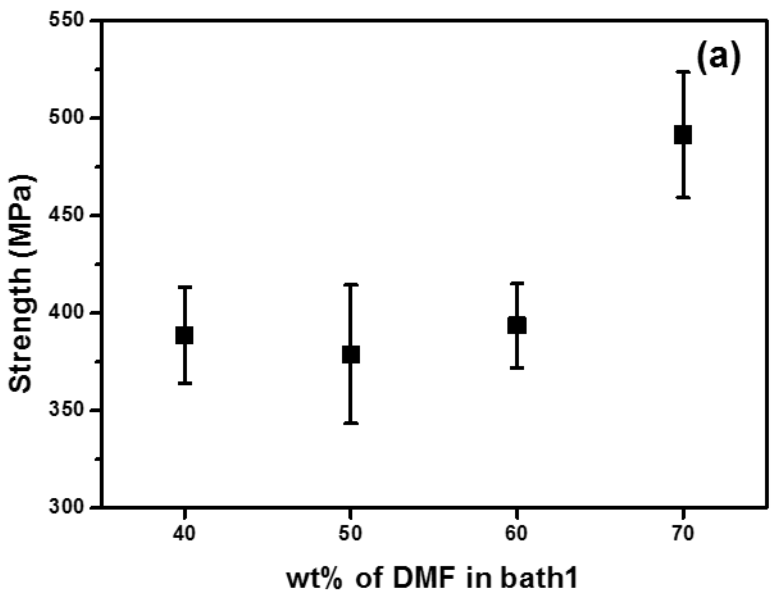

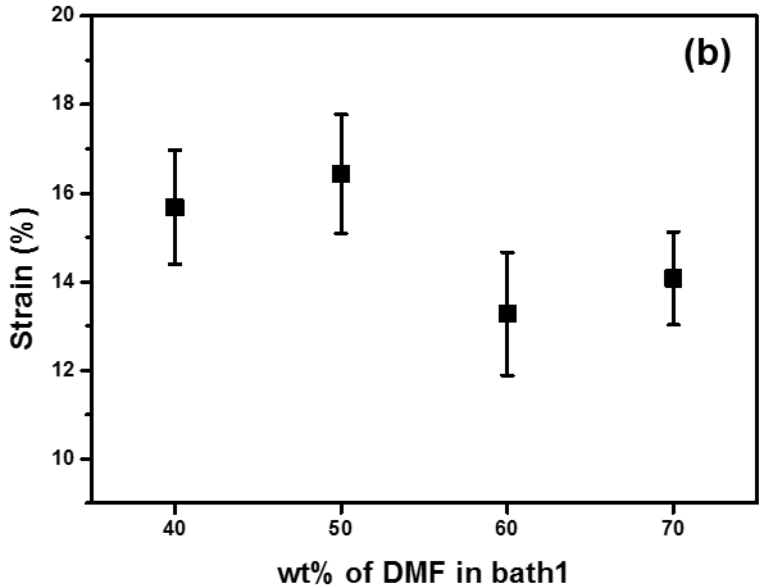

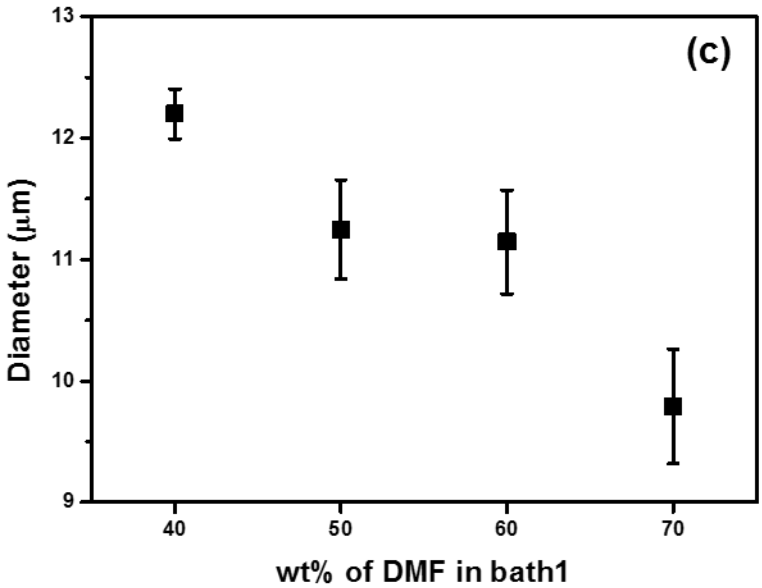

Figure 3.11. (a) Strength, (b) strain, and (c) diameter according to different

coagulation composition of the 1st bath in 3-staged bath device.

The 1st coagulation bath composition in 3-staged bath was controlled and other parameters kept constant including coagulation bath composition (7:3) (Figure 3.11). Overall tendency showed that the drawability increased as the 1st coagulation bath composition increased; the failure strength increased and the failure strain, the diameter decreased gradually. At low composition of 1st coagulation bath (40 wt%), it is expected that rigid skin-core structure was formed due to the fast phase separation by a large amount of water (or abrupt change in water concentration between coagulation bath and the 1st coagulation bath in 3-staged bath device) rather than other samples. This structure induced bad drawability at low composition of 1st coagulation bath.

3.2.2.4 Drawing ratio effect

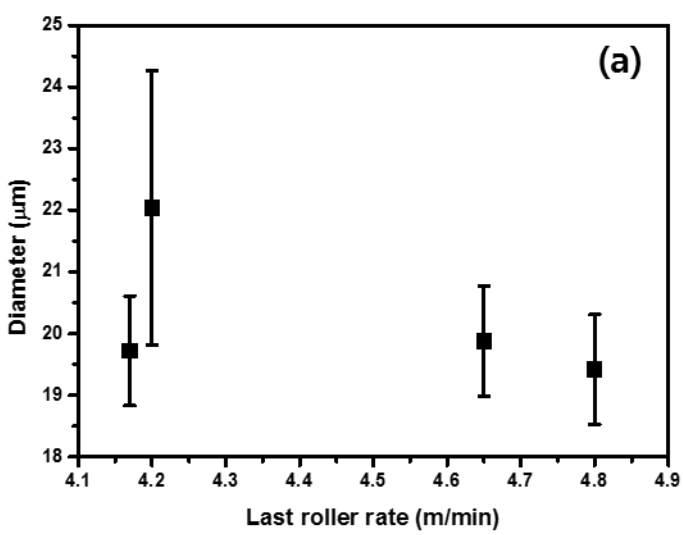

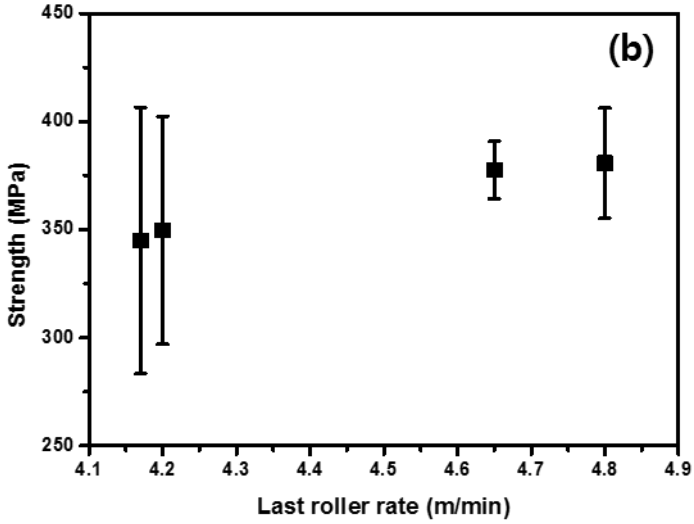
(b)
Strength (MPa)
450
400
350
300
250
4.1
4.2
4.3
4.4
4.5
4.6
4.7
4.8
4.9
Last roller rate (m/min)

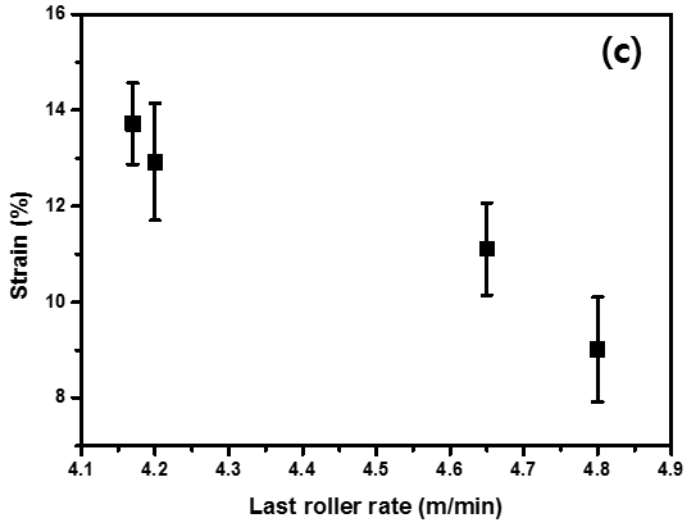
(c)
Strain (%)
16
14
12
10
8
4.1
4.2
4.3
4.4
4.5
4.6
4.7
4.8
4.9
Last roller rate (m/min)

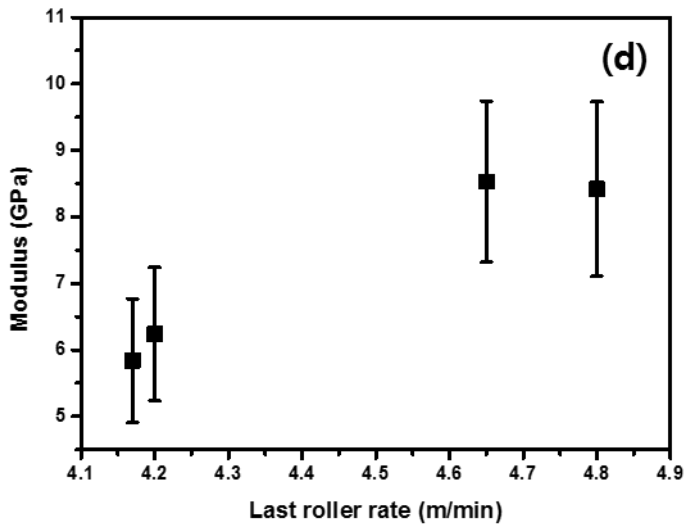

Figure 3.12. Mechanical properties of PAN fibers according to change in the last roller rate: (a) diameter, (b) strength, (c) strain, and (d) modulus.

The mechanical properties of fibers with different rate of the last roller in 3-staged bath were evaluated through tensile test. Other parameters kept constant (concentration 25 wt% and flow rate 90.83 ml/h). Generally, the diameter decreased as the last roller rate increased (Figure 3.12 (a)). Strength and strain were increased and decreased respectively as the rate of the last roller increased. The larger the rate of the last roller, the greater the change in strength and strain (Figure 3.12 (b) and (c)). Modulus also increased as the rate of the last roller increased (Figure 3.12 (d)). The polymer chains were more aligned in the direction of the fiber axis as the rate increased, and the diameter of the fibers becomes smaller, thereby increasing the overall mechanical performance.

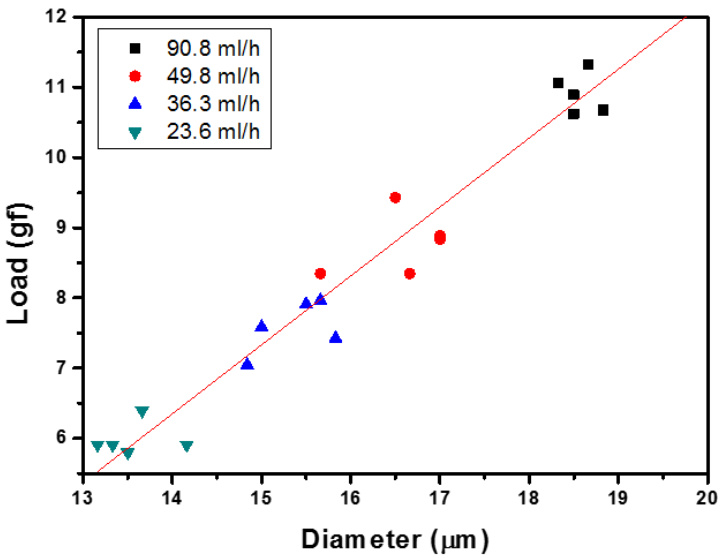

Figure 3.13. Relationship between flow rate and diameter for 20 wt% of PAN solution.

Like Figure 3.1, similar experiments were conducted on 20 wt% of PAN solution. As mentioned above (see section 3.1.2), lowering PAN concentration was necessary to avoid difficulties in imperfect preparation of PAN solution and additional process. The relationship between flow rate and the last drawing rate was investigated (Figure 3.13). All fibers were drawn just before breakage of fibers. Except flow rate and stretch ratio, other wet-spinning parameters keep constant (coagulation composition (6:4 in wt%) and bath temperature (room temperature for coagulation bath and 40, 60, 85 °C for 1st, 2nd, 3rd bath in 3-staged bath respectively). As flow rate decreased (90.8 → 23.6 ml/h), diameter (19 → 13 μm), the last roller rate (9.5 → 6.8 m/min), and failure load also decreased. High flow rate induced large polymer jet from the nozzle and then relatively thick fiber have difficulty in exchange between solvent

and non-sovlent. Therefore, as the fibers went through the process, the thick fibers have relatively thick shell, which leads to bad drawability and larger diameter even with faster stretch rate. Consequently, failure load and fiber diameter have linear relationship so failure strength is almost constant (400 Mpa) for all samples. With optimization of various parameters in wet-spinning, PAN fibers fabricated from 20 wt% showed almost similar strength with PAN fibers fabricated from 25 wt% (Figure 3.6). Originally, diameter and failure strength have quadratic relation but for fibers with diameters greater than 10 μm, a linear relationship between diameter and failure strength was observed.

3.3. Summary

Before current-assisted wet-spinning process, ordinary wet-spinning process was conducted in both wet-spinning for single filament and for multi filaments processes. Basic wet-spinning parameters were decided by stacking various data. According to the change in concentration of PAN solution and flow rate, jet stretch, drawing rate was determined. By performing the wet-spinning for single filament process, the need for the wet-spinning for multi filaments process has been raised and it was set. Based on experiments data, current-assisted wet-pinning was conducted and it would be introduced in next section.

4. Current-assisted wet-spinning: Basic setup

In this section, current-assisted wet-spinning was introduced both in wet-spinning for single filament and wet-spinning for multi filaments processes. The electric potential was applied to the syringe and other processes were same with the conventional wet-spinning processes. The PAN fibers fabricated through general wet-spinning and the PAN fibers fabricated through current-assisted wet-spinning were compared. There have been numerous trials and errors before the current-assisted wet-spinning actually worked. Detailed trials and errors were introduced here.

4.1. Current-assisted wet-spinning for single filament

4.1.1 Experimental (electric current introduction)

(a)

(b)

Figure 4.1. Self-designed (a) initial metal syringe for applying electric potential and (b) polymer syringe for applying electric potential.

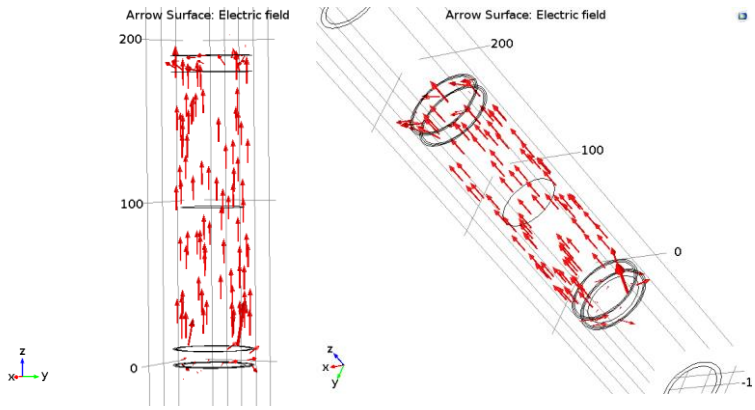

Figure 4.2. COMSOL simulation of Electric field distribution on the metal syringe during applying electric potential.

The current-assisted wet-spinning was done by simply applying potential to the syringe in the wet-spinning for single filament process (see section 3.1.1). Initially, the electric potential was directly applied to metal syringe (Figure 4.1 (a)) by connecting negative positive sockets to metal syringe plunger part and nozzle part respectively *via* copper tape. However, the applied charge to the conducting materials exists only on the surface of the conducting materials by Gauss's law. In other words, regardless of external electric field strength, there is no difference in charge distribution inside the conducting materials (no electric field inside the syringe). So the external electric field cannot penetrate metal syringe barrel and cannot affect PAN solution at all. Figure 4.2 is Comsol simulation of electric field distribution on the metal syringe during applying electric potential; the electric field existed only on the metal syringe barrel surface. Thus, syringe barrel was made of polypropylene (Figure 4.1 (b)) instead of metal. Furthermore, in case of metal syringe the electric current would flow only through metal syringe (lower resistance part). The polypropylene syringe was used in current-assisted wet-spinning. The

electric potential was applied *via* electrometer (Keithley 6517B) while current-assisted wet-spinning was proceeded. Except syringe part, other current-assisted wet-spinning process was same with the conventional wet-spinning process (see section 3.1.1). The concentration of PAN solution was varied from 25 wt% to 32 wt%.

4.1.2 Results and discussion

The PAN fibers fabricated through general wet-spinning and the PAN fibers fabricated through current-assisted wet-spinning were abbreviated as GPANf and EPANf respectively. The number just following the abbreviation stands for the concentration from which the PAN fiber was made. The current-assisted wet-spinning was conducted with various concentration of PAN solution (25 – 32 wt%).

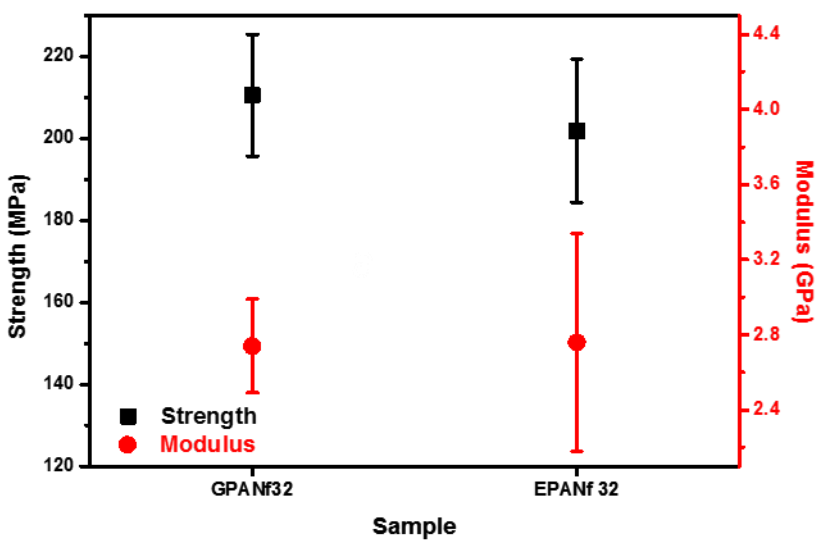

Figure 4.3. Strength and modulus comparison between GPANf32 and EPANf32 fabricated from 32 wt% PAN solution.

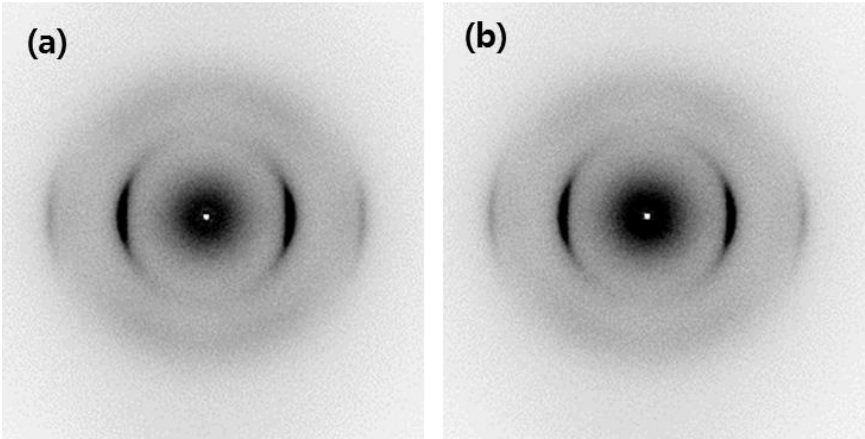

Figure 4.4. 2D-WAXD image of (a) GPANf32 and (b) EPANf32.

Initially, high concentrated PAN solution (32 wt%) was spun *via* general wet-spinning and current-assisted wet-spinning (GPANf32 and EPANf32). In current-assisted wet-spinning process, the applied electric potential was 30 V. The average strength and modulus of GPANf32 and EPANf32 were almost same (Figure 4.3). The failure strain was not included because the delamination of adhesive during tensile test occurred (see Figure 3.3 and 3.4 in section 3.1.2). The diameter of EPANf32 decreased by 3 μm compared to GPANf32 (GPANf32: 54.46 μm and EPANf32: 52.39 μm). The preferred orientation of GPANf32 and EPANf32 was calculated from extracted azimuthal scan from Figure 4.4. The preferred orientations were almost same (79.2% and 79% for GPANf32 and EPANf32 respectively).

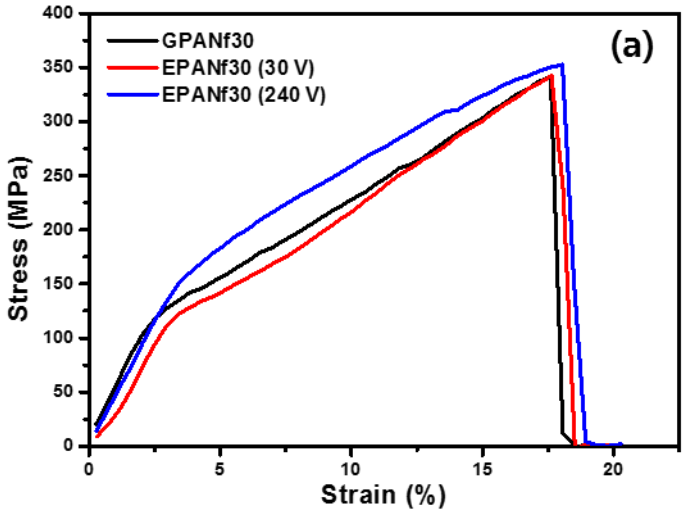
(a)
GPANf30
EPANf30 (30 V)
EPANf30 (240 V)
Stress (MPa)
Strain (%)
0
50
100
150
200
250
300
350
400
0
5
10
15
20

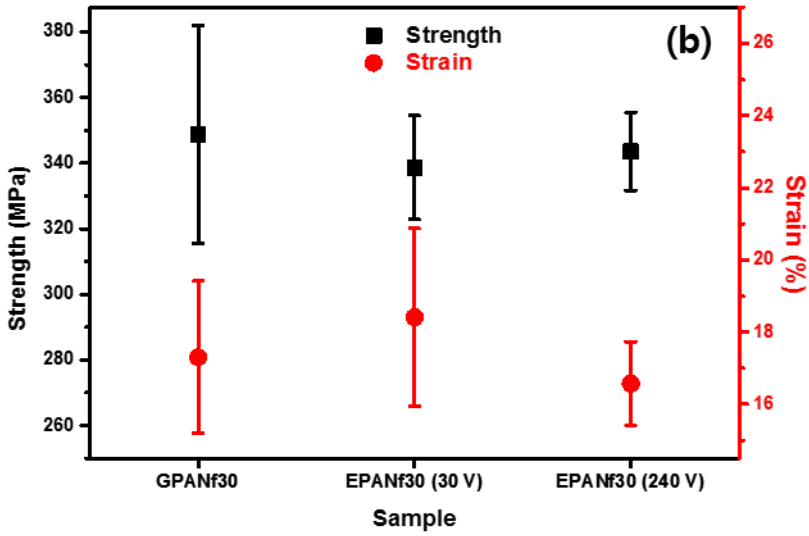
(b)
Strength
Strain
Strength (MPa)
Strain (%)
Sample
GPANf30
EPANf30 (30 V)
EPANf30 (240 V)
260
280
300
320
340
360
380
16
18
20
22
24
26

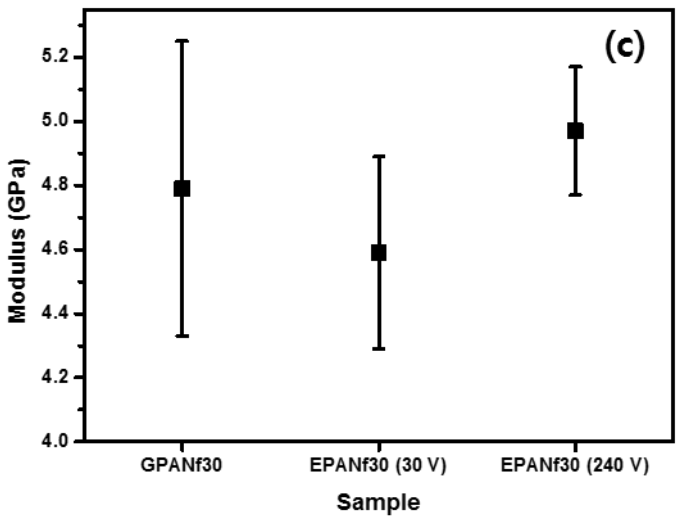

Figure 4.5. (a) S-S curve, (b) average strength and strain, (c) average modulus of GPANf30, EPANf30 (30 V), and EPANf30 (240 V).

There were no difference between general wet-spinning process and current-assisted wet-spinning (Figure 4.3 and 4.4) so the concentration decreased (30 wt%) and the electric potential increased from 30 V to 240 V. Representative S-S curve of tensile-tested sample of GPANf30, EPANf30 (30 V), and EPANf30 (240 V) was shown in Figure 4.5 (a). There was no difference in the mechanical properties of samples even with applying high electric potential (240 V). Diameter of each sample was 37.66, 41.79, and 40.06 μm for GPANf30, EPANf30 (30 V), and EPANf30 (240 V). Unlike samples in Figure 4.3, the diameter of EPANf30 increased a little bit compared to GPANf30.

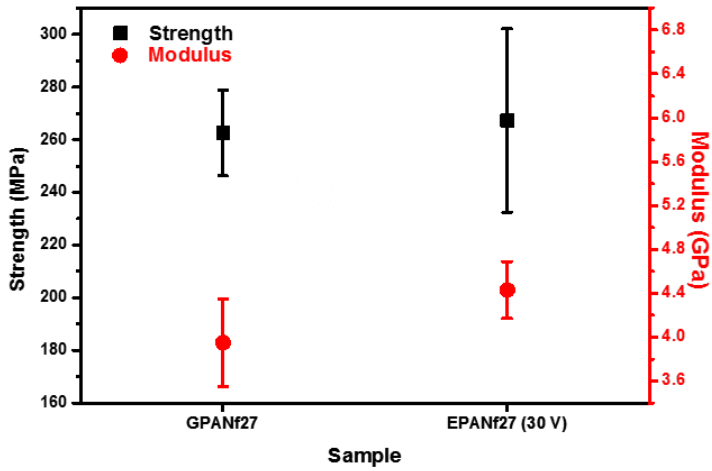

Figure 4.6. Average strength and modulus comparison between GPANf27 and EPANf27 (30 V)

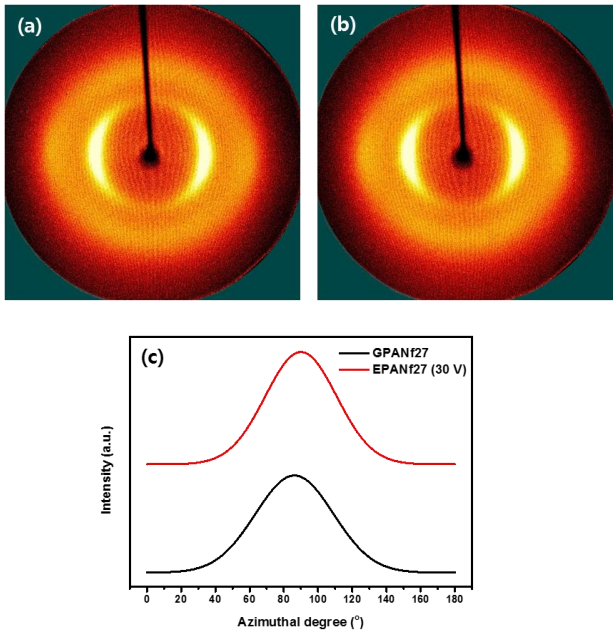

Figure 4.7. 2D-WAXD images of (a) GPANf27 and (b) EPNf27 (30 V). (c) azimuthal scan extracted from 2D-WAXD images.

27 wt% PAN solution was spun with both processes and their mechanical properties were compared (Figure 4.6). The applied electric potential was 30 V for fabricating EPANf27. The strain of GPANf27 and EPANf27 was excluded for same reason (the delamination of adhesive in the sample resulted in longer strain). Strength of each sample was almost same but the modulus of EPNAF27 increased slightly rather than that of GPANf27. Figure 4.7 (a) and (b) were 2D-WAXD images of GPANf27 and EPANf27. Figure 4.7 (c) was extracted azimuthal scan from 2D-WAXD images for each sample. The preferred orientation was 74.03% and 76.84% for GPANf27 and EPANf27 respectively. Due to increased orientation of EPANf27, EPANf27 showed slightly higher modulus (Figure 4.6). Actually higher orientation was one distinct feature shown in EPANf so detailed would be explained in page 121 in section 5.2.3.2. The diameter of each sample was 41.09 and 41.45 μm.

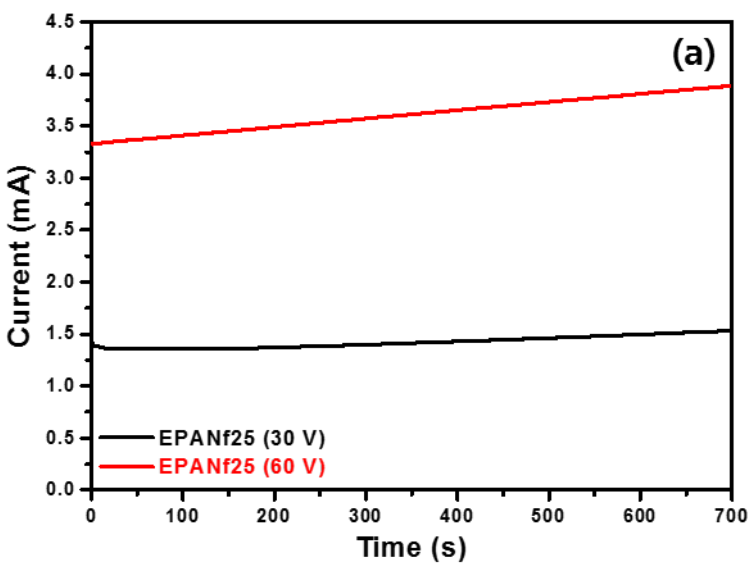

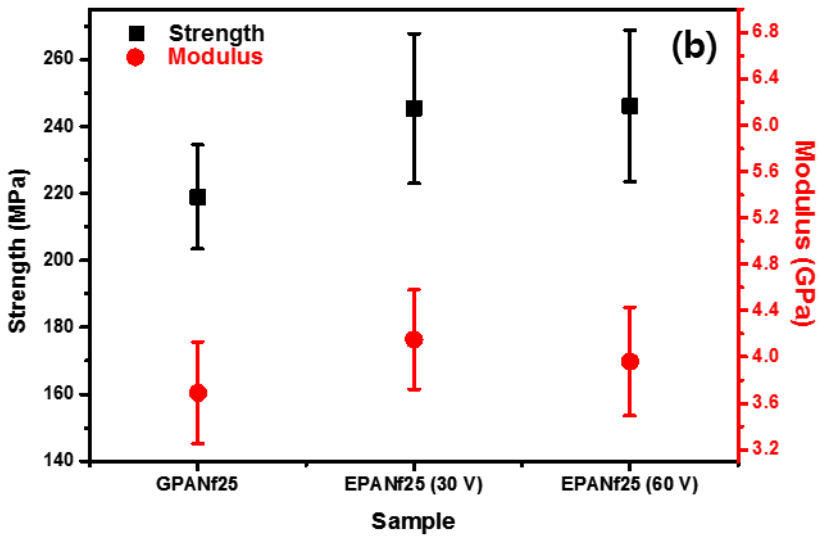

Figure 4.8. (a) Electric current during current-assisted wet-spinning. (b)Average strength and modulus comparison between GPANf25, EPANf25 (30 V), and EPANf25 (60 V).

25 wt% PAN solution was also spun with same method like above explanation. Figure 4.8 (a) showed the electric current during current-assisted wet spinning. As the applied electric potential increased, the electric current value also increased. Moreover, as the process progressed further, the current value increased. As the PAN solution was consumed, the height of the PAN solution was lowered. As a result, the electric field increased even at the same potential and finally, the electric current increased by more mass transport of PAN chains (electrophoresis). Note that much higher current (~ mA) in current-assisted wet-spinning for single filament than the current (~ μA) in current-assisted wet-spinning for multi filaments was due to much larger nozzle area contacted with PAN solution in current-assisted wet-spinning for

single filament (current-assisted wet-spinning for single filament: 4 cm^2 and current-assisted wet-spinning for multi filaments: 1.7 cm^2). However, the mechanical properties of GPANf25, EPANf25 (30 V), and EPANf (60 V) were almost same. The diameter of each sample was 48.25, 46.4, and 46.15 μm respectively. The EPANf diameter decreased by about 2 μm.

4.2. Current-assisted wet-spinning for multi filaments

4.2.1 Experimental

Figure 4.9. Self-designed syringe for current-assisted wet-spinning for multi filaments.

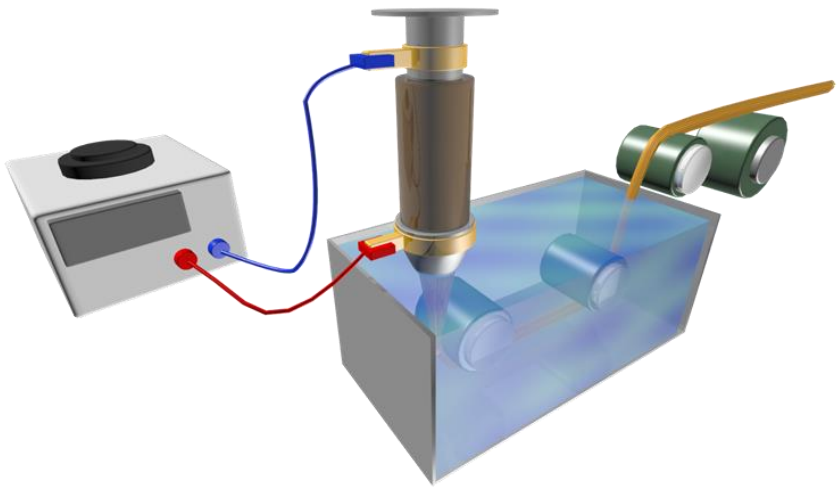

Figure 4.10. Schematic diagram of front part in current-assisted wet-spinning process.

Like current-assisted wet-spinning for single filament, the syringe barrel and other parts for connecting nozzle were made of polypropylene (Figure 4.9). The screw in each polypropylene part was covered by Teflon tape to prevent the leakage of PAN solution (see Figure 4.9).

Figure 4.10 shows the schematic diagram of syringe and coagulation part of current-assisted wet-spinning for multi filaments. Before polymer jet enters coagulation bath, electric potential is applied to the syringe. The electric potential was applied *via* electrometer (Keithley 6517B) while current-assisted wet-spinning is proceeded. We also called the PAN fibers fabricated *via* general wet-spinning as MGPANf and the PAN fibers fabricated *via* current-assisted wet-spinnning as MEPANf.

Unlike section 3.2.1, the most of parameters like flow rate, drawing ratio, and drawing ratio were settled down. Flow rate was 23.6 ml/h and rate of four rollers was set as 0.47, 0.9, 1.4, and 4.1 m/min. The concentration of PAN solution used for the

process was only 25 wt% and 20 wt% (the procedure of PAN solution preparation was not optimized in this part yet). The method to apply electric potential was same (see section 4.1.1) and other parts in current-assisted wet-spinning for multi filaments were also same (see section 3.2.1)

4.2.2 Results and discussion

4.2.2.1 Solvent diffusion control by coagulation composition

Like PAN fibers in section 4.1.2, the fibers were abbreviated as MGPANf and MEPANf (M came from multi-orificed nozzle). The number just following the abbreviation meant concentration of PAN solution and the number just after '-' was the repeated number of experiments.

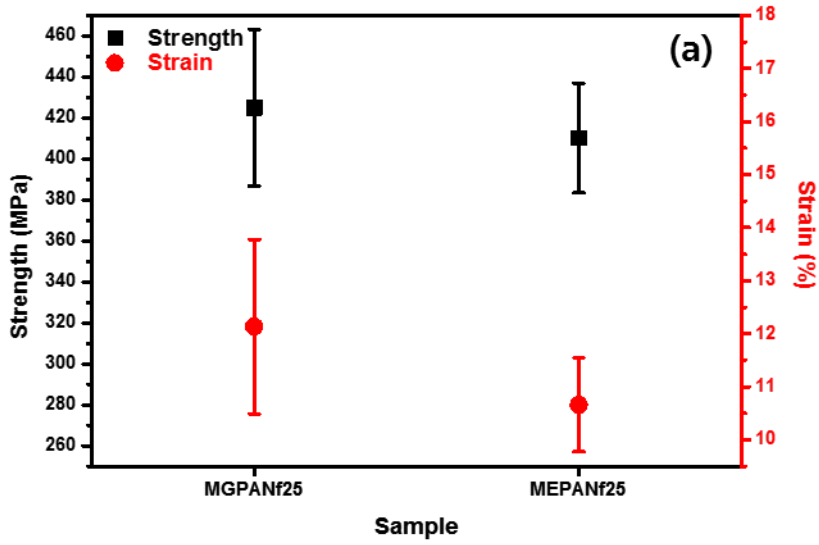

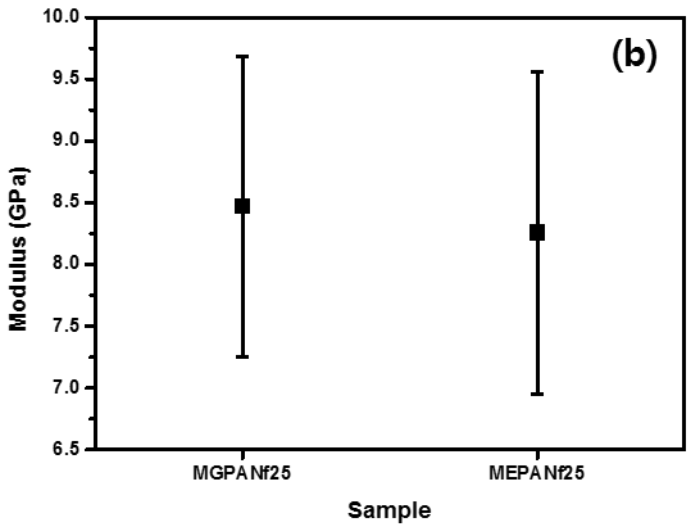

Figure 4.11. (a) Average strength, strain, and (b) modulus comparison between MGPANf25 and MEPANf25.

25 wt% PAN solution was spun *via* both wet-spinning and current-assisted wet-spinning for multi filaments (MGPANf25 and MEPANf25). In Figure 4.11 (a), black point with black error bar was strength and red point with red error bar was strain of each sample (this was same for other Figures until Figure 4.14). Strength and modulus of each sample was not changed much (Figure 4.11). However, failure strain of MEPANf25 decreased a little bit. The diameter of each fibers was 13.79 and 14.30 μm respectively.

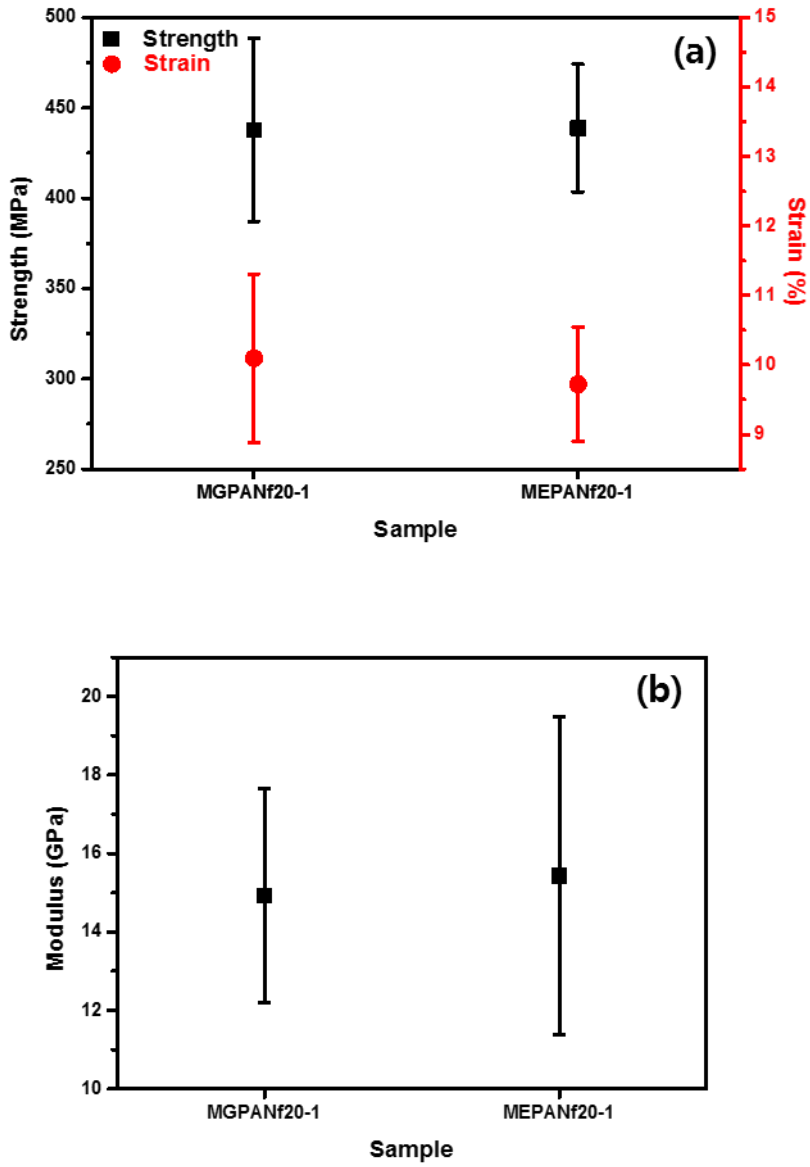

Figure 4.12. (a) Average strength, strain, and (b) modulus comparison between MGPANf20-1 and MEPANf20-1.

20 wt% PAN solution also spun with the both processes (MGPANf20-1 and

MEPANf20-1). Mechanical properties of samples were shown in Figure 4.12. Like samples in Figure 4.11, there were no big difference in their mechanical properties. Their diameter was 10.53 and 10.68 μm respectively.

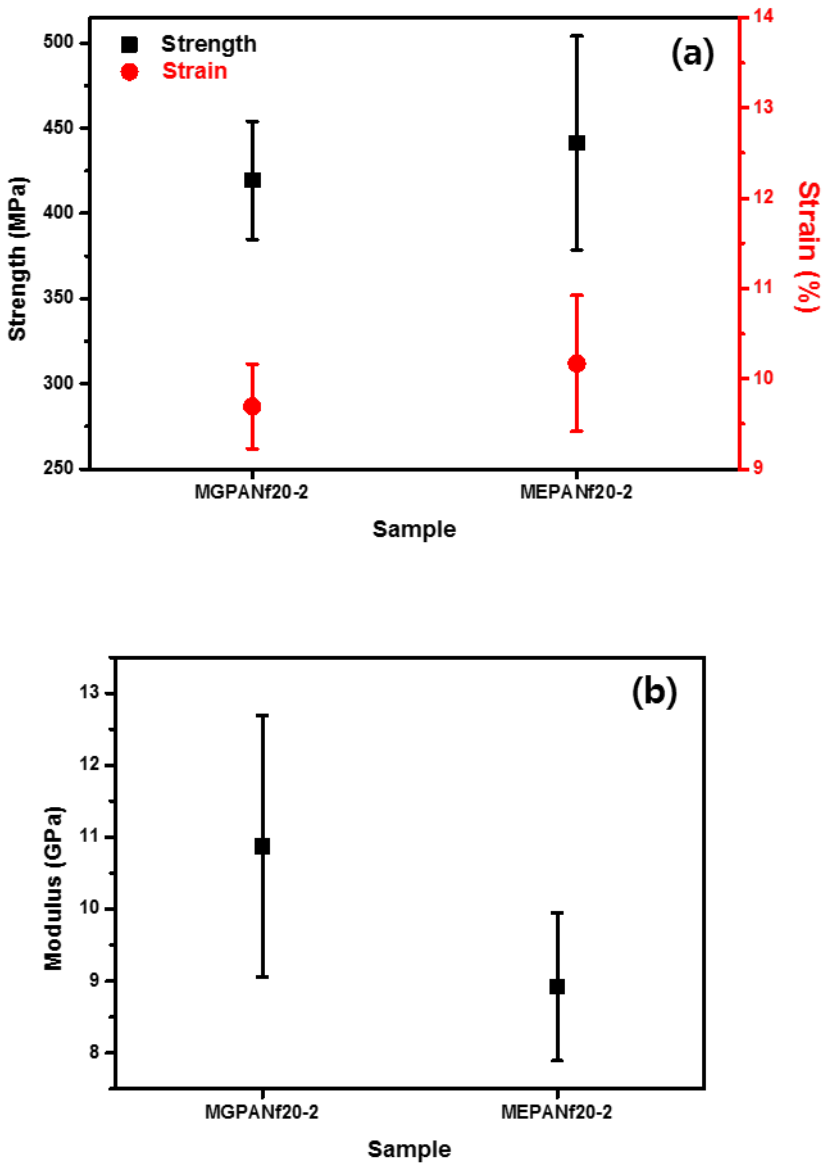

Figure 4.13. (a) Average strength, strain, and (b) modulus comparison between

MGPANf20-2 and MEPANf20-2.

The 20wt% PAN solution was secondly spun like samples in Figure 4.12. This time, the strength and strain of EPANf20-2 were simultaneously increased (Figure 4.13 (a)) unlike other sample. However, the modulus of EPANf20-1 was decreased (Figure 4.13 (b)). The diameter for GPANf20-2 and EPANf20-2 was 12.49 and 14.66 μm respectively.

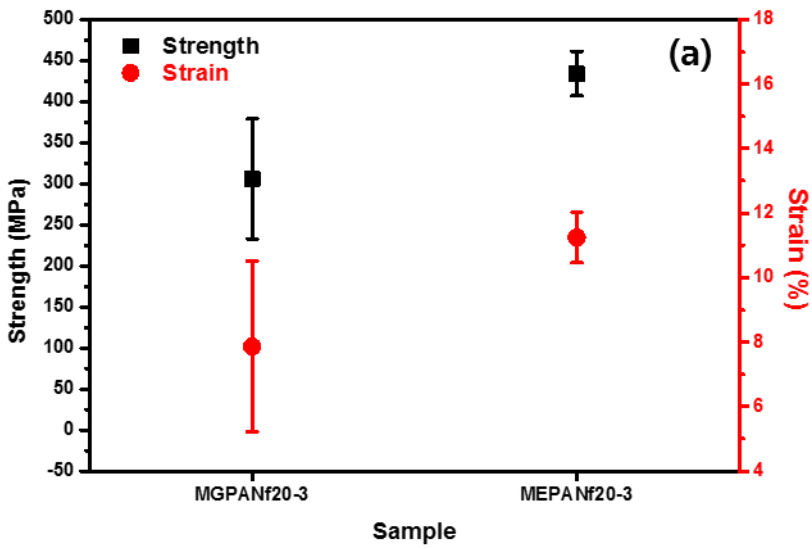

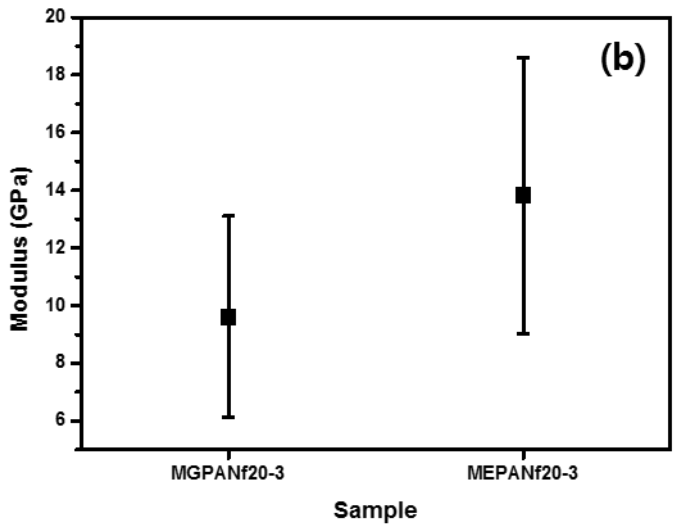

Figure 4.14. (a) Average strength, strain, and (b) modulus comparison between MGPANf20-3 and MEPANf20-3.

The spinning of 20 wt% PAN solution was tried again (MGPANf20-3 and MEPANf20-3). This time, the rate of the last roller was increased from 4.1 to 4.6 m/min. At this rate (4.6 m/min), it was expected that defibrillation occurred in MGPANf20-3 because strength and strain of MGPANf20-3 much lower than those of other MGPANf20 (Figure 4.12 and 4.13) as well as than those of MEPANf20-3. Furthermore, error bar of MGPANf20 strength and MGPANf20 strain (Figure 4.14 (a)) was extremely higher than any other samples. It meant that defibrillation partially occurred due to high rate. However, in case of MEPANf20-3, strength and strain were more increased than other MPANf20 (Figure 4.12 and 4.13) samples. The diameter of MGPANf20-3 and MEPANf20-3 was 10.92 and 11.12 μm respectively. From this result, it was believed that there was a definite effect of

current-assisted process.

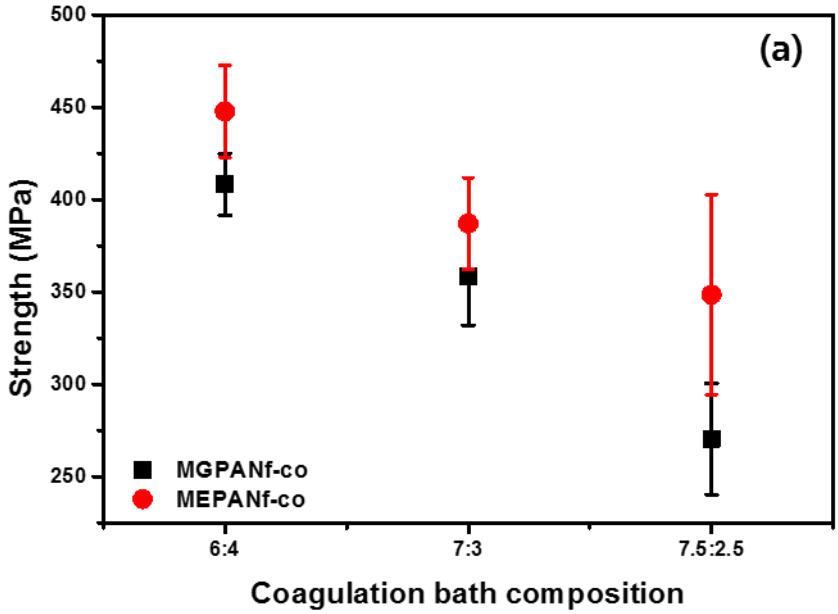

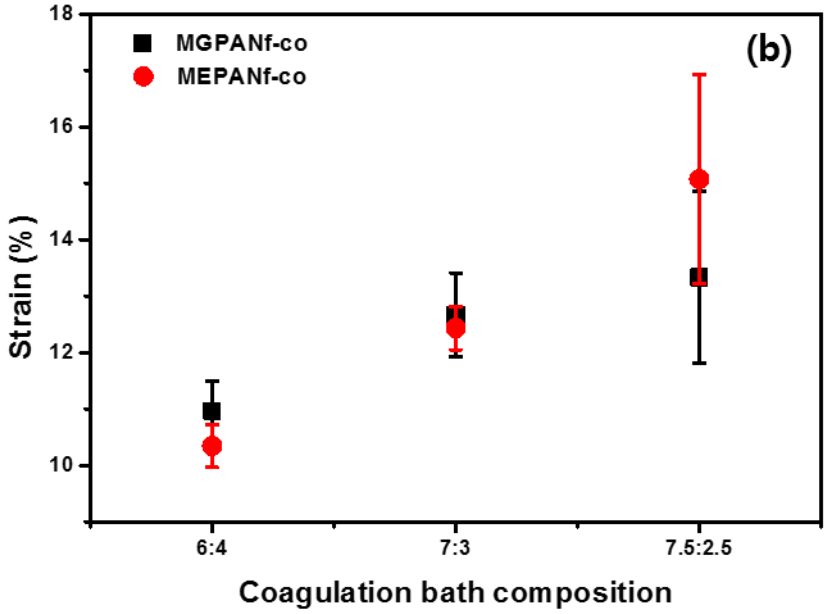

Figure 4.15. (a) Strength and (b) strain comparison between GPANf-co and EPANf-co fabricated from different coagulation bath.

Figure 4.13 (a) (MGPANf20-2 and MEPANf20-2) showed a little bit difference between two samples (strength and strain of MEPANf20-2 was higher than those of MGPANf20-2). And in Figure 4.14, MEPANf20-3 sample definitely showed superior mechanical properties than MGPANf20-3 sample. When these experiments were conducted, the experiments were done continuously without changing the coagulation bath (originally 6:4 in weight fraction of solvent and non-solvent). So it was thought that solvent portion in coagulation bath increased because the solvent in PAN polymer jets diffused into coagulation bath. In this respect, experiments of PAN fibers fabricated from different coagulation bath composition were conducted through both general wet-spinning and current-assisted wet-spinning. The black point with black error bar was strength and strain of MGPANf-co while the red point with red error bar was strength and strain of MEPANf-co (Figure 4.15); 'co' just behind the hyphen meant 'coagulation bath'. At low solvent in coagulation bath (6:4), the mechanical properties were almost similar. As the solvent in coagulation bath increased the gap between MGPANf-co and MEPANf-co became larger. In Figure 4.15 (a), the gap gradually increased from 8, 9, and 28% respectively. While, in Figure 4.15 (b), the gap of strain also gradually increased from -5, -1, and 13%. However, although the gap increased, the strength or strain gradually decreased in each MGPANf-co and MEPANf-co respectively. The effect of current-assisted process is to absorb more non-solvent by forming ions (detailed would be explained in section 5 and 6). So at the low solvent in coagulation bath (6:4), there was no big

difference in mechanical properties between GPANf and EPANf because already enough non-solvent existed in coagulation bath. Furthermore, the effect of current-assisted process led faster coagulation rate, which formed more the rigid skin-core. Due to the bad drawability resulted from rigid skin-core in EPANf, generally, EPANf showed higher diameter than GPANf. In this aspect, at high solvent in coagulation bath, the effect of current-assisted process was obvious. Note that samples in Figure 4.15 were different with the samples which would be introduced in section 5.2.

4.3. Summary

Basic current-assisted wet-spinning was conducted in both wet-spinning for single filament process and wet-spinning for multi filaments process. Numerous trials and errors have been made and these samples did not show any effect of current-assisted process. The clue for the effect of current-assisted wet-spinning was accidently found; countless experiments increased the solvent portion in coagulation bath and the EPANf fabricated in this coagulation bath showed superior mechanical properties than GPANf. More precise experiments with the condition would be introduced in section 5 and 6.

5. Defect and mechanical properties of PAN filaments

Based on stacked information from section 4, the current assisted wet-spinning was performed in the coagulation bath containing high solvent content. GPANf and EPANf were fabricated through both wet-spinning for single filament process and wet-spinning for multi filaments process and they were compared. Various characterization methods were introduced to briefly explain the mechanism of current-assisted process.

5.1. The effect of coagulation composition

5.1.1 Experimental

PAN solution was prepared at 25 wt% concentration. Flow rate was 19 ml/h and the rate of the first and second (final) roller was 7.85 and 39.25 m/min, respectively. Coagulation bath composition was 7:3 wt% of solvent and non-solvent mixture. Other detailed was already explained in section 3.1.1 and 4.1.1. The applied potential was 60 V in current-assisted wet-spinning.

5.1.2 Increased mechanical properties of single PAN filament

25 wt% PAN solution was spun *via* both wet-spinning and current-assisted wet-spinning for single filament. The PAN fibers fabricated from both processes were abbreviated as GPANf and EPANf. During current-assisted wet-spinning for single filament, the electric current was constant as about 2 mA.

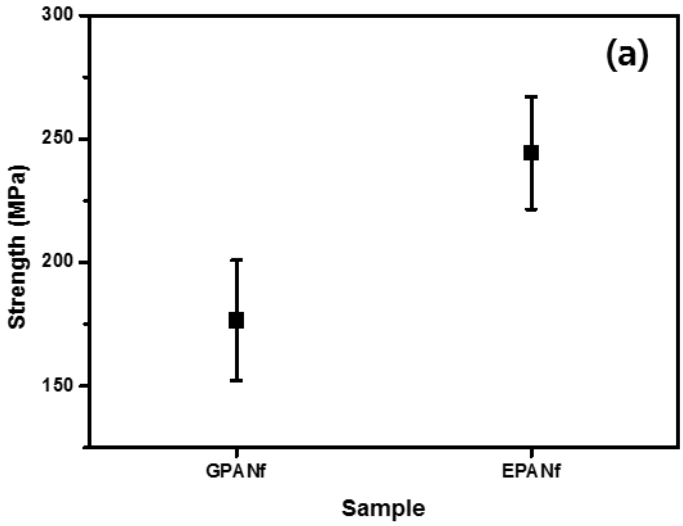
(a)
Strength (MPa)
300
250
200
150
GPANf
EPANf
Sample

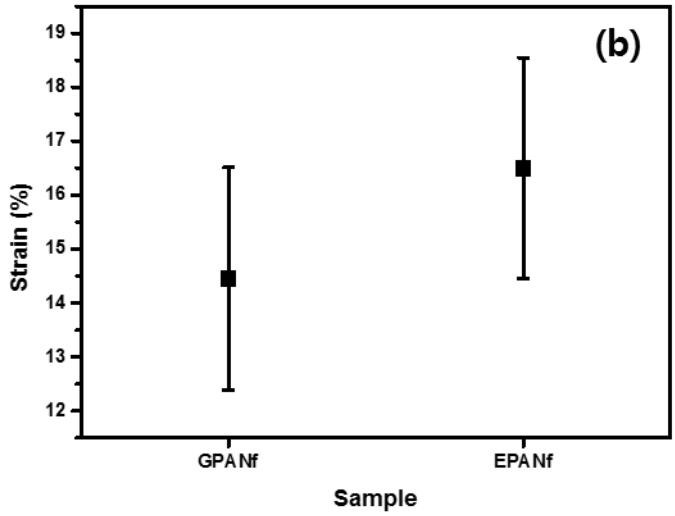
(b)
Strain (%)
19
18
17
16
15
14
13
12
GPANf
EPANf
Sample

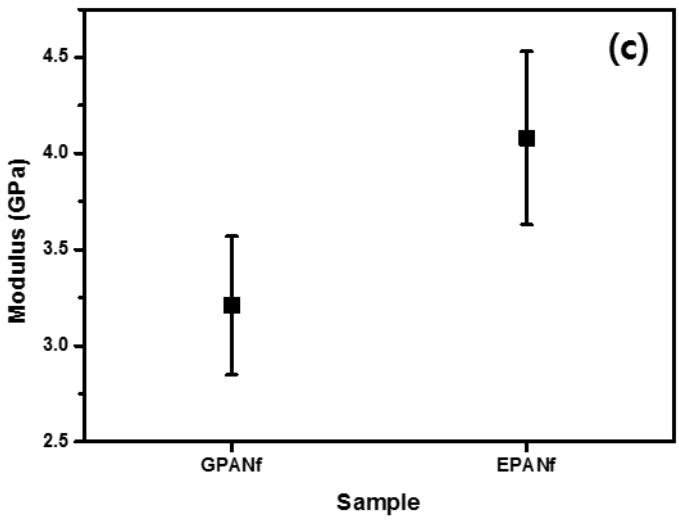

Figure 5.1. (a) Average strength, (b) strain, and (c) modulus comparison between GPANf and EPANf.

In Figure 5.1, mechanical properties (strength, strain, and modulus) of EPANf were higher than those of GPANf by 38, 14, and 27% respectively. These gaps between GPANf and EPANf were not shown in previous samples in section 4.1. The diameter of GPANf and EPANf was 48.56 and 48.73 μm respectively, which were almost similar. This is a notable feature because previously almost all EPANf diameters were much larger than the GPANf diameter (1 – 2 μm difference).

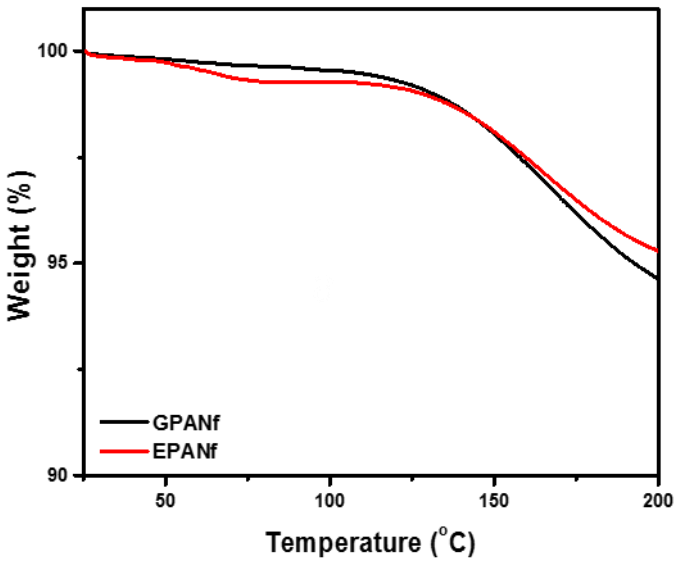

Figure 5.2. TGA plot of GPANf and EPANf.

TGA was performed on GPANf and EPANf for evaluating solvent and non-solvent contents in the fibers (Figure 5.2). Before TGA measurement, all samples were dried at least for 2 days at room temperature. Around 50 °C, the weight of EPANf more decreased than that of GPANf. This attributed to more water content in EPANf sample and the gap was about 0.4%. Just before 150 °C (boiling point of DMF is 152 °C), the slope of GPANf and EPANf was changed and the tendency was reversed. In other words, GPANf included more solvent (DMF). In this aspect, it could be said that applying electric potential helped exchange of solvent and non-solvent. Unlike Figure 5.10 (b), GPANf and EPANf in Figure 5.2 contained more DMF because DMF extraction from the fibers were interfered by their large diameter.

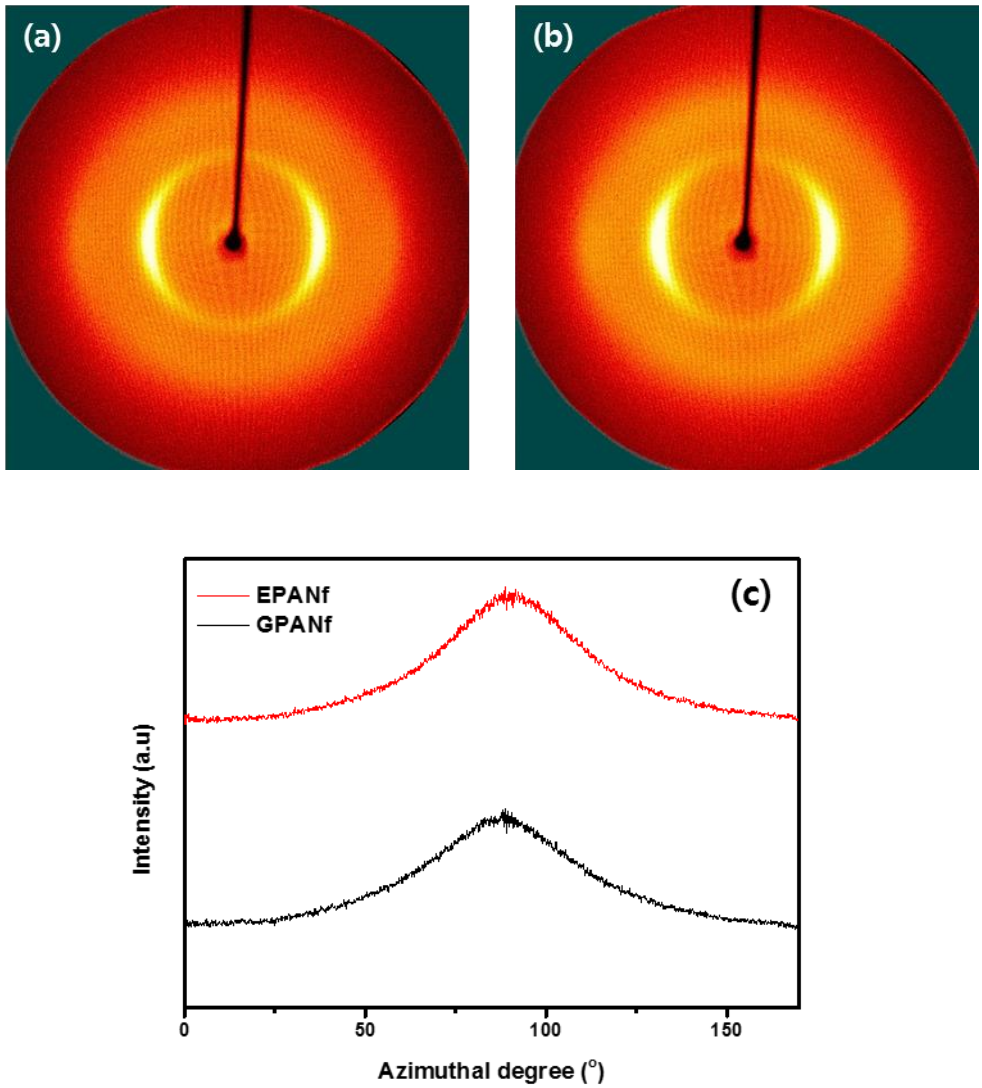

Figure 5.3. 2D-WAXD images of (a) GPANf and (b) EPANf. (c) Azimuthal scan extracted from 2D-WAXD images.

For calculating crystallinity and preferred orientation (P.O), WAXD (Figure 5.3) was performed on both GPANf and EPANf. The crystallinity of GPANf and EPANf was 26.59 and 25.09% while the P.O of GPANf and EPANf was 74.42 and 76.40%. The

EPANf crystallinity decreased a little bit and the EPANf P.O increased than GPANf. The reason for increase in EPANf P.O was described in page 121 in section 5.2.3.2.

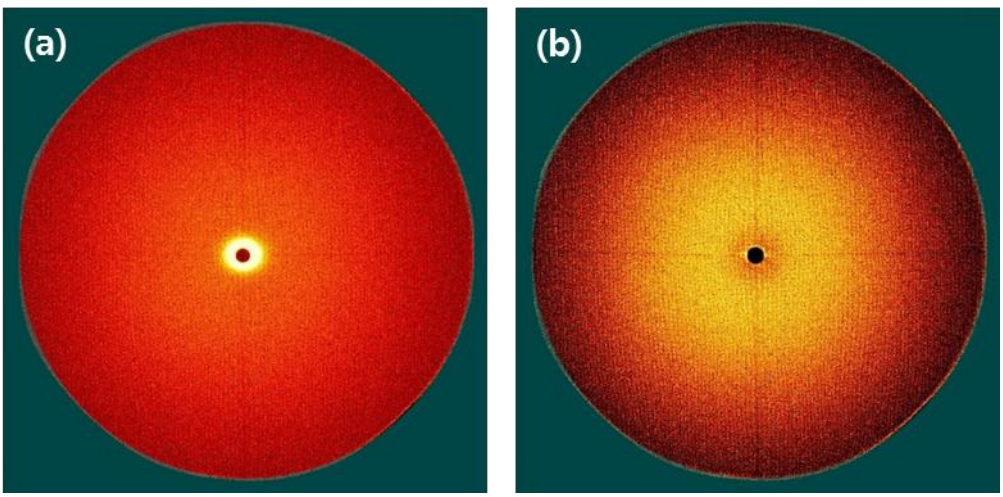

Figure 5.4. 2D-SAXS images of (a) GPANf and (b) EPANf.

SAXS was performed on GPANf and EPANf for evaluating void information. The scattering intensity in 2D-SAXS images come from the difference in electron density between PAN matrix and voids. As shown in Figure 5.4, total scattering intensity in EPANf (Figure 5.4 (b)) was much lowered than that in GPANf (Figure 5.4 (a)). This indirectly implied that size of voids in EPANf decreased or number of voids in EPANf sample are smaller than those of GPANf. We tried to calculate the void size with the Rulands' streak method (see page 128-129), but the scattering intensity of Figure 5.4 (b) was too weak to extract the azimuthal scan.

5.2. Analysis of multi PAN filaments

5.2.1 Experimental

Table 1. EDS result of received PAN powder and washed PAN powder.

Element (At%)	As received	Washed
C	85.8	85
N	12.5	13.3
O	1.6	1.6
S	0.1	0.1
Na	0.1	0

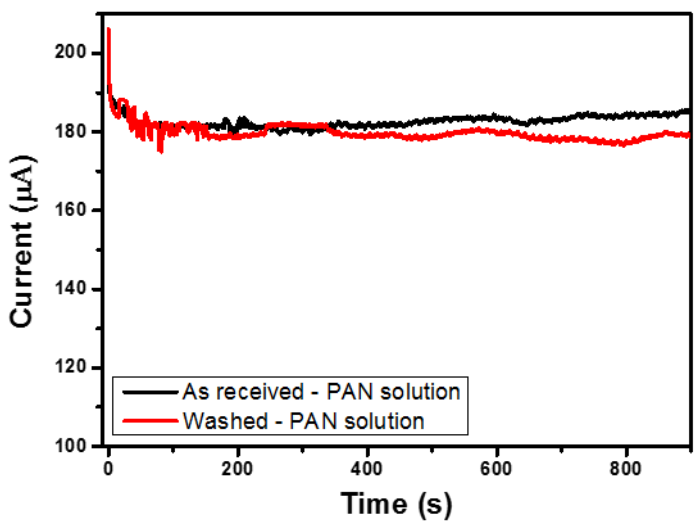

Figure 5.5. Electric current flow during wet-spinning process for as received and washed.

PAN powder was washed several times with distilled water and then dried at vacuum oven (50 °C) for 24 h. Table 1 showed EDS result of as received and washed PAN powder. In as received PAN powder, sodium element was observed. It is expected that sodium ion came from sodium bisulfate [130, 131] or sodium hydroxide [132]. Sodium bisulfate are usually used for boosting initiation rate in redox polymerization and sodium hydroxide are used for removing moisture in AN monomer. After washing several times, sodium element was removed like Table 1. PAN solution was prepared from both as received PAN powder and washed PAN powder respectively. During current-assisted wet-spinning, the constant potential (60 V) was applied to the syringe (Figure 4.9) containing each PAN solution prepared from received and washed PAN solution. Regardless of sodium contents, the constant electric current of about 180 μA flowed in both samples; sodium itself could not affect the electric current largely because of its low content (Figure 5.5). Considering that ~ 10 μA flowed in case of only DMF solvent, it was expected that there were non-faradaic (mass transfer of PAN by electrophoresis) and faradaic (redox reaction of PAN) current.

Same lab scale wet-spinning device for multi filaments (Figure 3.5) was used for conducting experiments. The detailed experiments procedure was already explained in section 3.2.1 and 4.2.1. The coagulation bath composition was 7:3 weight fraction in solvent and non-solvent mixture. Other parameters were same as the parameters introduced in section 4.2.1.

Polyacrylonitrile (co-polymer with 6 wt% methyl acrylate, PAN, MW: 80,000, Polysciences) was used and before using, water washing of PAN was conducted to remove a residual count ions (these might be from the initiator). *N,N*-dimethylformamide (DMF, purity: 99.5%, Daejung Chemical) was used as received

and solution concentration was set as 20 wt%. PAN powder was dissolved in DMF at 70 °C for 2.5 h with mechanical stirring. The prepared PAN solution was centrifuged at 6000 rpm for 15 min to perfectly dissolve PAN and to remove micro bubbles in the PAN solution simultaneously. The solution was placed in vacuum oven at room temperature for 20 min for deaeration. The PAN fibers fabricated *via* general wet-spinning for multi filaments called as MGPANf while the PAN fibers fabricated via current-assisted wet-spinning for multi filaments called as MEPANf.

5.2.2 Characterization

All fibers were dried at room temperature for at least 2 days before all characterizations. Cross-sectional shape of fibers were taken from FE-SEM (JSM-7600F, JEOL). Mechanical properties of fibers were measured using single-fiber tensile test following the ASTM D3822-07. WAXD and SAXS (D8 Discover, Bruker) were used to investigate microstructure and void information of fibers. Solvent and non-solvent contents in fibers were measured *via* simultaneous DTA/TGA analyser (SDT, TA instruments). Chemical composition of fibers was analyzed *via* H-NMR (500 MHz, Advance-500, Bruker) and XPS (AXIS-HSi, KRATOS). T_g of fibers was measured *via* dynamic mechanical analyzer (DMA, Q800, TA instruments Inc).

5.2.3 Results and discussion

5.2.3.1 Mechanical properties

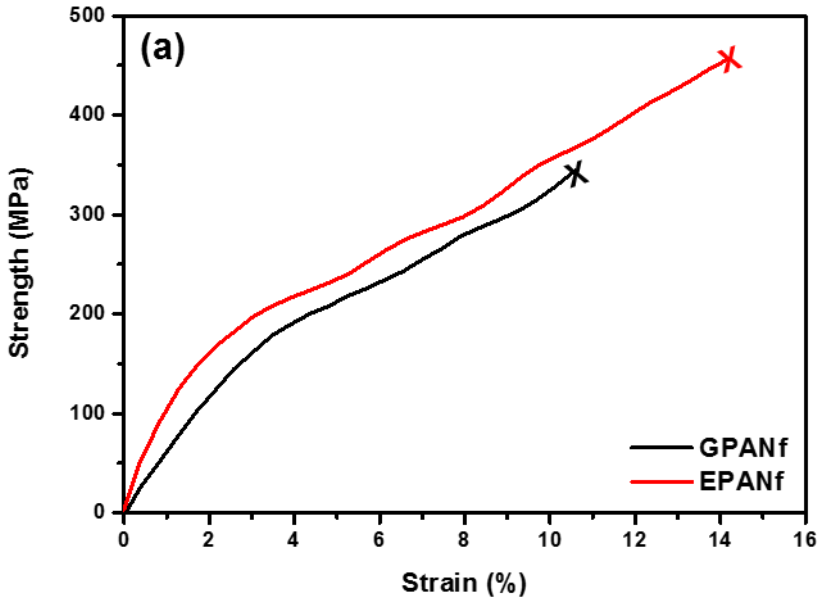
(a)
Strength (MPa)
Strain (%)
GPANf
EPANf
0
100
200
300
400
500
0
2
4
6
8
10
12
14
16

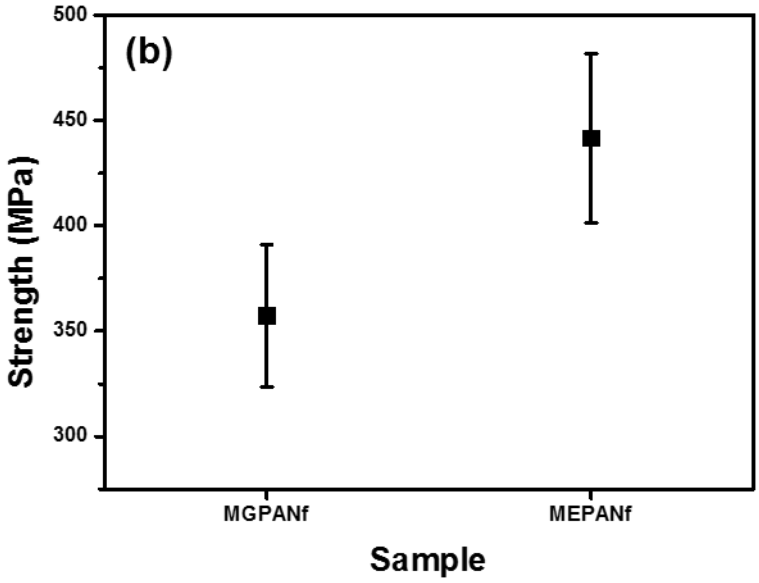
(b)
Strength (MPa)
Sample
MGPANf
MEPANf
300
350
400
450
500

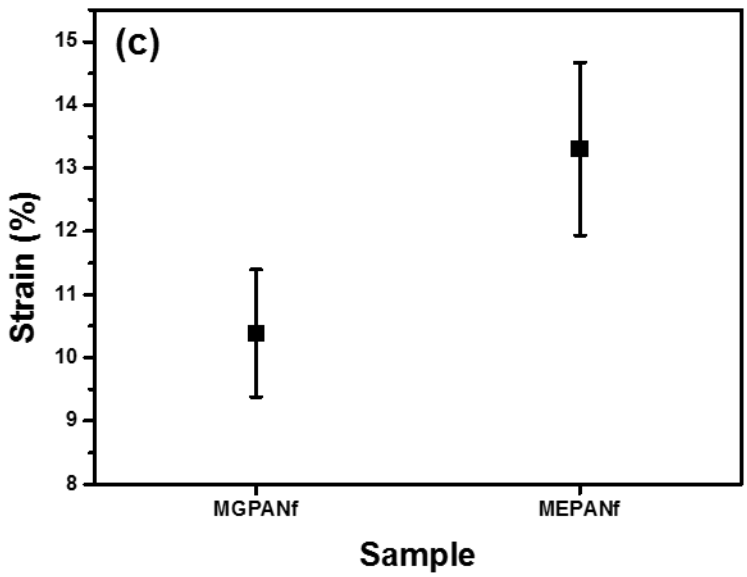

Figure 5.6. (a) S-S curve, (b) the average strength, and (c) the average strain with error bar for GPANf and EPANf.

To find the difference between MGPANf and MEPANf, tensile test was firstly conducted. The gauge length and crosshead speed were 20 mm and 10 mm/min respectively. The tensile test was repeated 30 times for each sample. Figure 5.6 (a) showed representative S-S curve of MGPANf and MEPANf. Figure 5.6 (b) and (c) were average value of strength and strain with error bar for MGPANf and MEPANf. The failure strength and strain of MEPANf were about 23 and 28% higher than those of MGPANf. To find reason for improved mechanical properties of EPANf, various characterizations were conducted.

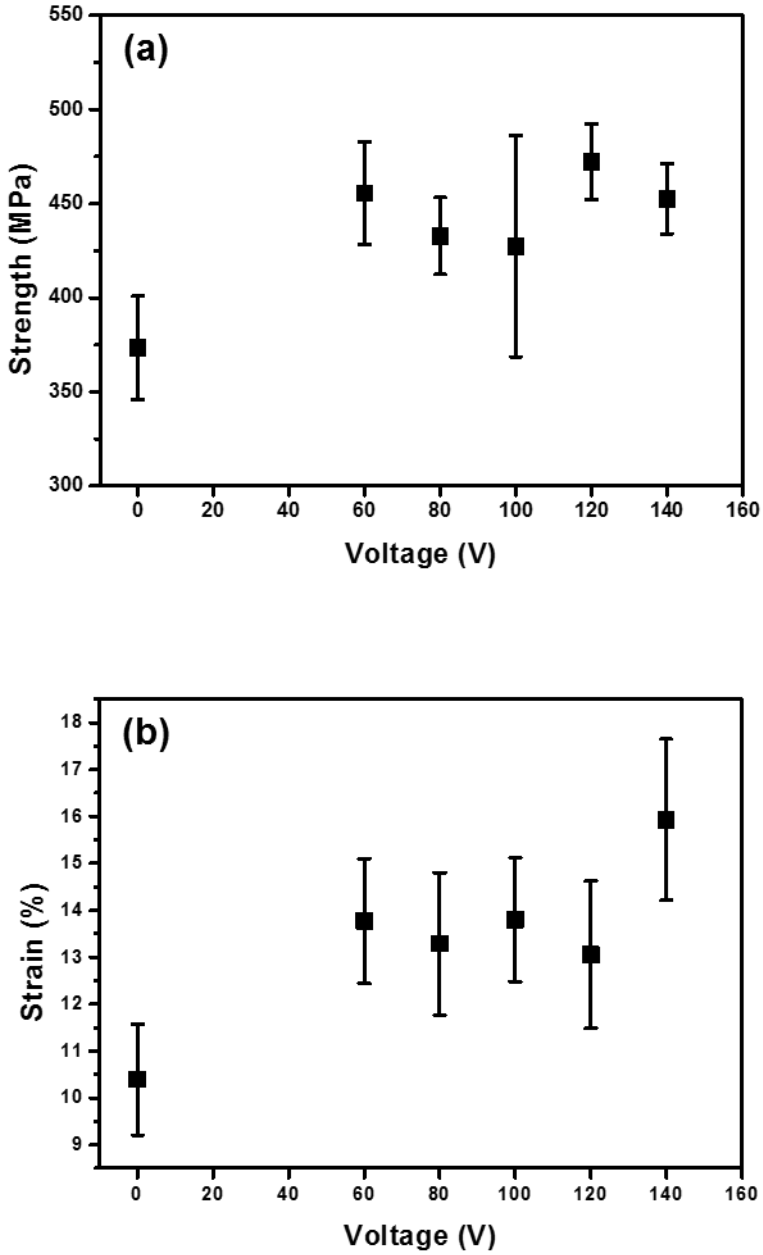

Figure 5.7. Average (a) failure strength and (b) failure strain according to applied electric potential.

Various EPANfs were fabricated with applying different electric potential (60 – 140 V) and their mechanical properties were evaluated (Figure 5.7). Their failure strength and strain were almost same after the certain threshold value of electric potential (60 V). This meant that energy for demethylation from methyl acrylate group was high enough for 60 V.

5.2.3.2 Morphological observation

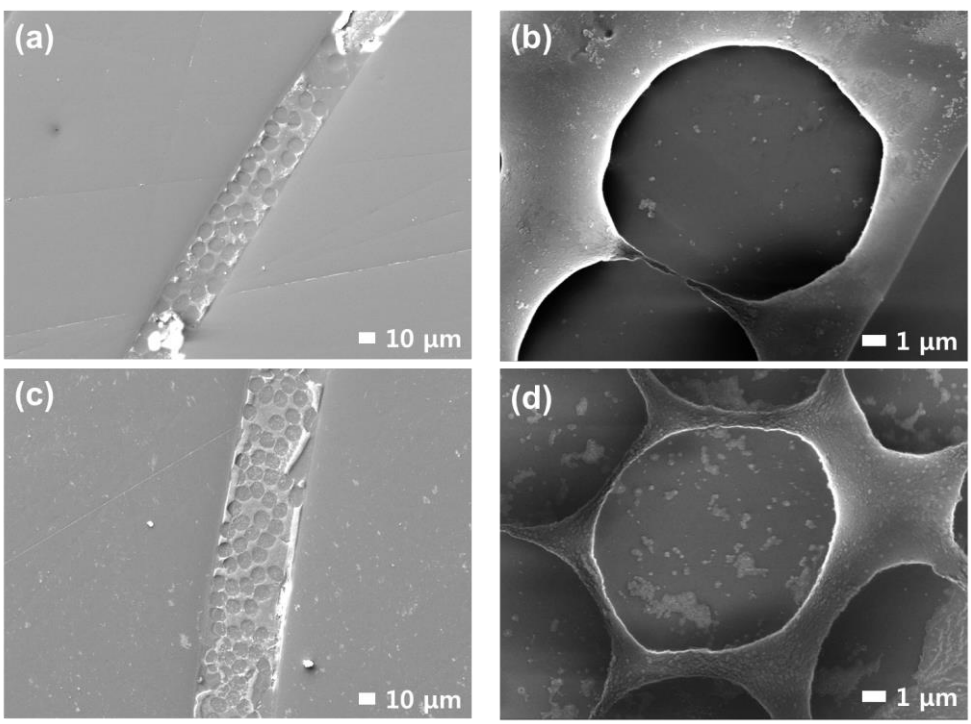

Figure 5.8. Cross-sectional SEM image at low magnification of (a) MGPANf and (c) MEPANf. At high magnification of (b) MGPANf and (d) MEPANf.

Two PAN fibers were fabricated *via* the general wet-spinning (MGPANf) and the current-assisted wet-spinning (MEPANf). Except applying 60 V to the syringe (MEPANf case), other parameters were same for two cases. Firstly, their cross-sectional shape was observed by SEM (Figure 5.8). To get the sample for SEM, fiber bundles were strongly fixed in narrow clip and epoxy resin were poured into the clip and hardened. The prepared epoxy resin was polished with sand paper and nano colloidal particles. All fibers were close to circular shape (Figure 5.8 (a) and (c)) and large cracks or voids were not observed. *Via* this, it was confirmed that coagulation process was well conducted (kidney or bean shape could be fabricated with fast coagulation rate and they are not preferred (see section 1.4)). The diameters of MGPANf (10.68 ± 0.86 μm) and MEPANf (10.93 ± 0.70) were almost same (the impurities from Figure 5.8 (b) and (d) were nano colloidal particles used in polishing process).

5.2.3.3 WAXD analysis

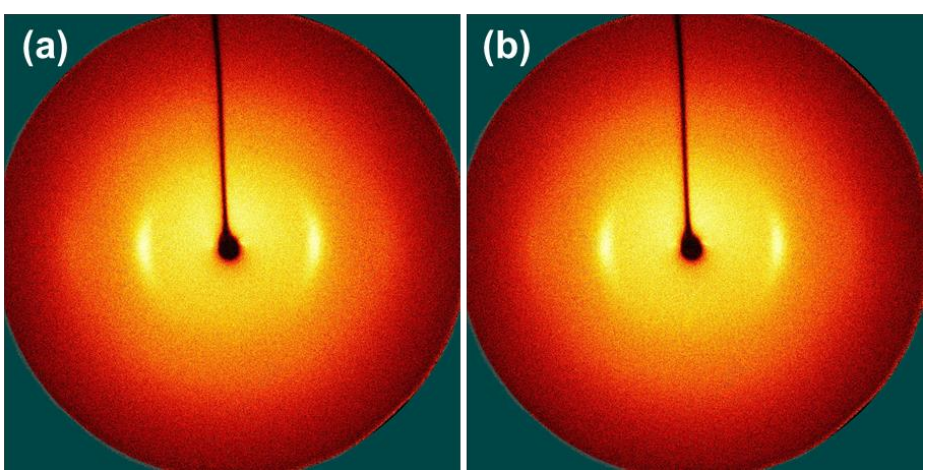

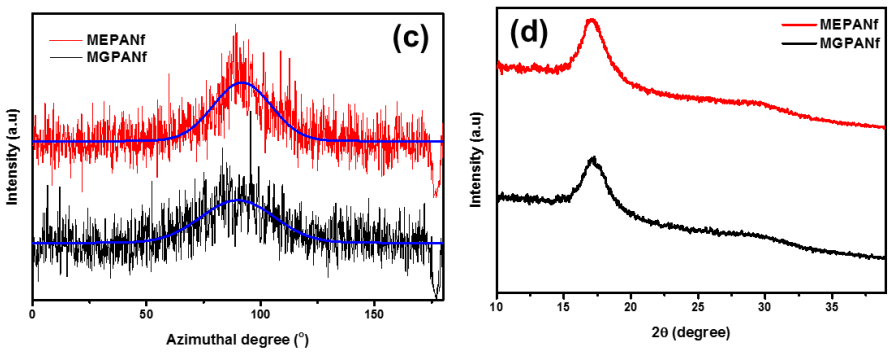

Figure 5.9. 2D-WAXD images of (a) MGPANf and (b) MEPANf. (c) Azimuthal scan of MGPANf and MEPANf which was extracted at 2θ = 16.9. (d) Equatorially extracted 1D XRD plot of MGPANf and MEPANf.

Table 2. Crystallinity and preferred orientation of MGPANf and MEPANf.

	MGPANf	**MEPANf**
Crystallinity (%)	43	42.8
Preferred orientation (%)	83	86.13

PAN fibers consist of three levels. From the lower dimension, the levels are helix structure of PAN macromolecules (Van der Waals force acting), close-packed paracrystals (rod-shaped), and fibrous crystals. One higher level structure is made of just below level structure [133, 134]. Initially, the reason for enhanced mechanical properties of EPANf was thought to be the improved microstructure of MEPANf. So 2D-WAXD analysis was performed on two samples. Strong peak at 2θ = 16.9 ° was indexed to the (100) plane of a hexagonal structure and weak peak at 2θ = 30 ° was

indexed to the (020) plane (Figure 5.9 (d)) [135]. The crystallinity of each sample was calculated based on Figure 5.9 (d). The preferred orientation (P.O) [136] of each sample was calculated from peak integration (Int. W) in azimuthal scan (Figure 5.4 (c)) which were extracted at 2θ = 16.9 ° in Figure 5.9 (a) and (b). Calculated crystallinity and P.O were listed in table 2. Crystallinity of MGPANf and MEPANf were almost same while P.O of MEPANf was a little bit higher than that of MGPANf. P.O affect tensile modulus (MGPANf: 7.64 GPa, MEPANf: 9.43 GPa) but cannot affect strength and strain largely. It was thought that electrophoresis movement of PAN chains makes better orientation in MEPANf sample. The applied potential did not affect crystallinity significantly.

5.2.3.4 TGA, DSC, and DMA analysis

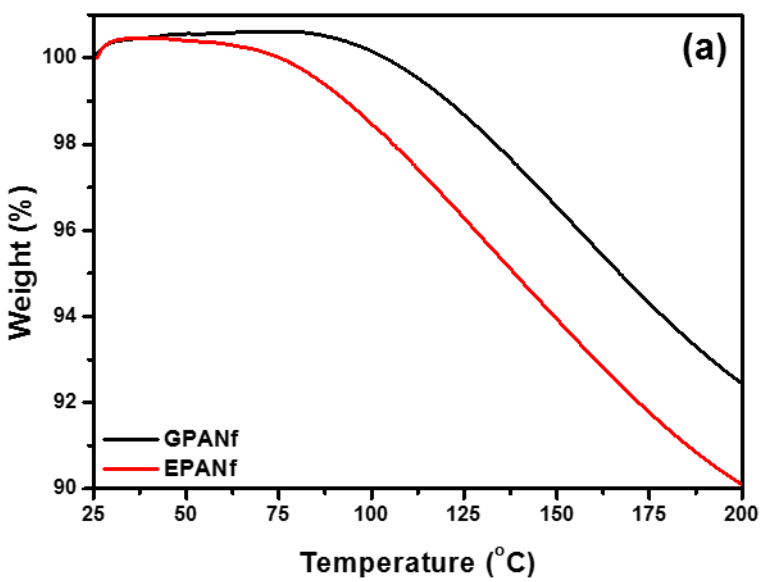

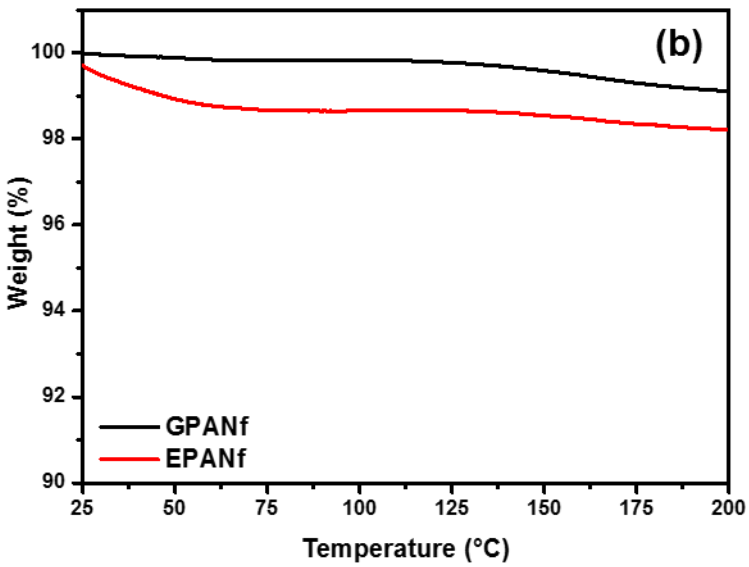

Figure 5.10. TGA comparison of GPANf and EPANf: (a) undrawn fibers and (b) drawn fibers.

TGA was measured with undrawn and drawn fibers for MGPANf and MEPANf. All samples were dried for 2 days at room temperature before measuring TGA. In both Figure 5.10 (a) and (b), the weight loss of MEPANf firstly started below 100 °C rather than MGPANf. The gap (started from around 50 °C) between MGPANf and MEPANf was 1% and it was kept constant (weight loss of water generally started below 50 °C [137]). This meant that MEPANf absorbed more non-solvent (water) than MGPANf in coagulation bath. Note that the solvent or non-solvent inside closed pores in the fibers were very difficult to remove even in vacuum at 50 °C [138]. At high temperature (> 200 °C), all liquids could be removed but it could induce change of microstructure or chemical constituent. In undrawn fibers (Figure 5.10 (a)),

weight loss kept continuing until 200 °C due to mass of solvent (DMF) but this disappeared in drawn fibers due to washing process in 3-staged bath. MGPANf plot in Figure 5.10 (b) showed a little bit higher weight loss around 150 °C rather than MEPANf. This meant MGPANf contained more DMF than MGPANf. Consequently, it could be concluded that applying potential helped the exchange between solvent and non-solvent and boost the inward tendency of non-solvent.

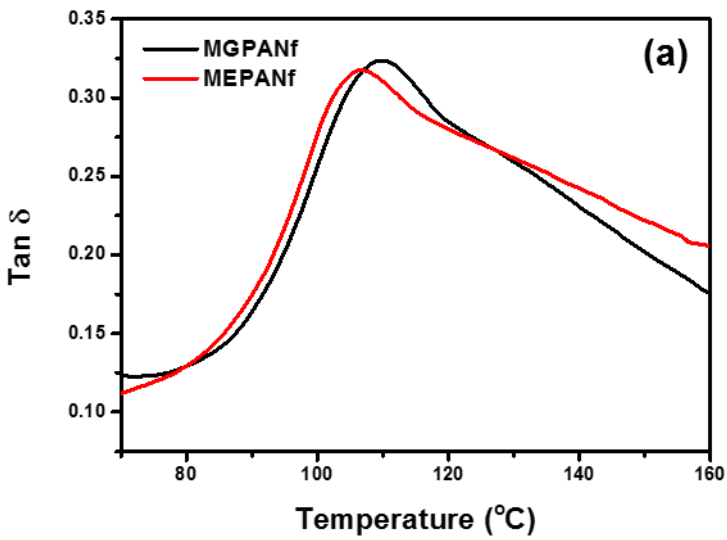

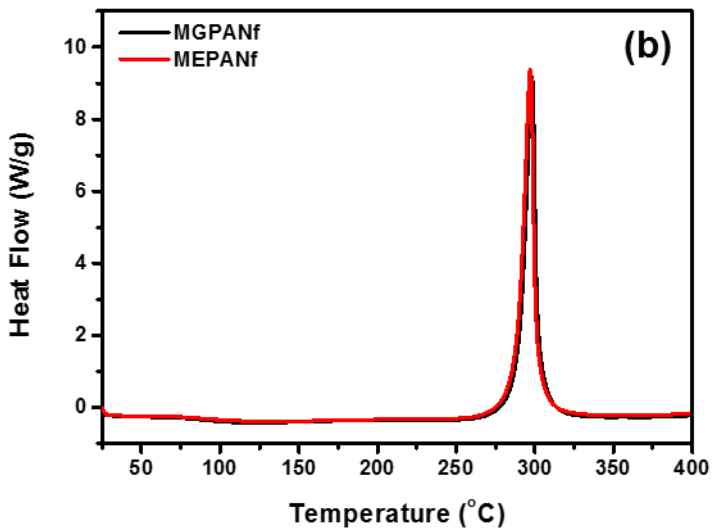

Figure 5.11. (a) Tan δ as a function of temperature and (b) DSC plot for MGPANf and MEPANf.

In order to measure glass transition temperature (T_g) of MGPANf and MEPANf, DMA was conducted on the two samples (Figure 5.11 (a)). Frequency, oscillating amplitude, and temperature increasing rate were 10 Hz, 15 μm, and 5 °C/min respectively. Generally, T_g is the temperature where the polymer segment starts to actively move due to thermal energy and it indirectly indicates the strength of secondary bonds between polymer chains. In Figure 5.10, MGPANf showed a peak around 110 °C (MGPANf T_g) and this was similar with other PAN fiber [44]. However, MEPANf showed a peak around 106 °C (MEPANf T_g), which was lower than that of MGPANf. This was because the secondary bond points were reduced due to demethylation of MA. Meanwhile, DSC (Figure 5.11 (b)) also showed similar result with DMA. For cyclization (stabilization) reaction of PAN, DSC was

conducted in air atmosphere. The peaks in Figure 5.11 (b) meant exothermic reactions such as cylization, dehydrogenation and oxidation to form a cyclized ladder type structure. The cyclization peaks MGPANf and MEPANf appeared at 298.11 and 297.14 °C, respectively. And their enthalpy was 575.7 and 586.6 J/g, respectively. The higher enthalpy value indicate that more PAN molecules participate in the reaction [139]. These observations might be attributed to relatively free molecular mobility of PAN chins in MEPANf due to the less secondary bond points than in MGPANf.

5.2.3.5 SAXS analysis

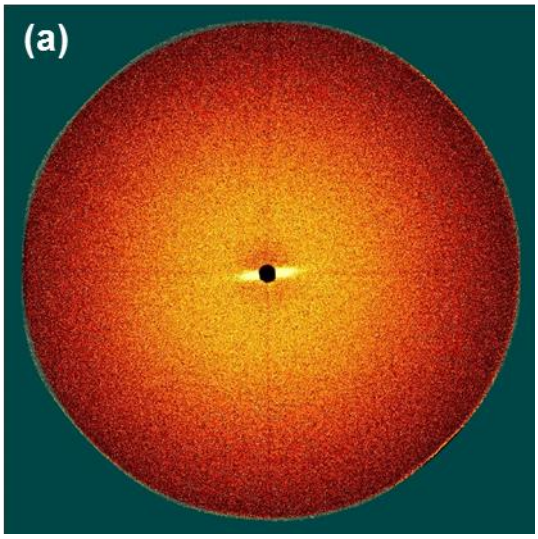

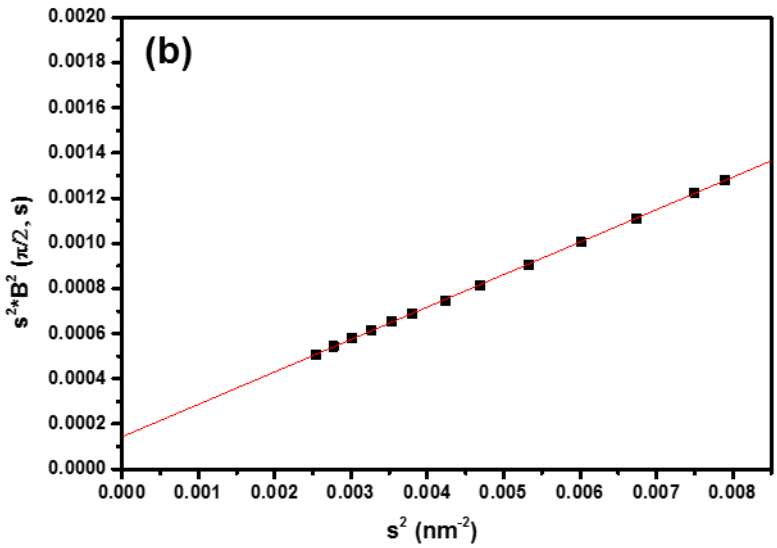
(b)
0.0020
0.0018
0.0016
0.0014
0.0012
0.0010
0.0008
0.0006
0.0004
0.0002
0.0000
s²*B² (π/2, s)
0.000
0.001
0.002
0.003
0.004
0.005
0.006
0.007
0.008
s² (nm⁻²)

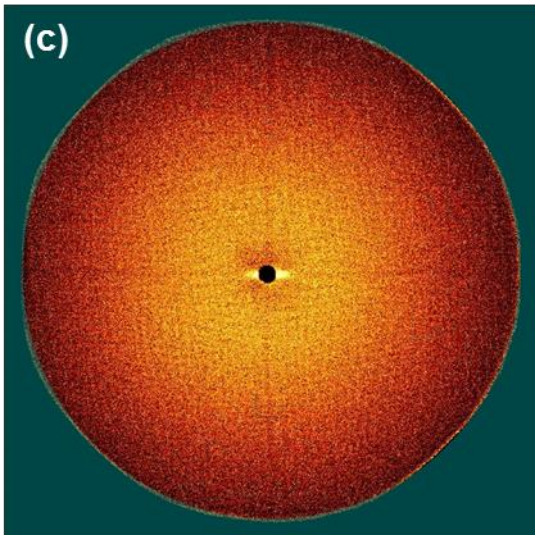
(c)

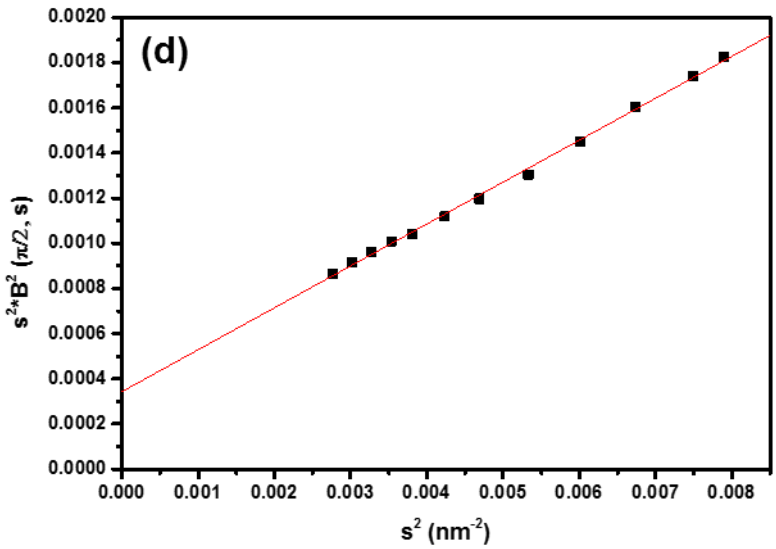

Figure 5.12. 2D-SAXS images of (a) MGPANf and (c) MEPANf. s^2*B^2 VS s^2 sacttering plot and linear fitting of (b) MGPANf and (d) MEPANf.

SAXS analysis is useful method to investigate the microvoid structure of the PAN precursor or carbon fibers [140-144]. 2D-SAXS scattering intensity included void information due to the difference in electron density between voids and PAN matrix. It was assumed that the microvoids inside PAN fibers were considered as a cylinder shape and it was assumed that dilute system of elongated microvoids (cylinder shape) was oriented with fiber axis. Average void length and angle could be calculated *via* Ruland's streak analysis method [140]. Firstly, azimuthal scans according to 2θ (gamma integration) were extracted from 2D-SAXS image (Figure 5.12 (a) and (c)) and s could be calculated from $s = 2\sin\theta/\lambda$ where λ was wavelength of incident X-ray beam (0.1542 nm)

$$B_{\pi/2}(s) = \frac{1}{I(s,\pi/2)} \int I(s,\varphi) d\varphi \quad \textbf{(1)}$$

$B_{\pi/2}$ (s), the integral breadth, could be calculated from equation (1) where $I(s,\pi/2)$ was the height of the peak in azimuthal scan at $\pi/2$ in certain s and $\int I(s, \varphi)d\varphi$ was the area of the peak in azimuthal scan.

$$s^2 B_{\pi/2}^2\ (s) = 1/L_c^2 + s^2 B_{eq}^2 \quad \textbf{(2)}$$

From the equation (2), scattering points of MGPANf and MEPANf was plotted and their intercept and slope was calculated *via* linear fitting (Figure 5.8 (b) and (d)). Average void length (L_c) and angle (B_{eq}) were square root invers of the intercept and square root of the slope. The calculated void information of MGPANf and MEPANf were listed in Table 3. The void length of MEPANf was lower than that of MGPANf by about 30%. Artur Rozanski et al. investigated void formation of bare polymer and non-solvent absorbed polymer *via* in-situ SAXS with drawing process [145]. In case of non-sovlent absorbed polymer, the size of pores containing non-solvent was not enlarged anymore during drawing. Furthermore cavitation (newly formed voids *via* drawing), which could be caused by drawing, was also prohibited due to non-solvent deeply penetrating into the polymer. As strain applied to the samples increased, the 2D-SAXS intensity of bare polymer increased while that of non-solvent absorbed polymers was not changed at al. Like this, voids enlargement and cavitation of MEPANf (more non-solvent absorbed sample: Figure 5.10) was prohibited during drawing process so mechanical properties of MEPANf increased rather than MGPANf. The reason for increased void angle of MEPANf (20.67 ° → 23.72 °)

thought to be that the voids including non-solvent would more resist to drawing than bare voids. Thus, the extra force would be applied to PAN matrix adjacent to voids and the matrix more aligned (that's why the orientation of MEPANf is higher than that of MGPANf).

Table 3. Voids information of MGPANf and MEPANf.

	MGPANf	**MEPANf**
Void length (nm)	74.35	52.11
Void angle (°)	20.67	23.72

5.2.3.6 Chemical constituent analysis

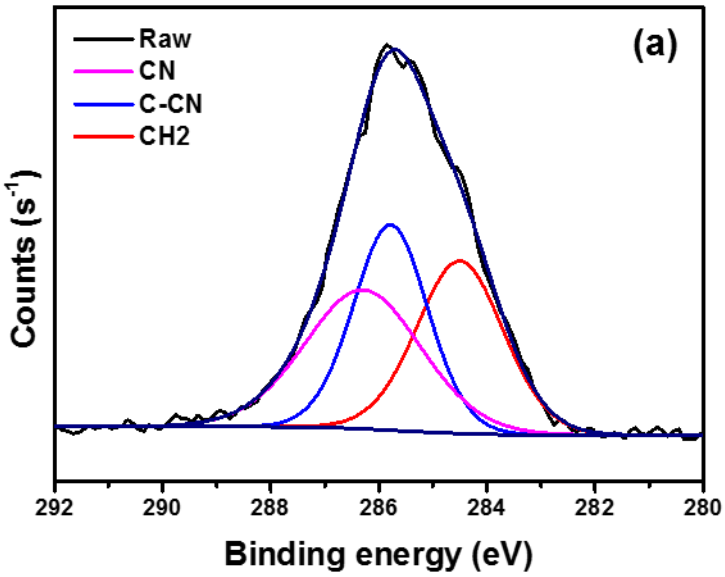

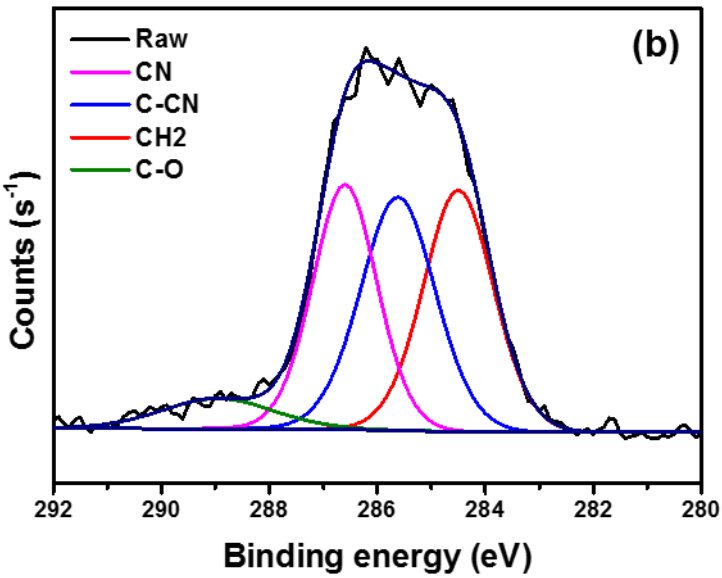
Raw
CN
C-CN
CH2
C-O
(b)
Counts (s-1)
292
290
288
286
284
282
280
Binding energy (eV)

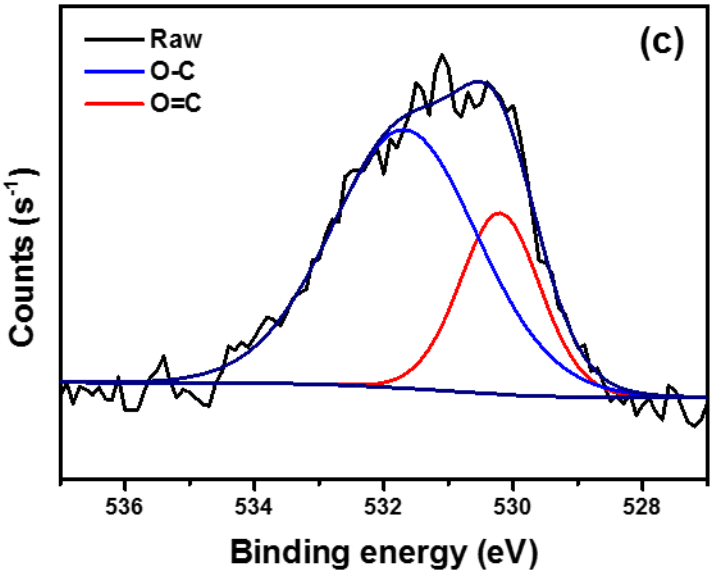
Raw
O-C
O=C
(c)
Counts (s-1)
536
534
532
530
528
Binding energy (eV)

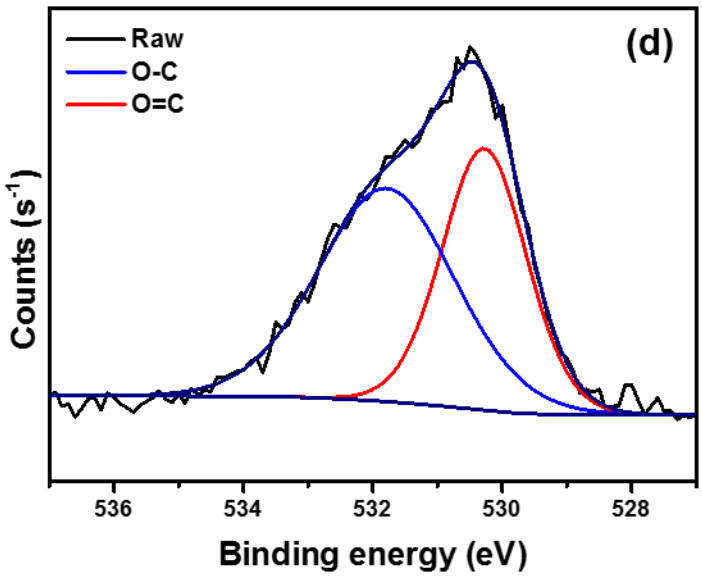

Figure 5.13. C1s XPS spectra (a) MGPANf and (b) MEPANf. O1s XPS spectra (c) MGPANf and (d) MEPANf.

To find change in chemical composition and constituent, the surface chemistry of the fibers was examined using XPS, which included the information of the top 1-10 nm of the fiber surface. C 1s spectra was shown in Figure 5.13 (a) and (b) for MGPANf and MEPANf respectively. Deconvoluted peaks were observed around at 288.9, 286.3, 285.8, and 284.5 and they were attributed to O-C=O, C≡N, C-CN, and CH_2 bondings respectively [146-148]. The O-C=O came from the copolymer, polymethylacrylate (PMA) in PAN (co-polymer with 6 wt% methyl acrylate, Polyscience). The peak attributed to O-C=O bonding was only observed in Figure 5.13 (b) (MEPANf). Figure 5.13 (c) and (d) showed O 1s spectra for MGPANf and MEPANf; 531.7 and 530.2 eV were attributed to C-O and C=O bondings. The

intensity of C-O bond and C=O decreased and increased respectively in MEPANf sample (Figure 5.13 (d)) rather than MGPANf (Figure 5.13 (c)) [149, 150]. In other words, methyl group of methylacrylate was detached in MEPANf sample. Carboxylate ion formed from demethylation in MEPANf attracted more water molecules in coagulation process (Figure 5.10). With this, it was predicted that attraction force between carboxylate ion and water molecules partially made carboxylate ions arrange to the fiber surface in MEPANf (basically, PMA also existed as helical structure in fibers like PAN [134]). So O-C=O bonding appeared in MEPANf (Figure 5.13 (b)), which was not shown in MGPANf (Figure 5.13 (a)) due to relatively weaker intensity than that of carbon. So it could be concluded that demethylation in methyl acrylate group occurred in MEPANf due to applied electric potential, which leads to formation of carboxylate negative ions in PAN chains. These ions attracted more non-solvent in coagulation bath because non-solvent (distilled water: 80) has a higher dielectric constant than solvent (DMF: 38.3).

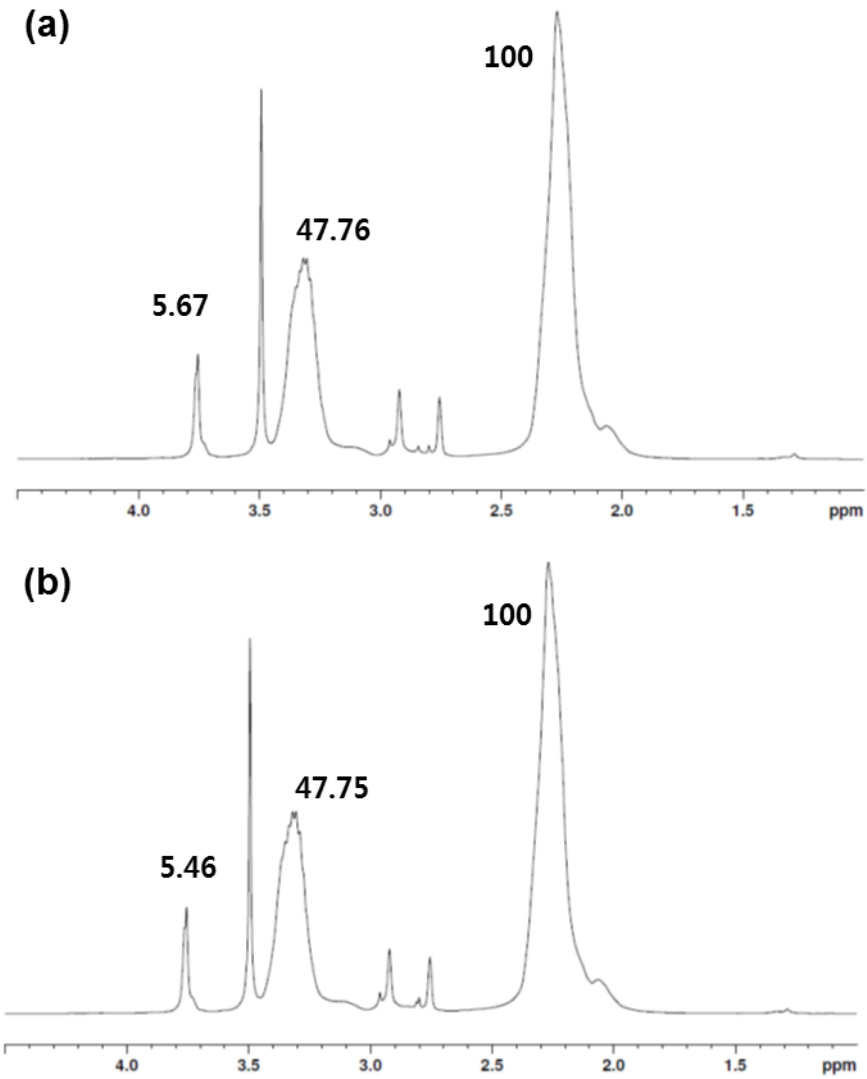

Figure 5.14. H-NMR of (a) MGPANf and (b) MEPANf.

MGPANf and MEPANf were dissolved in deuterated DMF (DMF-d) and H NMR was conducted to clarify chemical portion of each sample (Figure 5.14). The peaks at 3.75, 3.3, and 2.25 ppm were assigned as CH_3 in methylacrylate, CH in back bone of chain, and CH_2 in back bone of chain respectively [151]. The ratio of area of peaks

is the ratio of number of H in each group. According to Figure 5.14, two samples showed almost 6 wt% of methylacrylate, which was same with the original PAN powder. The other peak ratios were calculated by setting the area of the CH_2 peak to 100. The number of CH_3 in MEPANf (Figure 5.14 (b)) was more decreased than that of MGPANf (Figure 5.14 (a)) (5.67 → 5.46). Although the reduction was small, the same results (reduced number of CH_3 in MEPANf) was repeated for every test. It was predicted that most of detached methyl groups would return to original position (carboxylate ion) in coagulation bath and some of methyl groups would diffuse into coagulation (HNMR difference between MGPANf and MEPANf would be attributed to the methyl groups diffused into coagulation bath). Summarily, HNMR also showed same result of demethylation in MEPANf likewise the results of XPS, DMA, and DSC. Some researches revealed that methyl group in PMMA was detached by hydrolysis at mild conditions [150, 152]. The detached methyl was reacted with hydroxide from water, which leads to methanol formation. Residual hydrogen ion was attached to carboxylate ion at which originally methyl group existed. Another research showed that the bond length of O-CH_3 in triacetin became longer (other length of bonds in triacetin became shorter) as external electric field increased [153]. These papers directly and indirectly dealt with possibility of demethylation.

Table 4. GPC analysis of GPANf and EPANf

	MGPANf	**MEPANf (60 V)**	**EPANf (400 V)**
Mn	243952	246893	249313
MW	288156	292193	303019
PDI	1.18	1.18	1.22

To find out whether the applied electric potential or flown electric current affected the backbone of PAN chains, GPC was performed for both MGPANf and MEPANf samples (Table 4). MGPANf and MEPANf showed similar Mn, MW, and PDI values. Even the MEPANf fabricated with applying high voltage (400 V) showed also the similar results to other samples. With this, applied electric potential or flown electric current does not affect the backbone of PAN chains.

5.3. Summary

For current-asssited wet-spinnig process in both for single filament and multi filaments, syringe pump and syringe were self-designed. GPANf and EPANf were compared *via* various characterization methods. EPANf exhibited more than 20% better mechanical properties than GPANf in both single filament and multi filaments. EPANf absorbed more non-solvent during coagulation process than GPANf due to carboxylate ions formed from demthylation in methyl acrylate group. Demethylation of EPANf was proved through XPS, NMR, DMA, and DSC. More non-solvent absorbed EPANf showed smaller size of voids than GPANf. Due to the suppressed void enlargement and cavitation during drawing process, EPANf had higher mechanical properties than GPANf.

6. Current-assisted wet-spinning mechanism

We proved basic mechanism of improved mechanical properties of EPANf which fabricated *via* current-assisted wet-spinning. To further investigate the mechanism, various PAN solution was prepared for current-assisted wet-spinning for multi filaments. Firstly, MA content in PAN was controlled by mixing original PAN (MA 6wt%) with pure PAN. If MA content is low, the increase of mechanical properties in MEPANf is expected to decrease. Another approach was the preparation of CNT-PAN incorporated solution. CNT is typical hydrophobic material and it was predicted that hydrophobic CNT would block more non-solvent uptake caused by applying electric potential. Detailed would be explained below.

6.1. Experimental

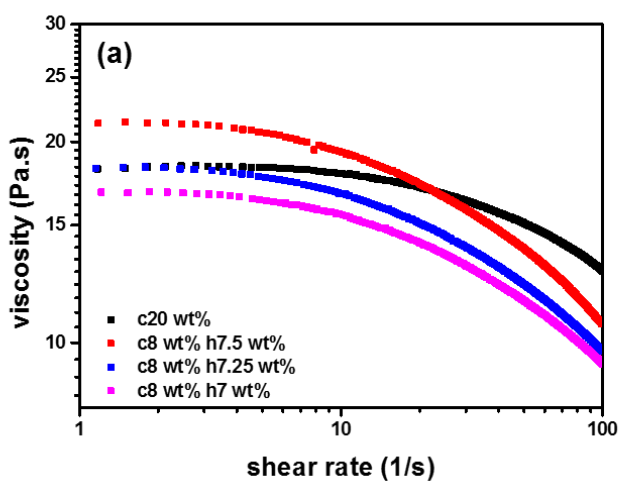

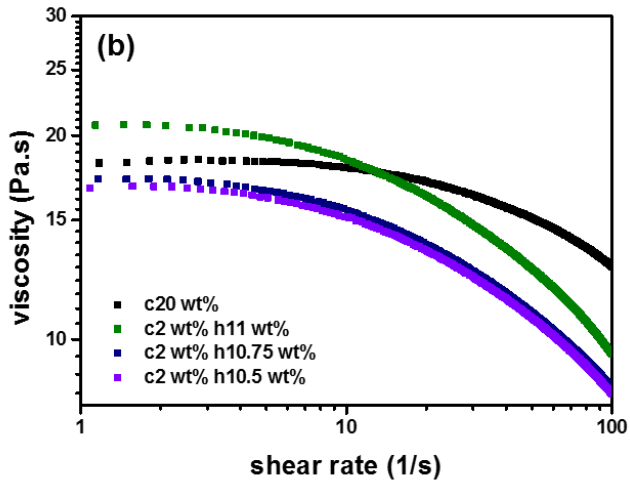

Figure 6.1. Viscosity of various solution. (a) solution containing MA 3 wt% and (b) solution containing MA 1 wt%.

To prepare PAN solution with different MA contents, original PAN (coPAN) powder (copolymer with methyl acrylate 6 wt%, Mw: 80,000 g/mol, Polyscience) was mixed with pure PAN powder (MW 200,000 g/mol, Polyscience). Due to high molecular weight of pure PAN, originally used 20 wt% concentration of mixed PAN solution can result in very high viscosity. PAN solution with high viscosity is impossible to be spun. So various mixed PAN solutions (solution preparation procedure was same with the procedure introduced in section 5.2.1) were prepared to match the zero-viscosity (18 Pa·s) of 20 wt% coPAN solution (Figure 6.1). The total concentration of the mixed solution containing 3 wt% of MA was set as 15.25 wt% (coPAN 8 wt% + pure PAN 7.25 wt%), and the total concentration of the mixed solution containing 1 wt% of MA was set as 12.8 wt% (coPAN 2 wt% + pure PAN 10.8 wt%). Due to low total concentration of two mixed PAN solutions, shear thinning behavior was

started at more early shear rate than 20 wt% coPAN solution. However, the shear rate applied during wet-spinning process with the certain flow rate (23.7 ml/h) was lower than the point where shear thinning occurred at both two mixed PAN solution. So shear thinning would not happen during wet-spinning. The prepared solutions were spun with the same wet-spinning parameters of MGPANf and MEPANf (see section 5.2.1). From now on, the fibers spun from MA 1 wt% PAN solution were called as 1GPANf and 1EPANf while the fibers spun from MA 3 wt% PAN solution were called as 3GPANf and 3EPANf (MGPANf and MEPANf in section 5.2 were called 6GPANf and 6EPANf).

CNT incorporated PAN solution was prepared as followed. Firstly, 0.1 and 0.5 wt% of MWNT (diameter: 8-15 nm, length: 0.5-2 μm, purity: > 95%, Nanosturctured & Amorphous Materials, Inc.) were dispersed in DMF respectively *via* tip sonicator (1 sec on and 1 sec off for 3 h). Then, 20 wt% of PAN powder was added to the prepared CNT-DMF solution and dissolved at 70 °C for 2.5 h with mechanical stirring. The prepared solution was centrifuged with 6000 rpm for 15 min. For deaeration, the solution was placed in vacuum oven for 20 min. CNT-PAN solution was spun with the same wet-spinning parameters of 6GPANf and 6EPANf.

6.2. Characterization

All fibers were dried at room temperature for at least 2 days before all characterizations. Cross-sectional shape of fibers were taken from FE-SEM (JSM-7600F, JEOL). Mechanical properties of fibers were measured using single-fiber tensile test following the ASTM D3822-07. WAXD and SAXS (D8 Discover, Bruker) were used to investigate microstructure and void information of fibers. Solvent and

non-solvent contents in fibers were measured *via* simultaneous DTA/TGA analyser (SDT, TA instruments). Through potentiostat (PGSTAT302N, Metrohm Autolab) cyclic voltammetry was conducted on PAN solutions to investigate the redox reaction.

6.3. Results and discussion

6.3.1 PAN filaments with different methyl acrylate content

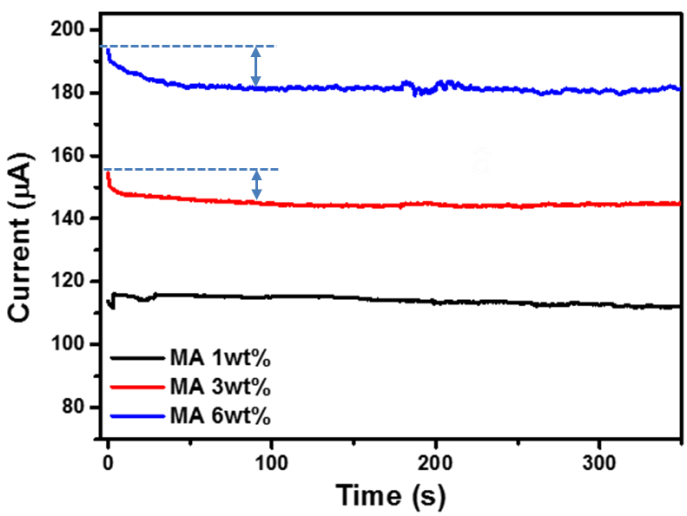

Figure 6.2. Electric current flow during wet-spinning process for PAN solution with different MA contents.

The applied electric potential was equal to 60 V for all EPANf samples. The electric current flow during current-assisted wet spinning process was shown in Figure 6.2 according to different MA contents in PAN solution. The electric current of all samples remained constant during the process (Figure 6.2). As MA contents

decreased, the electric current also decreased (180, 145, 115 μA). The reason for reduction in electric current thought to be that 1. The reduction in total concentration (20 wt% → 15.25 wt% → 12.8 wt%) decreased non-faradaic current caused by mass transfer of PAN chains (sulfate in the end group of PAN chains has negative charge which could be reacted to electric field). 2. The certain possibly reductive species (methyl group detached from methyl acrylate) were reduced due to low MA contents and low total concentration. Moreover, saturation current value from initial current to constant current was different for solutions: 13, 10, 0 μA for MA 6, 3, 1 wt% respectively. It meant that the number of ions decreased as MA content decreased.

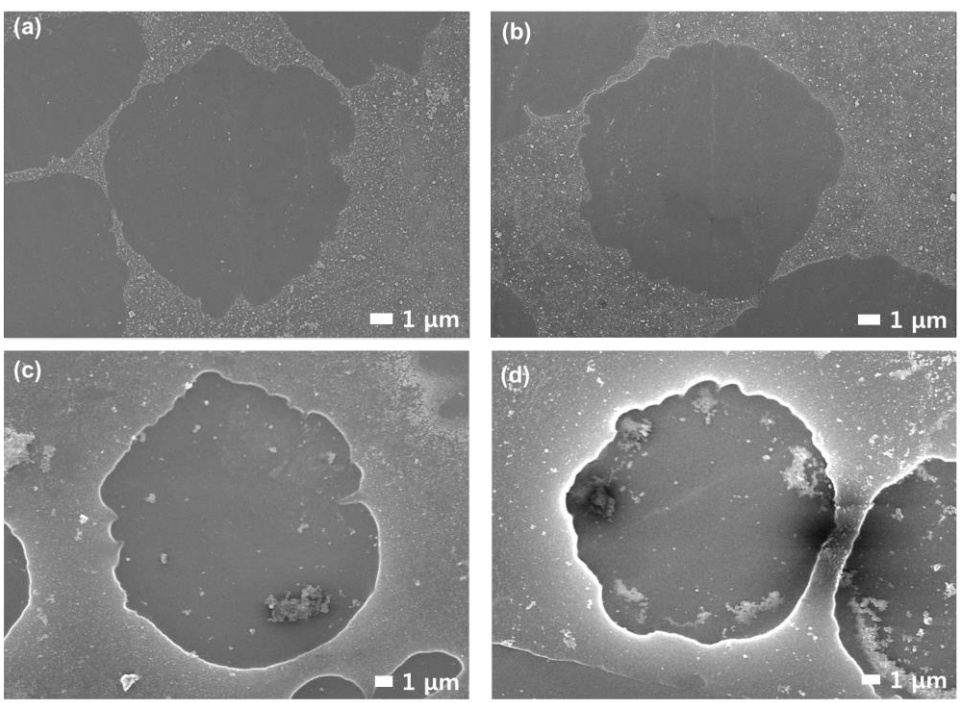

Figure 6.3. Cross-sectional shape of (a) 1GPANf, (b) 1EPANf, (c) 3GPANf, and (d) 3EPANf.

The cross-sectional shape of each fiber was analyzed *via* FE-SEM (Figure 6.3). All cross-section of fibers were close to circular shape and there were no big difference in GPANf and EPANf. However, unlike cross-section of 6GPANf and 6EPANf (Figure 3.9), the surface roughness of fibers (Figure 6.3) increased a lot because low concentrated PAN solution triggered re-dissolution in coagulation bath by lower phase separation force [27]. Their diameters was a little bit decreased after applying electric potential (1GPANf: 13.60 μm → 1EPANf: 12.32 μm, 3GPANf: 13.86 μm → 3EPANf: 12.42 μm, each diameter was average value measured from 100 points in optic images of fibers)

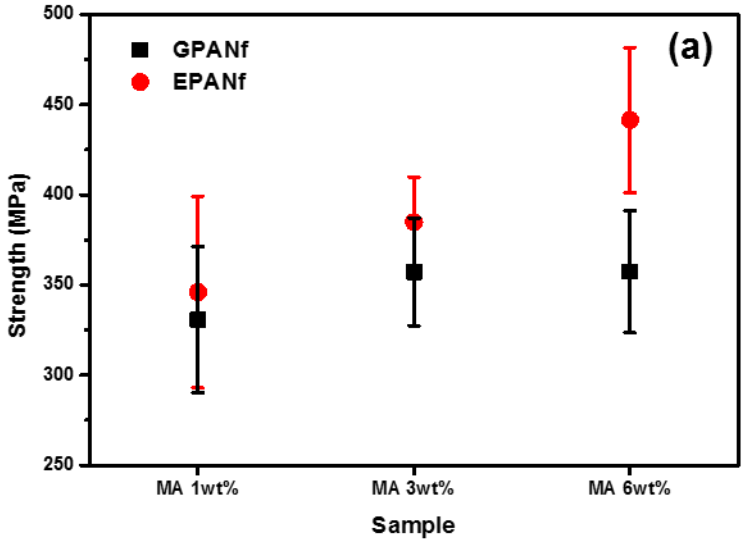

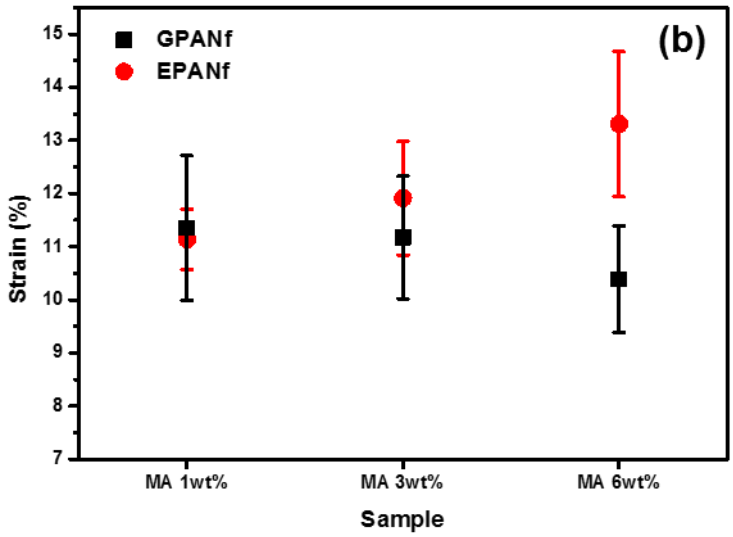

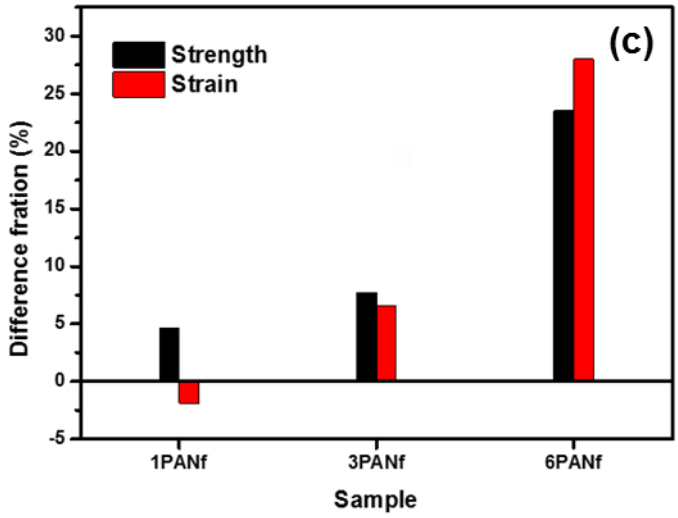

Figure 6.4. (a) Average failure strength, (b) average failure strain, and (c) strength and strain difference for GPANf and EPANf according to MA contents.

Tensile test was performed to evaluate the mechanical properties of fibers. For the

comparison, mechanical properties of 6GPANf and 6EPANf (Figure 5.6) were also added in Figure 6.4. As MA content increased, the strength of GPANf also showed increasing tendency but the difference was not large (Figure 6.4 (a)). Especially, the failure strength of 3GPANf and 6GPANf was almost similar. This was because high molecular weight of pure PAN in 3GPANf would compensate lower concentration of dope containing MA 3 wt%. It seemed that the low strength of 1GPANf was due to low concentrated dope (11.8 wt%). While the strength of EPANf certainly increased as MA content increased. So the difference of the failure strength between GPANf and EPANf increased sequentially with increasing MA content (4.6% (15 MPa) → 7.7% (27 MPa) → 23.5% (84 MPa)) (Figure 6.4 (c)). The failure strain of GPANf and EPANf was decreased and increased, respectively (Figure 6.4 (b)). The difference of the failure strain between GPANf and EPANf also sequentially increased with increasing MA content (-1.86% → 6.6% → 28%) (Figure 6.4 (c)). Note that considering error bar, 1GPANf and 1EPANf exhibited almost similar mechanical properties. The microstructure of fibers was evaluated *via* 2D-WAXD (Figure 6.5) and from it, crystallinity (Figure 6.5 (g) and (h)) and preferred orientation (Figure 6.5 (e) and (f)) were calculated (Table 5). Like 6GPANf and 6EPANf (Figure 5.9 (d)), strong peak at $2\theta = 16.9$ ° and weak peak at $2\theta = 30$ ° were observed (Figure 6.5 (g) and (h)). The crystallinity difference between GPANf and EPANF was not much large but preferred orientation difference sequentially increased as MA content increased (1GPANf and 1EPANf: 1.3% → 3GPANf and 3EPANf: 1.8% → 6GPANf and 6EPANf: 3.13%) (Figure 6.6). Accordingly, the difference in modulus, which is dependent on orientation, sequentially increased (11% → 16% → 23%).

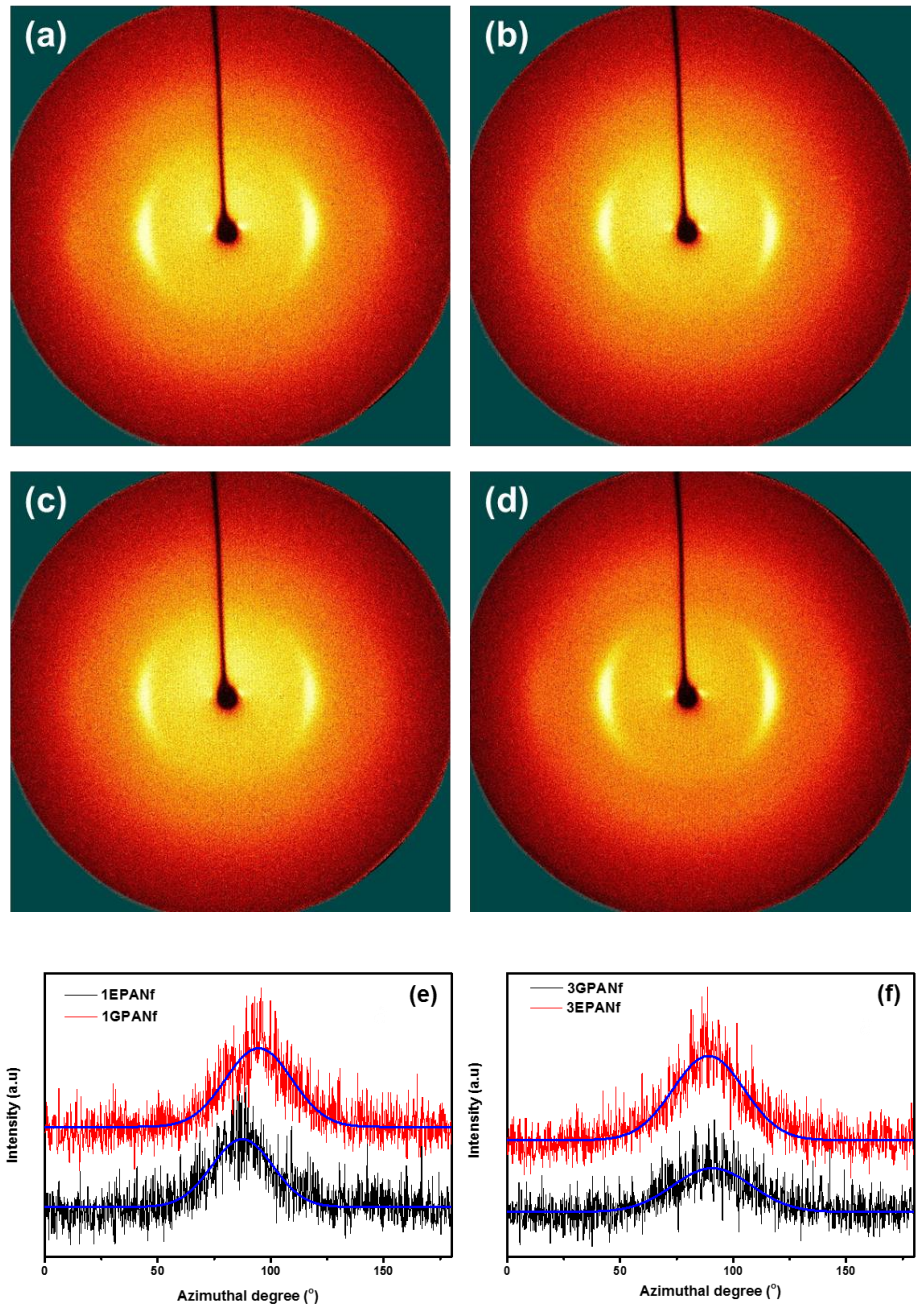
(a)
(b)
(c)
(d)
1EPANf
1GPANf
(e)
Intensity (a.u)
0
50
100
150
Azimuthal degree (°)
3GPANf
3EPANf
(f)
Intensity (a.u)
0
50
100
150
Azimuthal degree (°)

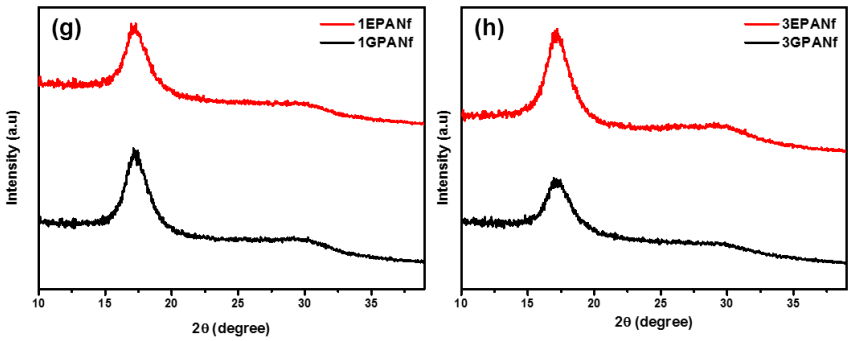

Figure 6.5. 2D-WAXD images of (a) 1GPANf, (b) 1EPANf, (c) 3GPANf, and (d) 3EPANf. Azimuthal scan of (e) 1PANf and (d) 3PANf extracted from 2θ=16.9 °. Equatorially extracted 1-D XRD plot of (g) 1PANf and (h) 3PANf.

Table 5. Crystallinity and preferred orientation of GPANf and EPANf.

	1GPANf	**1EPANf**	**3GPANf**	**3EPANf**
Crystallinity (%)	43.4	42.8	42.6	41.4
Preferred orientation (%)	83.66	84.96	80.73	82.53

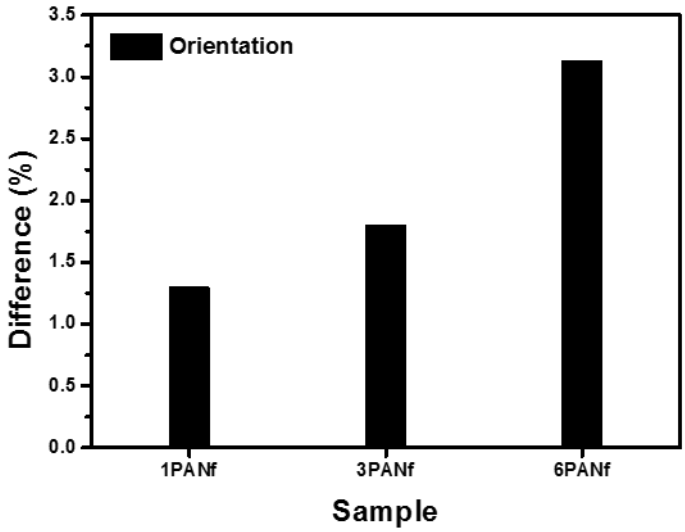

Figure 6.6. Preferred orientation difference between GPANf and EPANf according to MA contents.

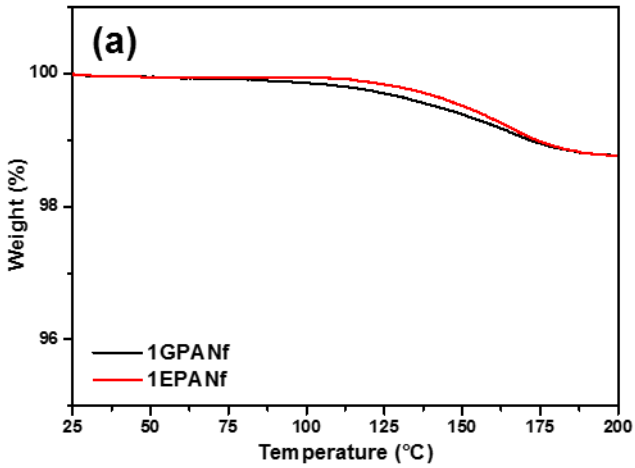

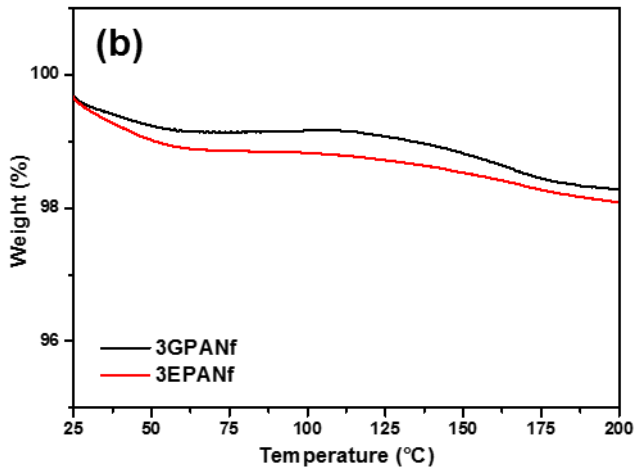

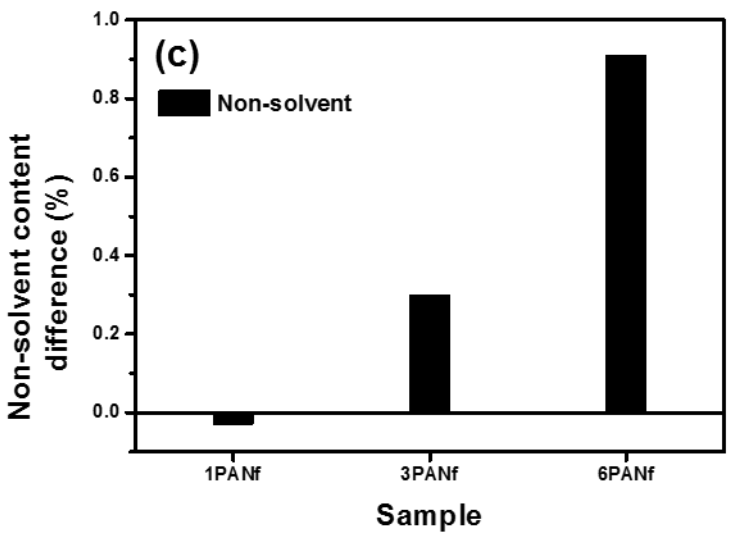

Figure 6.7. TGA comparison of GPANf and EPANf: (a) MA 6 wt% and (b) MA 1 wt%. (c) Non-solvent content difference between GPANf and EPANf.

TGA was analyzed for evaluating absorbed non-solvent difference between GPANf

and EPANf like Figure 5.10 (b). As shown in Figure 6.6 (a), unlike the other samples, 1GPANf absorbed more non-solvent than 1EPANf below 100 °C but the value of more absorbed non-solvent was little difference as 0.03%. And over 100 °C, weight loss, which might be attributed to solvent (DMF), was observed for both samples and DMF content was same for both samples as 1.1% (see the weight loss of 1GPANf and 1EPANf from 100 °C to 200 °C). In Figure 6.6 (b), weight of 3GPANf and 3EPANf reduced simultaneously from 25 °C. The difference in non-solvent content between 3GPANf and 3EPANf was 0.3%, which was higher than the difference between 1GPANf and 1EPANf (0% in Figure 6.6 (a)) and lower than the difference between 6GPANf and 6EPANf (0.91% in Figure 5.11 (b)). In Figure 6.7 (c), the difference in non-solvent content increased as MA content increased. The DMF content in 3GPANf and 3EPANf were 0.83% and 0.7% respectively (6GPANf and 6EPANf were 0.6% and 0.43% respectively). Except 1GPANf and 1EPANf, generally GPANf contained more DMF content than EPANf. As MA content increased, overall DMF content in fibers decreased. Due to applied electric field, the exchange between solvent and non-solvent was accelerated and the effect was larger as MA content increased.

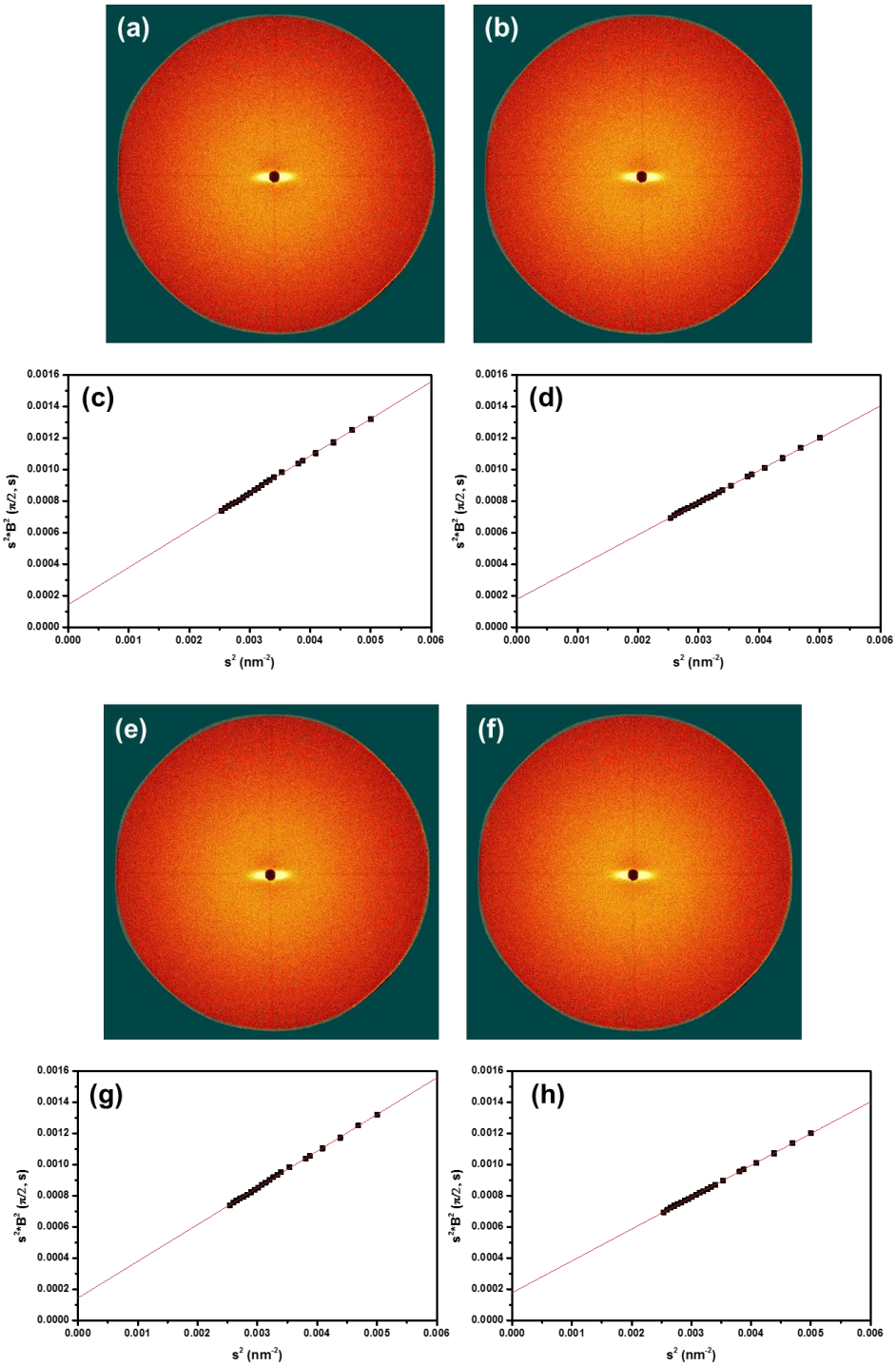
(a)
(b)
(c)
(d)
(e)
(f)
(g)
(h)
s²*B² (π/2, s)
s² (nm⁻²)
0.0000
0.0002
0.0004
0.0006
0.0008
0.0010
0.0012
0.0014
0.0016
0.000
0.001
0.002
0.003
0.004
0.005
0.006

Figure 6.8. 2D-SAXS images of (a) 1GPANf, (b) 1EPANf, (e) 3GPANf, and (f) 3EPANf. s^2*B^2 VS s^2 sacttering plot and linear fitting of (c) 1GPANf, (d) 1EPANf, (g) 3GPANf, and (h) 3EPANf.

Table 6. Void information of GPANf and EPANf.

	1GPANf	**1EPANf**	**3GPANf**	**3EPANf**
Void length (nm)	83.51	75.10	110.75	92.52
Void angle (°)	27.81	25.89	28.86	27.79

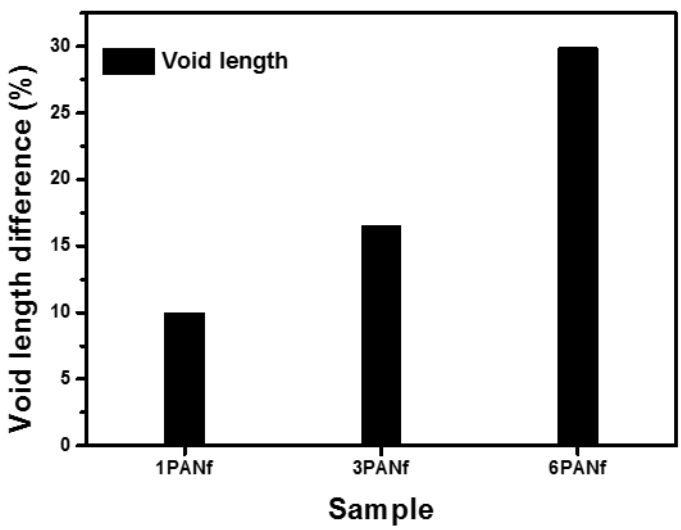

Figure 6.9. Void length difference between GPANf and EPANf.

The void information of 1GPANf, 1EPANf, 3GPANf, and 3EPANf were calculated with same method introduced in Figure 5.12 and Table 3 (Figure 6.8). Overall, EP-

ANf has lower void length than GPANf and the reduction ratio in void length between GPANf and EPANf was 10.06 and 16.46% for 1PANf and 3PANf respectively (Figure 6.9). Compared with 6PANf (reduction ratio was 29.9%), the reduction ratio decreased as MA content decreased. Note that based on mechanical properties (Figure 6.4 (a)), TGA behavior (Figure 6.7 (a)), void length of 1PANf, 1GPANf and 1EPANf were regarded as same fibers. In case of void angle, any tendency between samples was not found.

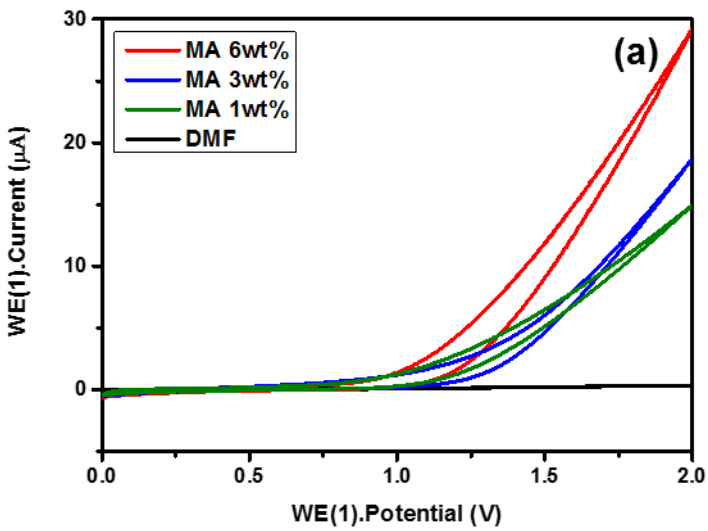

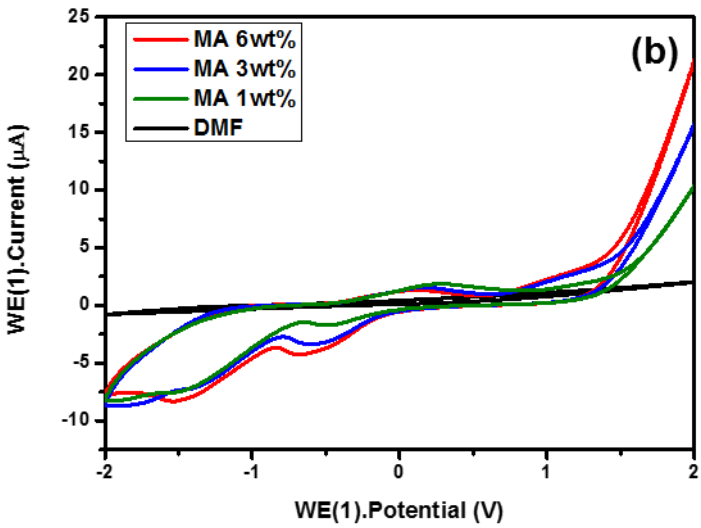

Figure 6.10. Cyclic voltammetry scan of PAN solutions with different MA content. (a) Range from 0 to 2 V and (b) range from -2 V to 2 V.

To find out whether redox reaction occur or not in PAN solution during current-assisted wet-spinning, cyclic voltammetry (CV) was conducted for PAN solutions containing MA 1 wt%, 3 wt%, and 6 wt%. Working electrode, counter electrode, and reference electrode were Pt, Pt, and $AgNO_3$, respectively and scan rate was 50 mV/s. In Figure 6.10 (a) (0 – 2 V), when working electrode was positive, there were no peaks but the current was only exponentially increased (mass transfer) as potential increased. However, in Figure 6.10 (b), reduction peaks around -0.5 V and oxidation peaks around 0.25 V were definitely observed. Considering Figure 6.10 (a) and the scan direction (0 V → -2 V → 0 V → 2 V), some species were first reduced at negative working electrode and the species were again oxidized at positive working electrode. Thus, the oxidation peaks, which were observed in Figure 6.10 (b), were

not observed in Figure 6.10 (a). Furthermore, in DMF plot in Figure 6.10 (b), there were no redox peaks so the redox peaks in PAN solutions were not related to DMF electrolysis. Reduction peak intensity was reduced in order as MA content decreased. It was expected that the species were CH_3 detached from methyl acrylate group by electric field.

6.3.2 CNT-incorporated PAN filaments

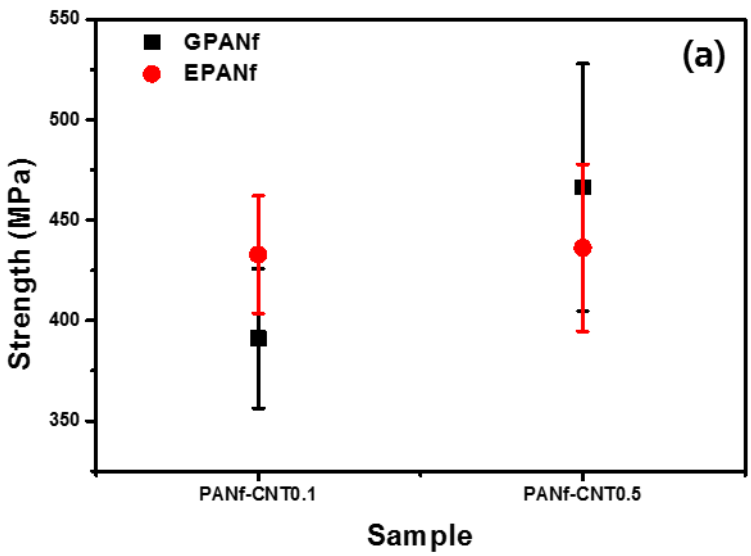

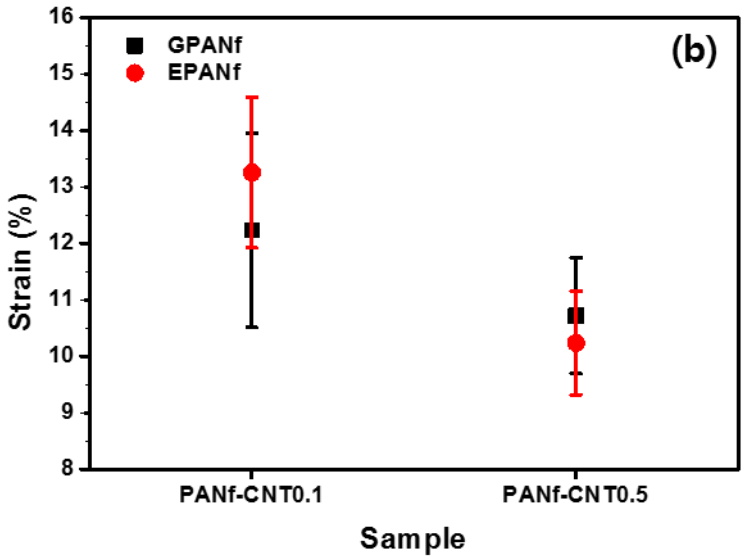

Figure 6.11. (a) Average strength, and (c) the average strain with error bar for GPANf and EPANf.

CNT incorporated PAN fibers were fabricated *via* general wet-spinning and current-assisted wet-spinning. The black square point with black error bar and the red round point with red error bar meant GPANf and EPANf, respectively. The 0.1 wt% and 0.5 wt% of CNT/PAN fibers were denoted as GPANf-CNT0.1, EPANf-CNT0.1, GPANf-CNT0.5, and EPANf-CNT0.5. Their mechanical properties were evaluated *via* tensile test (Figure 6.11). The failure strength and strain of EPANf-CNT0.1 increased by 10.7% and 8.3% respectively than those of GPANf-CNT0.1. However, these increasing value were much smaller than increasing value between 6GPANf and 6EPANf (23% and 28% for strength and strain). On the other hand, EPANf-CNT0.5 showed a little bit decreased mechanical properties than GPANf-CNT0.5. The hydrophobic CNT would suppress the driving force attracting non-solvent. So

at high CNT (0.5 wt%) concentration, there were almost no difference between GPANf-CNT0.5 and EPANf-CNT0.5.

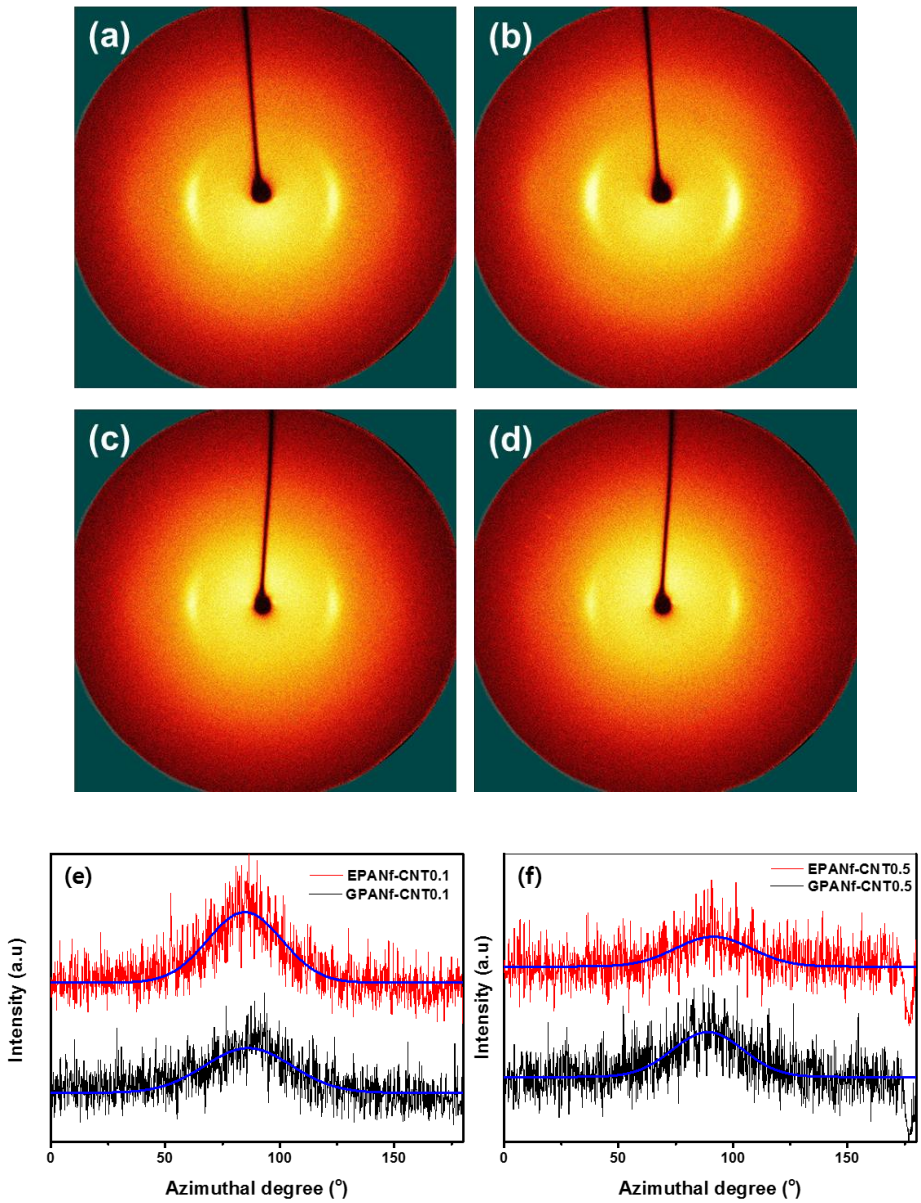

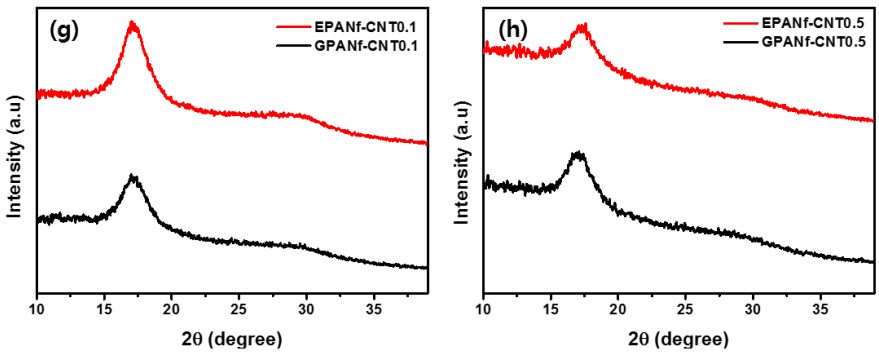

Figure 6.12. 2D-WAXD images of (a) GPANf-CNT0.1, (b) EPANf-CNT0.1, (c) GPANf-CNT0.5, and (d) EPANf-CNT0.5. Azimuthal scan of (d) PANf-CNT0.1 and (e) PANf-CNT0.5. Equatorially extracted 1D XRD plot of (g) PANf-CNT0.1 and (h) PANf-CNT0.5.

Table 7. Crystallinity and preferred orientation of CNT incorporated PAN fibers.

	GPANf-CNT0.1	EPANf-CNT0.1	GPANf-CNT0.5	GPANf-CNT0.5
Crystallinity (%)	38.4	40.5	43.6	43.7
Preferred orientation (%)	75.1	78.74	82.84	81.55

The microstructure of CNT/PAN fibers was evaluated *via* 2D-WAXD (Figure 6.12 (a), (b), (c), and (d)). Like other samples, the crystallinity and the preferred orientation of PANf-CNT were calculated from equatorially extracted 1D XRD plot (Figure 6.12 (g) and (h)) and azimuthal scan (Figure 6.12 (e) and (f)) respectively. In Figure 6.12 (g) and (h), strong peak at $2\theta = 16.9$ ° and very weak peak at $2\theta = 30$ ° were observed, which are characteristic peak of PAN fibers (Figure 4.7). However, peak of the (002) plane of CNT at $2\theta = 26.5$ ° was not identified because the concentration of CNT was too low (0.1 wt% and 0.5 wt%). Even in 5 wt% of CNT

incorporated PAN fibers, the peak at 2 θ = 26.5 ° of MWNT was not well observed [154]. Generally, the crystallinity a little bit increased in EPANf-CNT than GPANf-CNT (Table 7). The preferred orientation (P.O) of EPANf-CNT0.1 increased by about 3.6% than GPANf-CNT0.1. This increased value was comparable to increased value (3.1%) between 6GPANf and 6EPANf. So it was thought that the increased P.O of EPANf-CNT0.1 would come from PAN matrix. As explained in page 130 in section 5.2.3.5, it was expected that the voids containing non-solvent would resist to drawing and deformation so the extra force would be applied to PAN matrix adjacent to voids. However, the P.O of EPANf-CNT0.5 decreased slightly. Considering mechanical properties GPANf-CNT0.5 and EPANf-CNT0.5, there was no effect of current-assisted process in PANF-CNT0.5, which was also shown in the result of P.O in GPANf-CNT0.5 and EPANf-CNT0.5.

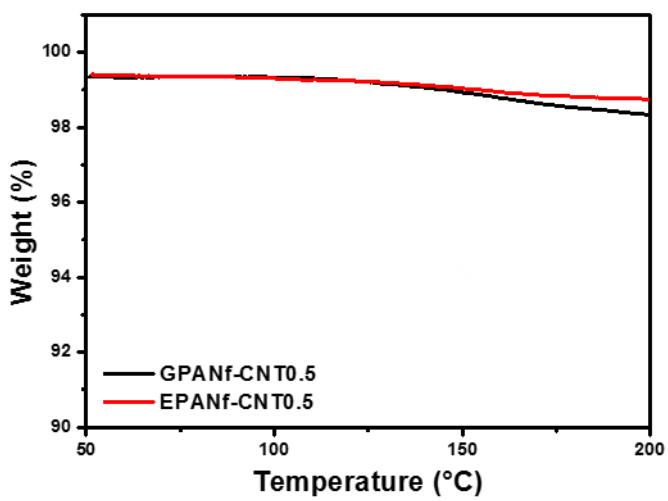

Figure 6.13. TGA comparison of GPANf-CNT0.5 and EPANf-CNT0.5.

Unlike other samples without CNT, there was no effect of absorbing more non-

solvent in case of EPANf-CNT0.5 compared with GPANf-CNT0.5 (Figure 6.13). However, like other GPANf and EPANf, GPANf-CNT0.5 showed more absorbed solvent around 150 °C than EPANf-CNT0.5.

6.4. Summary

To delicately verify the mechanism of current-assisted wet-spinning process, PAN solutions containing different MA contents and PAN solutions containing different CNT contents were prepared and spun through current-assisted wet-spinning process. They were compared with fibers fabricated *via* general wet-spinning. As MA content decreased, the difference in mecahnical properties and void length between GPANf and EPANf were decreased. The difference in absorbed non-solvent content between EPANf than GPANf was also decreased as MA content decreased. This meant that the number of carboxylate ions formed by demethylation triggered by applied electric potential would be low in low MA content. This led to a decrease in the force attracting non-solvent in coagulation bath. Low absorbed non-solvent finally caused almost no difference in void length between GPANf and EPANf (nanocavitation would be less suppressed due to low absorbed non-solvent).

CNT incorporated PAN fiber fabricated *via* current-assisted wet-spinning showed the effect of current-assisted process at low CNT content. However, the increased value in mechanical properties between GPANf-CNT and EPANf-CNT was lower than that between GPANf and EPANf. At high CNT content, the effect of current-assisted process did not appeared at all. Finally, it could be said that hydrophobic CNT lowered the force attracting non-solvent in coagulation bath during current-assisted wet-spinning process.

7. Conclusion

This thesis introduced world firstly tried current-assisted wet-spinning process and the mechanism of improved mechanical properties of PAN fibers fabricated *via* current-assisted wet-spinning process. The main idea of the process came from electrospinning. In current-assisted wet-spinning process, almost parts of the process were same with general wet-spinning process except syringe part. So syringe pump and syringe for current-assisted wet-spinning were self-designed. Before setting current-assisted wet-spinning process, optimization of wet-spinning process and PAN solution preparation procedure were necessary. Proper PAN solution preparation procedure and other parameters (flow rate, coagulation bath composition, jet ratio, drawing ratio, and drying temperature) were determined.

By simply applying electric potential *via* connecting negative and positive sockets to syringe plunger and nozzle, the current-assisted wet-spinning process was conducted. The flown electric current during current-assisted wet-spinning was several hundreds of microampere. PAN fibers fabricated *via* general wet-spinning process (GPANf) and PAN fibers fabricated *via* the current-assisted wet-spinning process (EPANf) were compared *via* various characterization methods. EPANf showed 23% and 28% higher the failure strength and strain than GPANf. EPANf absorbed more non-solvent than GPANf (TGA) because carboxylate ions formed by applying electric potential attracted more non-solvent. This was confirmed by XPS and H-NMR. EPANf showed lower number of CH_3 in H-NMR and higher fraction of C=O than the fraction of C-O in XPS than GPANf. The more absorbed water stopped enlargement of voids and nanocavitation in EPNf during drawing process.

That was why EPANf had higher mechanical properties than GPANf.

PAN solutions having different methyl acrylate (MA) content and different CNT content were prepared and spun *via* current-assisted wet-spinning. As MA content decreased, the increased value of mechanical properties in EPANf sequentially decreased. Simultaneously, the absorbed non-solvent gap between GPANf and EPANf got lower as MA content decreased because the source of driving force attracting non-solvent decreased. Similarly, as CNT content increased, the increasing value of mechanical properties in EPANf-CNT was decreased because hydrophobic CNT reduced the effect of current-assisted process. By conducting these experiments, the mechanism of improved mechanical properties of EPANf became more clear.

Consequently, the mechanism of improved mechanical properties of fibers fabricated *via* current-assisted wet-spinning process was well established by various characterization. The order of mechanism was as follows: 1. the applied electric field caused demethylation (ions mass transfer by electrophoresis and redox reaction were displayed as the electric current). 2. The formed ions from demethylation attracted more non-solvent in coagulation bath. 3. More absorbed non-solvent prevented enlargement of voids and nanocavitation during drawing process. Through these procedures, the fibers showed higher mechanical properties. The parameters of wet-spinning have been successfully optimized because the process has been conducted for almost 80 years. So based on these researches, the process has been commercially established successfully. This current-assisted wet-spinning process would suggest a new way of wet spinning by introducing a new parameter.

References

1. Frank, E., et al., *Carbon Fibers: Precursor Systems, Processing, Structure, and Properties.* Angewandte Chemie International Edition, 2014. **53**(21): p. 5262-5298.
2. Chung, D.D. and D. Chung, *Carbon fiber composites*. 2012: Butterworth-Heinemann.
3. Morris, E.A., et al., *Synthesis, spinning, and properties of very high molecular weight poly(acrylonitrile-co-methyl acrylate) for high performance precursors for carbon fiber.* Polymer, 2014. **55**(25): p. 6471-6482.
4. Kobashi, T. and S. Takao, *Polyacrylonitrile fiber with high strength and high modulus of elasticity*. 1987, Google Patents.
5. Gupta, V. and V. Kothari, *Manufactured fibre technology*. 2012: Springer Science & Business Media.
6. Moad, G., E. Rizzardo, and S.H. Thang, *Living Radical Polymerization by the RAFT Process.* Australian Journal of Chemistry, 2005. **58**(6): p. 379-410.
7. Spörl, J.M., et al., *Carbon fibers prepared from tailored reversible-addition-fragmentation transfer copolymerization-derived poly(acrylonitrile)-co-poly(methylmethacrylate).* Journal of Polymer Science Part A: Polymer Chemistry, 2014. **52**(9): p. 1322-1333.
8. An, Q., et al., *Study on kinetics of controlled/living radical polymerization of acrylonitrile by RAFT technique.* Journal of Polymer Science Part A: Polymer Chemistry, 2005. **43**(9): p. 1973-1977.
9. Niu, S., et al., *Synthesis of high molecular weight and narrow molecular weight distribution poly(acrylonitrile) via RAFT polymerization.* Journal of Polymer Science Part A: Polymer Chemistry, 2013. **51**(5): p. 1197-1204.
10. Kopeć, M., et al., *Aqueous RAFT Polymerization of Acrylonitrile.* Macromolecules, 2016. **49**(16): p. 5877-5883.
11. Tsai, J.-S., *Effect of drawing ratio during spinning and oxidation on the properties of polyacrylonitrile precursor and resulting carbon fibre.* Journal of Materials Science Letters, 1992. **11**(3): p. 140-142.
12. Tsai, J.S. and C.H. Lin, *Polyacrylonitrile precursors by copolymer and additive with itaconic acid.* Journal of Materials Science Letters, 1990. **9**(8): p. 869-871.
13. Tsai, J.S. and C.H. Lin, *Effect of comonomer composition on the properties of polyacrylonitrile precursor and resulting carbon fiber.* Journal of Applied Polymer Science, 1991. **43**(4): p. 679-685.
14. Adachi, Y. and K. Nabae, *Acrylic fibers for producing carbon fibers*. 1985, Google Patents.
15. Eom, Y. and B.C. Kim, *Solubility parameter-based analysis of polyacrylonitrile solutions in N,N-dimethyl formamide and dimethyl sulfoxide.* Polymer, 2014. **55**(10): p. 2570-2577.

16. A., N.B., et al., *Processing, structure, and properties of gel spun PAN and PAN/CNT fibers and gel spun PAN based carbon fibers.* Polymer Engineering & Science, 2015. **55**(11): p. 2603-2614.
17. Newcomb, B.A., et al., *Polyacrylonitrile solution homogeneity study by dynamic shear rheology and the effect on the carbon fiber tensile strength.* Polymer Engineering & Science, 2016. **56**(3): p. 361-370.
18. Zhang, J., et al., *Dry-jet wet-spun PAN/MWCNT composite fibers with homogeneous structure and circular cross-section.* Journal of Applied Polymer Science, 2012. **125**(S1): p. E58-E66.
19. Zeng, X., et al., *Diffusion Mechanism of As-spun Polyacrylonitrile Fiber in a Dimethyl Sulfoxide-Water Coagulation Bath.* Journal of Macromolecular Science, Part A, 2006. **43**(11): p. 1711-1720.
20. I., S.A. and K.V. P., *Influence of drawing speed on some properties of acrylic fibers.* Journal of Applied Polymer Science, 1981. **26**(6): p. 1813-1818.
21. Chen, J., et al., *Effect of coagulation temperature on the properties of poly(acrylonitrile- itaconic acid) fibers in wet spinning.* Journal of Polymer Research, 2007. **14**(3): p. 223-228.
22. Xing-Guang, D., et al., *Effect of DMSO/H2O coagulation bath on the structure and property of polyacrylonitrile fibers during wet-spinning.* Journal of Applied Polymer Science, 2007. **105**(3): p. 1221-1227.
23. Rahman, M.A., A.F. Ismail, and A. Mustafa, *The effect of residence time on the physical characteristics of PAN-based fibers produced using a solvent-free coagulation process.* Materials Science and Engineering: A, 2007. **448**(1): p. 275-280.
24. Chen, J., et al., *Study on the Coagulation Mechanism of Wet-Spinning PAN Fibers.* Journal of Polymer Research, 2006. **13**(6): p. 515-519.
25. Knudsen, J.P., *The Influence of Coagulation Variables on the Structure and Physical Properties of an Acrylic Fiber.* Textile Research Journal, 1963. **33**(1): p. 13-20.
26. Yan-Xiang, W., W. Cheng-Guo, and Y. Mei-Jie, *Effects of different coagulation conditions on polyacrylonitrile fibers wet spun in a system of dimethylsulphoxide and water.* Journal of Applied Polymer Science, 2007. **104**(6): p. 3723-3729.
27. Peng, G.-q., et al., *Effect of Coagulation Bath DMSO Concentration on the Structure and Properties of Polyacrylonitrile (PAN) Nascent Fibers during Wet-Spinning.* Journal of Macromolecular Science, Part B, 2008. **47**(6): p. 1130-1141.
28. Zhou, P., et al., *Effect of Bath Concentration on Coagulation Kinetics at the Early Stage during Wet Spinning of PAN Copolymer Nascent Fibers.* Journal of Macromolecular Science, Part B, 2011. **50**(6): p. 1215-1225.
29. Hou, C., Y. Liang, and C.-G. Wang, *Determination of the Diffusion Coefficient of H2O in Polyacrylonitrile Fiber Formation.* Journal of Polymer Research, 2005. **12**(1): p. 49-52.

30. Ouyang, Q., et al., *Effect of Jet Swell and Jet Stretch on the Structure of Wet-Spun Polyacrylonitrile Fiber.* Journal of Macromolecular Science, Part B, 2011. **50**(12): p. 2417-2427.
31. Yan-Xiang, W., et al., *Effect of the drawing process on the wet spinning of polyacrylonitrile fibers in a system of dimethyl sulfoxide and water.* Journal of Applied Polymer Science, 2007. **104**(2): p. 1026-1037.
32. Xiaomei, Z., et al., *Investigating the jet stretch in the wet spinning of PAN fiber.* Journal of Applied Polymer Science, 2007. **106**(4): p. 2267-2273.
33. Tsai, J.-S. and W.-C. Su, *Control of cross-section shape for polyacrylonitrile fibre during wet-spinning.* Journal of materials science letters, 1991. **10**(21): p. 1253-1256.
34. Masson, J., *Acrylic fiber technology and applications*. 1995: CRC Press.
35. S., A., et al., *Designing index of void structure and tensile properties in wet-spun polyacrylonitrile (PAN) fiber. I. Effect of dope polymer or nonsolvent concentration.* Journal of Applied Polymer Science, 2008. **109**(6): p. 3461-3469.
36. Chen, J.C. and I.R. Harrison, *Modification of polyacrylonitrile (PAN) carbon fiber precursor via post-spinning plasticization and stretching in dimethyl formamide (DMF).* Carbon, 2002. **40**(1): p. 25-45.
37. Jain, M.K. and A.S. Abhiraman, *Conversion of acrylonitrile-based precursor fibres to carbon fibres.* Journal of Materials Science, 1987. **22**(1): p. 278-300.
38. B., M.R., M. J., and B.O. P., *Bimodification of polyacrylonitrile (PAN) fibers.* Journal of Applied Polymer Science, 1993. **49**(3): p. 469-476.
39. Wu, G.-P., et al., *Effect of boric acid on oxidative stabilization of polyacrylonitrile fibers.* Fibers and Polymers, 2011. **12**(7): p. 979.
40. Mittal, J., et al., *Post spinning treatment of PAN fibers using succinic acid to produce high performance carbon fibers.* Carbon, 1998. **36**(7): p. 893-897.
41. Mathur, R.B., et al., *Characteristics of KMnO4-modified PAN fibres—its influence on the resulting carbon fibres' properties.* Carbon, 1994. **32**(1): p. 71-77.
42. Xi, Z.W. and W.Y. Zhi, *Manufacture of carbon fibers from polyacrylonitrile precursors treated with CoSO4.* Journal of Applied Polymer Science, 2002. **85**(1): p. 153-158.
43. Ko, T.-H. and L.-C. Huang, *Preparation of high-performance carbon fibres from PAN fibres modified with cobaltous chloride.* Journal of Materials Science, 1992. **27**(9): p. 2429-2436.
44. V., S.T., et al., *Polyacrylonitrile Single-Walled Carbon Nanotube Composite Fibers.* Advanced Materials, 2004. **16**(1): p. 58-61.
45. Chae, H.G., et al., *A comparison of reinforcement efficiency of various types of carbon nanotubes in polyacrylonitrile fiber.* Polymer, 2005. **46**(24): p. 10925-10935.
46. Chae, H.G., M.L. Minus, and S. Kumar, *Oriented and exfoliated single wall*

carbon nanotubes in polyacrylonitrile. Polymer, 2006. **47**(10): p. 3494-3504.
47. Jian, Z., et al., *Dry-jet wet-spun PAN/MWCNT composite fibers with homogeneous structure and circular cross-section.* Journal of Applied Polymer Science, 2012. **125**(S1): p. E58-E66.
48. Newcomb, B.A., et al., *Stress transfer in polyacrylonitrile/carbon nanotube composite fibers.* Polymer, 2014. **55**(11): p. 2734-2743.
49. Li, X., et al., *Drawing dependent structures, mechanical properties and cyclization behaviors of polyacrylonitrile and polyacrylonitrile/carbon nanotube composite fibers prepared by plasticized spinning.* Physical Chemistry Chemical Physics, 2015. **17**(34): p. 21856-21865.
50. Y., X., et al., *One-Dimensional Nanostructures: Synthesis, Characterization, and Applications.* Advanced Materials, 2003. **15**(5): p. 353-389.
51. D., L. and X. Y., *Electrospinning of Nanofibers: Reinventing the Wheel?* Advanced Materials, 2004. **16**(14): p. 1151-1170.
52. Lee, B.-S. and W.-R. Yu, *PA6/MWNT nanocomposites fabricated using electrospun nanofibers containing MWNT.* Macromolecular Research, 2010. **18**(2): p. 162-169.
53. Gyeong-Man, K., et al., *The Mechanical Deformation Process of Electrospun Polymer Nanocomposite Fibers.* Macromolecular Rapid Communications, 2005. **26**(9): p. 728-733.
54. Yoo, H.J., S.S. Mahapatra, and J.W. Cho, *High-Speed Actuation and Mechanical Properties of Graphene-Incorporated Shape Memory Polyurethane Nanofibers.* The Journal of Physical Chemistry C, 2014. **118**(19): p. 10408-10415.
55. Dae-Jin, Y., et al., *Ultrasensitive and Highly Selective Gas Sensors Based on Electrospun SnO2 Nanofibers Modified by Pd Loading.* Advanced Functional Materials, 2010. **20**(24): p. 4258-4264.
56. Kim, I.-D., et al., *Ultrasensitive Chemiresistors Based on Electrospun TiO2 Nanofibers.* Nano Letters, 2006. **6**(9): p. 2009-2013.
57. Choi, S.-J., et al., *Selective Diagnosis of Diabetes Using Pt-Functionalized WO3 Hemitube Networks As a Sensing Layer of Acetone in Exhaled Breath.* Analytical Chemistry, 2013. **85**(3): p. 1792-1796.
58. Lee, B.-S., et al., *Effects of Substrate on Piezoelectricity of Electrospun Poly(vinylidene fluoride)-Nanofiber-Based Energy Generators.* ACS Applied Materials & Interfaces, 2014. **6**(5): p. 3520-3527.
59. Chang, C., et al., *Direct-Write Piezoelectric Polymeric Nanogenerator with High Energy Conversion Efficiency.* Nano Letters, 2010. **10**(2): p. 726-731.
60. Chen, Y.Q., X.J. Zheng, and X. Feng, *The fabrication of vanadium-doped ZnO piezoelectric nanofiber by electrospinning.* Nanotechnology, 2010. **21**(5): p. 055708.
61. Wang, L., et al., *A novel carbon–silicon composite nanofiber prepared via electrospinning as anode material for high energy-density lithium ion batteries.* Journal of Power Sources, 2010. **195**(15): p. 5052-5056.

62. Ji, L., et al., *Porous carbon nanofiber-sulfur composite electrodes for lithium/sulfur cells.* Energy & Environmental Science, 2011. **4**(12): p. 5053-5059.
63. Yan, Y., et al., *Encapsulation of Sn@carbon Nanoparticles in Bamboo-like Hollow Carbon Nanofibers as an Anode Material in Lithium-Based Batteries.* Angewandte Chemie International Edition, 2009. **48**(35): p. 6485-6489.
64. Im, J.S., et al., *The study of controlling pore size on electrospun carbon nanofibers for hydrogen adsorption.* Journal of Colloid and Interface Science, 2008. **318**(1): p. 42-49.
65. Zhou, X., et al., *Mesoporous Coaxial Titanium Nitride-Vanadium Nitride Fibers of Core–shell Structures for High-Performance Supercapacitors.* ACS Applied Materials & Interfaces, 2011. **3**(8): p. 3058-3063.
66. Wu, J., et al., *Electrospinning of multilevel structured functional micro-/nanofibers and their applications.* Journal of Materials Chemistry A, 2013. **1**(25): p. 7290-7305.
67. Lu, Y., et al., *Mild immobilization of diverse macromolecular bioactive agents onto multifunctional fibrous membranes prepared by coaxial electrospinning.* Acta Biomaterialia, 2009. **5**(5): p. 1562-1574.
68. Moghe, A.K. and B.S. Gupta, *Co-axial Electrospinning for Nanofiber Structures: Preparation and Applications.* Polymer Reviews, 2008. **48**(2): p. 353-377.
69. Lee, B.-S., et al., *An effective method for manufacturing hollow carbon nanofibers and microstructural analysis.* Macromolecular Research, 2012. **20**(6): p. 605-613.
70. Lee, B.-S., et al., *Anodic properties of hollow carbon nanofibers for Li-ion battery.* Journal of Power Sources, 2012. **199**: p. 53-60.
71. Lee, B.-S., et al., *Effect of Pores in Hollow Carbon Nanofibers on Their Negative Electrode Properties for a Lithium Rechargeable Battery.* ACS Applied Materials & Interfaces, 2012. **4**(12): p. 6702-6710.
72. Lee, B.-S., et al., *Fabrication of Si core/C shell nanofibers and their electrochemical performances as a lithium-ion battery anode.* Journal of Power Sources, 2012. **206**: p. 267-273.
73. Mu, J., et al., *High Photocatalytic Activity of ZnO−Carbon Nanofiber Heteroarchitectures.* ACS Applied Materials & Interfaces, 2011. **3**(2): p. 590-596.
74. Lee, J.S., et al., *Fabrication of Ultrafine Metal-Oxide-Decorated Carbon Nanofibers for DMMP Sensor Application.* ACS Nano, 2011. **5**(10): p. 7992-8001.
75. Ji, L. and X. Zhang, *Electrospun carbon nanofibers containing silicon particles as an energy-storage medium.* Carbon, 2009. **47**(14): p. 3219-3226.
76. Wu, J., et al., *Facile Synthesis and Evaluation of Nanofibrous Iron–Carbon Based Non-Precious Oxygen Reduction Reaction Catalysts for Li–O2*

Battery Applications. The Journal of Physical Chemistry C, 2012. **116**(17): p. 9427-9432.
77. Kim, C. and K.S. Yang, *Electrochemical properties of carbon nanofiber web as an electrode for supercapacitor prepared by electrospinning.* Applied Physics Letters, 2003. **83**(6): p. 1216-1218.
78. Joshi, P., et al., *Electrospun Carbon Nanofibers as Low-Cost Counter Electrode for Dye-Sensitized Solar Cells.* ACS Applied Materials & Interfaces, 2010. **2**(12): p. 3572-3577.
79. Ghasemi, M., et al., *Activated carbon nanofibers as an alternative cathode catalyst to platinum in a two-chamber microbial fuel cell.* International Journal of Hydrogen Energy, 2011. **36**(21): p. 13746-13752.
80. Li, D. and Y. Xia, *Direct Fabrication of Composite and Ceramic Hollow Nanofibers by Electrospinning.* Nano Letters, 2004. **4**(5): p. 933-938.
81. Chen, H., et al., *Nanowire-in-Microtube Structured Core/Shell Fibers via Multifluidic Coaxial Electrospinning.* Langmuir, 2010. **26**(13): p. 11291-11296.
82. Lee, B.-S., et al., *Novel multi-layered 1-D nanostructure exhibiting the theoretical capacity of silicon for a super-enhanced lithium-ion battery.* Nanoscale, 2014. **6**(11): p. 5989-5998.
83. Lee, B.-S., et al., *New Electrospinning Nozzle to Reduce Jet Instability and Its Application to Manufacture of Multi-layered Nanofibers.* Scientific Reports, 2014. **4**: p. 6758.
84. He, D.-X., et al., *Microstructural evolution during thermal stabilization of PAN fibers.* Journal of Materials Science, 2007. **42**(17): p. 7402-7407.
85. Lee, B.-S., et al., *Face-Centered-Cubic Lithium Crystals Formed in Mesopores of Carbon Nanofiber Electrodes.* ACS Nano, 2013. **7**(7): p. 5801-5807.
86. Ryu, Z., et al., *Characterization of pore size distributions on carbonaceous adsorbents by DFT.* Carbon, 1999. **37**(8): p. 1257-1264.
87. Kim, D.-K., et al., *Electrospun polyacrylonitrile-based carbon nanofibers and their hydrogen storages.* Macromolecular Research, 2005. **13**(6): p. 521-528.
88. Lu, L., et al., *A review on the key issues for lithium-ion battery management in electric vehicles.* Journal of Power Sources, 2013. **226**: p. 272-288.
89. Gallagher, K.G., et al., *Quantifying the promise of lithium-air batteries for electric vehicles.* Energy & Environmental Science, 2014. **7**(5): p. 1555-1563.
90. Ge, M., et al., *Review of porous silicon preparation and its application for lithium-ion battery anodes.* Nanotechnology, 2013. **24**(42): p. 422001.
91. Ashuri, M., Q. He, and L.L. Shaw, *Silicon as a potential anode material for Li-ion batteries: where size, geometry and structure matter.* Nanoscale, 2016. **8**(1): p. 74-103.
92. Yin, Y., L. Wan, and Y. Guo, *Silicon-based nanomaterials for lithium-ion*

batteries. Chinese Science Bulletin, 2012. **57**(32): p. 4104-4110.
93. Mukhopadhyay, A. and B.W. Sheldon, *Deformation and stress in electrode materials for Li-ion batteries.* Progress in Materials Science, 2014. **63**: p. 58-116.
94. Berla, L.A., et al., *Robustness of amorphous silicon during the initial lithiation/delithiation cycle.* Journal of Power Sources, 2014. **258**: p. 253-259.
95. Liu, N., et al., *A pomegranate-inspired nanoscale design for large-volume-change lithium battery anodes.* Nature Nanotechnology, 2014. **9**: p. 187.
96. Wada, T., et al., *Bulk-Nanoporous-Silicon Negative Electrode with Extremely High Cyclability for Lithium-Ion Batteries Prepared Using a Top-Down Process.* Nano Letters, 2014. **14**(8): p. 4505-4510.
97. Fan, Y., et al., *High performance lithium ion battery anodes based on carbon nanotube–silicon core–shell nanowires with controlled morphology.* Carbon, 2013. **59**: p. 264-269.
98. Li, X., et al., *Mesoporous silicon sponge as an anti-pulverization structure for high-performance lithium-ion battery anodes.* Nature Communications, 2014. **5**: p. 4105.
99. Zuo, X., et al., *Silicon based lithium-ion battery anodes: A chronicle perspective review.* Nano Energy, 2017. **31**: p. 113-143.
100. Besenhard, J.O., J. Yang, and M. Winter, *Will advanced lithium-alloy anodes have a chance in lithium-ion batteries?* Journal of Power Sources, 1997. **68**(1): p. 87-90.
101. Conductive, H., *Mechanically Robust, and Electrochemically Inactive TiC.* C Nanofiber Scaffold for High-Performance Silicon Anode Batteries Yao, Yan: p. 8346-8351.
102. Lee, B.-S., et al., *Silicon/Carbon Nanotube/BaTiO3 Nanocomposite Anode: Evidence for Enhanced Lithium-Ion Mobility Induced by the Local Piezoelectric Potential.* ACS Nano, 2016. **10**(2): p. 2617-2627.
103. Bogart, T.D., et al., *Enhancing the lithiation rate of silicon nanowires by the inclusion of tin.* RSC Advances, 2014. **4**(79): p. 42022-42028.
104. Zhou, X., et al., *Facile synthesis of silicon nanoparticles inserted into graphene sheets as improved anode materials for lithium-ion batteries.* Chemical Communications, 2012. **48**(16): p. 2198-2200.
105. Kohandehghan, A., et al., *Nanometer-scale Sn coatings improve the performance of silicon nanowire LIB anodes.* Journal of Materials Chemistry A, 2014. **2**(29): p. 11261-11279.
106. Wu, J., et al., *A novel Si/Sn composite with entangled ribbon structure as anode materials for lithium ion battery.* Scientific Reports, 2016. **6**: p. 29356.
107. Lu, X., et al., *In Situ TEM Observations of Sn-Containing Silicon Nanowires Undergoing Reversible Pore Formation Due to Fast Lithiation/Delithiation Kinetics.* The Journal of Physical Chemistry C, 2015. **119**(38): p. 21889-21895.

108. Lee, B.-S., et al., *Facile conductive bridges formed between silicon nanoparticles inside hollow carbon nanofibers.* Nanoscale, 2013. **5**(11): p. 4790-4796.
109. Kim, S.Y., et al., *Facile Synthesis of Carbon-Coated Silicon/Graphite Spherical Composites for High-Performance Lithium-Ion Batteries.* ACS Applied Materials & Interfaces, 2016. **8**(19): p. 12109-12117.
110. Yang, L.Y., et al., *Dual yolk-shell structure of carbon and silica-coated silicon for high-performance lithium-ion batteries.* Scientific Reports, 2015. **5**: p. 10908.
111. Hu, C.-C., et al., *Design and Tailoring of the Nanotubular Arrayed Architecture of Hydrous RuO2 for Next Generation Supercapacitors.* Nano Letters, 2006. **6**(12): p. 2690-2695.
112. Zhi, M., et al., *Nanostructured carbon-metal oxide composite electrodes for supercapacitors: a review.* Nanoscale, 2013. **5**(1): p. 72-88.
113. Yuena, M., et al., *Hierarchical Porous Graphene/Polyaniline Composite Film with Superior Rate Performance for Flexible Supercapacitors.* Advanced Materials, 2013. **25**(48): p. 6985-6990.
114. Ni, J., Y. Huang, and L. Gao, *A high-performance hard carbon for Li-ion batteries and supercapacitors application.* Journal of Power Sources, 2013. **223**: p. 306-311.
115. Shinichi, K., et al., *Electrochemical Na Insertion and Solid Electrolyte Interphase for Hard-Carbon Electrodes and Application to Na-Ion Batteries.* Advanced Functional Materials, 2011. **21**(20): p. 3859-3867.
116. T., L.K., et al., *Synthesis and Rate Performance of Monolithic Macroporous Carbon Electrodes for Lithium-Ion Secondary Batteries.* Advanced Functional Materials, 2005. **15**(4): p. 547-556.
117. Teo, W.E. and S. Ramakrishna, *A review on electrospinning design and nanofibre assemblies.* Nanotechnology, 2006. **17**(14): p. R89.
118. Byoung-Sun, L., Y. Ho-Sung, and Y. Woong-Ryeol, *Fabrication of double-tubular carbon nanofibers using quadruple coaxial electrospinning.* Nanotechnology, 2014. **25**(46): p. 465602.
119. Yang, H.-S., et al., *Fabrication of carbon nanofibers with Si nanoparticle-stuffed cylindrical multi-channels via coaxial electrospinning and their anodic performance.* RSC Advances, 2014. **4**(88): p. 47389-47395.
120. Padilla, R. and H.Y. Sohn, *The reduction of stannic oxide with carbon.* Metallurgical Transactions B, 1979. **10**(1): p. 109-115.
121. Read, J., et al., *SnO2-carbon composites for lithium-ion battery anodes.* Journal of Power Sources, 2001. **96**(2): p. 277-281.
122. Lou, X.W., et al., *Preparation of SnO2/Carbon Composite Hollow Spheres and Their Lithium Storage Properties.* Chemistry of Materials, 2008. **20**(20): p. 6562-6566.
123. Lu, F., et al., *Room temperature ionic liquid assisted well-dispersed core-shell tin nanoparticles through cathodic corrosion.* RSC Advances, 2013.

3(41): p. 18791-18793.
124. Yang, Z., et al., *Easy preparation of SnO2@carbon composite nanofibers with improved lithium ion storage properties.* Journal of Materials Research, 2011. **25**(8): p. 1516-1524.
125. Wang, C., A. John Appleby, and F.E. Little, *Electrochemical study on nano-Sn, Li4.4Sn and AlSi0.1 powders used as secondary lithium battery anodes.* Journal of Power Sources, 2001. **93**(1): p. 174-185.
126. Liu, L., et al., *Tin-based anode materials with well-designed architectures for next-generation lithium-ion batteries.* Journal of Power Sources, 2016. **321**: p. 11-35.
127. Guo, Z.P., et al., *Electrochemical lithiation and de-lithiation of MWNT–Sn/SnNi nanocomposites.* Carbon, 2005. **43**(7): p. 1392-1399.
128. Li, L., W. Qi, and W. Ru, *Enhancing mechanical properties of poly(vinyl alcohol) blown films by drawing and surface crosslinking.* Journal of Applied Polymer Science, 2005. **98**(2): p. 774-779.
129. Li, W., F. Xue, and R. Cheng, *States of water in partially swollen poly(vinyl alcohol) hydrogels.* Polymer, 2005. **46**(25): p. 12026-12031.
130. Ebdon, J.R., T.N. Huckerby, and T.C. Hunter, *Free-radical aqueous slurry polymerizations of acrylonitrile: 2. End-groups and other minor structures in polyacrylonitriles initiated by potassium persulfate/sodium bisulfite.* Polymer, 1994. **35**(21): p. 4659-4664.
131. R., M.T., S.B. C., and N.P. L., *Redox polymerization of acrylonitrile. Kinetics of the reaction initiated by the redox system tartaric acid–V5+.* Journal of Polymer Science: Polymer Chemistry Edition, 1975. **13**(9): p. 2075-2086.
132. Ali, R.M. and A. Mahdi, *Kinetic study of radical polymerization. VII. Investigation into the solution copolymerization of acrylonitrile and itaconic acid by real-time 1H NMR spectroscopy.* Journal of Applied Polymer Science, 2007. **103**(5): p. 3253-3260.
133. POPESCU, N., V. DESPA, and D. UNGUREANU, *Structural analysis of PAN fiber by X-ray diffraction.* J Sci Arts, 2010. **1**: p. 89-94.
134. Karbownik, I., et al., *Effect of doping polyacrylonitrile fibers on their structural and mechanical properties.* Polymer, 2015. **75**: p. 97-108.
135. Martin, K., et al., *Characteristics of wet-spun and thermally treated poly acrylonitrile fibers.* Journal of Applied Polymer Science, 2016. **133**(29).
136. Clayton, C.R., *Materials science and engineering: An introduction: by WD Callister Jr.; published by Wiley, Chichester, West Sussex, 1985; 602 pp.; price,£ 40.40*. 1987, Elsevier.
137. Dobbs, W., L. Douce, and B. Heinrich, *1-(4-Alkyloxybenzyl)-3-methyl-1H-imidazol-3-ium organic backbone: A versatile smectogenic moiety.* Beilstein Journal of Organic Chemistry, 2009. **5**: p. 62.
138. Liu, Y., et al., *Temperature dependent tensile behavior of gel-spun polyacrylonitrile and polyacrylonitrile/carbon nanotube composite fibers.*

Polymer, 2013. **54**(15): p. 4003-4009.
139. Nain, R., et al., *Zinc oxide nanorod assisted rapid single-step process for the conversion of electrospun poly(acrylonitrile) nanofibers to carbon nanofibers with a high graphitic content.* Nanoscale, 2016. **8**(7): p. 4360-4372.
140. Thünemann, A.F. and W. Ruland, *Microvoids in Polyacrylonitrile Fibers: A Small-Angle X-ray Scattering Study.* Macromolecules, 2000. **33**(5): p. 1848-1852.
141. Mengfan, W., et al., *SAXS and WAXD study of periodical structure for polyacrylonitrile fiber during coagulation.* Polymers for Advanced Technologies, 2015. **26**(2): p. 136-141.
142. Zhu, C.-z., et al., *2D SAXS/WAXD analysis of pan carbon fiber microstructure in organic/inorganic transformation.* Chinese Journal of Polymer Science, 2013. **31**(5): p. 823-832.
143. Wenjie, W., et al., *Small-angle X-ray scattering investigation of carbon nanotube-reinforced polyacrylonitrile fibers during deformation.* Journal of Polymer Science Part B: Polymer Physics, 2009. **47**(23): p. 2394-2409.
144. Zhu, C., et al., *A small-angle X-ray scattering study and molecular dynamics simulation of microvoid evolution during the tensile deformation of carbon fibers.* Carbon, 2012. **50**(1): p. 235-243.
145. Rozanski, A. and A. Galeski, *Controlling Cavitation of Semicrystalline Polymers during Tensile Drawing.* Macromolecules, 2011. **44**(18): p. 7273-7287.
146. Wu, Y., et al., *Switching Fluid Slippage on pH-Responsive Superhydrophobic Surfaces.* Langmuir, 2014. **30**(22): p. 6463-6468.
147. Hennig, A., et al., *En route to traceable reference standards for surface group quantifications by XPS, NMR and fluorescence spectroscopy.* Analyst, 2015. **140**(6): p. 1804-1808.
148. Zander, N.E., et al., *Coaxial Electrospun Poly(methyl methacrylate)–Polyacrylonitrile Nanofibers: Atomic Force Microscopy and Compositional Characterization.* The Journal of Physical Chemistry B, 2011. **115**(43): p. 12441-12447.
149. Wochnowski, C., M.A. Shams Eldin, and S. Metev, *UV-laser-assisted degradation of poly(methyl methacrylate).* Polymer Degradation and Stability, 2005. **89**(2): p. 252-264.
150. Bettencourt, A., et al., *Surface studies on acrylic bone cement.* International Journal of Pharmaceutics, 2004. **278**(1): p. 181-186.
151. Miller, G.C., et al., *Melt-spinnable polyacrylonitrile copolymer precursors for carbon fibers.* Polymer, 2017. **126**: p. 87-95.
152. Ayre, W.N., S.P. Denyer, and S.L. Evans, *Ageing and moisture uptake in polymethyl methacrylate (PMMA) bone cements.* Journal of the Mechanical Behavior of Biomedical Materials, 2014. **32**: p. 76-88.
153. Wang, Y., et al. *Properties of a triacetin molecule under an external electric*

field. in *2016 IEEE International Conference on High Voltage Engineering and Application (ICHVE)*. 2016.

154. A., K., et al., *Composites of Polyacrylonitrile and Multiwalled Carbon Nanotubes Prepared by Gelation/Crystallization from Solution.* Advanced Functional Materials, 2004. **14**(9): p. 842-850.

Korean abstract

습식방사는 섬유를 생산하는 가장 오래된 방사 공정 중 하나이다. 습식방사로 제조된 PAN 섬유는 열처리를 통해 탄소섬유로 제조될 수 있다는 것이 알려주면서 더 중요하게 되었다. 그러나 1949년에 PAN 섬유는 상용화 되면서 많은 변수들이 잘 정립되어 있는 상태이나 중요한 진척은 없는 상태이다. 습식방사에서 전류라는 새로운 변수는 다루어지지 않았으며 전류가 섬유의 물성에 미치는 영향 또한 조사되지 않았다.

이 논문에서는 완전히 새로운 공정에 대해서 소개하며 이는 전류인가 습식방사이다. 우리 지식에서 이 공정은 이 논문에서 최초로 시도되었다. 이 공정의 주요 아이디어는 전기방사 공정에서 가져왔다. 전기방사에서 고분자 용액은 고전압 (~ 수십 kV) 인가를 통해서 연속적인 나노 섬유를 제조하지만 고전압으로 인한 주요한 데미지는 섬유에 발현되지 않는다. 그래서 습식방사에서 또한 고분자 용액의 전압 인가가 가능할 것으로 여겨졌다. 전기방사와 마찬가지로 전류인가 습식방사 공정은 간단히 전압을 PAN용액에 인가함으로써 이루어졌으며 나머지는 기존의 습식방사 공정과 동일하다. 전기방사와는 달리 전류인가 습식방사 공정 중에 흐른 전류는 수백 마이크로 암페어 였다.

전류인가 습식방사를 통해 제조된 PAN 섬유 (EPANf)는 기존 습식방사를 통해 제조된 PAN 섬유 (GPANf)에 비해 20% 이상 증가된

역학적 특성을 보여주었다. EPANf의 증가된 역학적 특성의 메커니즘을 알아보기 위해 다양한 characterization 방법들이 두 섬유에 대해 측정되었다. 인가된 전압은 PAN 용액 내 이온 생성으로 인해 응고욕에서의 응고 환경을 바꾸게 되며 이로 인해 비용매의 흡수가 촉진된다. EPANf의 내의 더 흡수된 비용매는 기존 기공의 확대 및 nanocavitation을 막아준다. 이로 인해 역학적 특성이 증가하게 된다. 전류인가 습식방사의 간단한 설치로 인해 기존의 습삭방사에 쉽게 적용 가능할 것으로 예상되며 따라서 이는 PAN 섬유와 그들의 최종 생산물을 생산하는 혁신적인 공정이 될 것이다.

핵심어: PAN 섬유, 전류인가 습식방사, 습식방사, 증가된 역학적 특성, 결점 최소화

학번: 2014-31056